

# 3D reconstruction of curvilinear one-dimensional objects viewed in transmission electron microscopy

Présentée le 21 septembre 2023

Faculté des sciences de base  
Laboratoire de spectrométrie et microscopie électronique  
Programme doctoral en physique

pour l'obtention du grade de Docteur ès Sciences

par

**Gulnaz GANEEVA**

Acceptée sur proposition du jury

Prof. O. Yazyev, président du jury  
Prof. C. Hébert, Dr E. Oveisi, directeurs de thèse  
Dr R. Schäublin, rapporteur  
Prof. A. Guitton, rapporteur  
Prof. H. Stahlberg, rapporteur





# Acknowledgements

I would like to express my sincere gratitude to the following individuals and institutions who have supported me throughout my journey in completing this PhD thesis:

**Funding** Swiss National Science Foundation.

**Supervision** I am immensely grateful to my supervisor, Prof. Cécile Hébert, for affording me the opportunity to become a part of her group, allowing me to collaborate with esteemed researchers, and attend numerous conferences. Her expertise, kindness, and guidance have provided me with the motivation and strength needed throughout my journey. She is a true mentor who gave me both freedom and unwavering support whenever it was needed.

I extend my heartfelt gratitude to my co-advisor, Dr. Emad Oveisi, whose tremendous support and understanding guided me through challenging times. His encouragement and belief in my abilities gave me the confidence to pursue my goals. Furthermore, his profound expertise in the field furnished me with the essential knowledge and skills required to excel.

**Jury** Prof. Antoine Guitton of Université de Lorraine, Dr. Robin Schäublin of ETHZ, Prof. Henning Stahlberg of EPFL, and Prof. Oleg Yazyev of EPFL for accepting the invitation to be a member of my dissertation committee.

**LSME** Dr. Duncan Alexander for generously sharing his expertise and teaching me to use the electron microscope. Anastasiia Mishchuk, Federico Garro for productive collaboration and help with Python programming language. Diane Pellet for her kindness and help with the administrative work. I would like to emphasize that the lab fostered an exceptionally welcoming, positive, and supportive environment. It was a privilege to work with each of you.

**CIME** Dr. Davide Demurtas for sharing his knowledge on tomography and teaching me to use dedicated software. Dr. Reza Zamani, Dr. Victor Boureau, and Dr. Marco Cantoni for their technical support and assistance in troubleshooting while working with microscopes. Dr. Lucie Navratilova, Danièle Laub, and Colette Vallotton for their help with sample preparation.

<b>CVLab</b>	Okan Altingövde and Prof. Pascal Fua for our fruitful collaboration, insightful discussions, and the discoveries we made together.
<b>UPHESS</b>	Dr. Adélie Garin and Prof. Kathryn Hess Bellwald for dedicating their time to craft a tool for topological analysis and generously imparting their expertise.
<b>SUNMIL</b>	Dr. Quy Ong Khac and Prof. Francesco Stellacci for exciting cryo-experiments, as well as their availability and invaluable assistance.
<b>ETHZ-LMPT</b>	Dr. Robin Schäublin for CUFOUR simulations, his support, and significant dedication of his time for enlightening discussions.
<b>LUMES</b>	Dr. Thomas La Grange for sharing his knowledge on dislocations and teaching me to use NanoMEGAS ASTAR tool.
<b>Université de Lorraine</b>	Prof. Antoine Guitton and Dr. Chunyang Zhang for supplying TiAl samples.
<b>EDPY</b>	Anh Eymann for her kindness and support with the administrative work.
<b>Friends</b>	My wonderful colleagues and dear friends Tatiana Akhmetshina, Farhang Nabiei, Federica Landucci, Stéphane Poitel, Adrien Teurtrie, Bernat Mundet, Hui Chen, Xhemi Malja, Arman Ayan, Lucie Navratilova, Anton Smirnov, Antoine Delgoffe, Rita Therisod, Barbora Bártová, Fabienne Bobard for continuous support and the enjoyable moments we have shared together. Special thanks to my dearest friends, Guzel Chernova and Renara Garifullina, who emotionally supported me all this time despite the distance and time zones between us.
<b>Family</b>	<p>I am truly fortunate and proud to have my family as my foundation and guiding light in this journey:</p> <p>My mother, Raisa, who is my source of inspiration and motivation, always believing in my potential and guiding me with her wisdom. Her love, understanding, and sacrifices have been my constant pillars of strength.</p> <p>My father, Rinat, who always believed in me until his final days. His love and unwavering confidence gave me the energy to persevere even during the most challenging moments.</p> <p>My siblings, Elvira and Rishat, for sharing their life experience with me, for their encouragement, and support whenever I needed it.</p> <p>My husband, Pascal, whose unconditional love, belief in me, and willingness to stand by my side, no matter the challenges, have been vital in this journey.</p>

I am deeply grateful to each and every one of you for being a part of this transformative experience.

*Lausanne, September 2023*

Gulnaz Ganeeva

# Abstract

To obtain a more complete understanding of material microstructure at the nanoscale and to gain profound insights into their properties, there is a growing need for more efficient and precise methods that can streamline the process of 3D imaging using a transmission electron microscope (TEM) and reconstruction, thereby minimize the need for manual intervention. This interdisciplinary project focuses on the development of an automatic stereo-vision reconstruction method that utilizes deep-learning neural networks. The aim is to obtain the 3D distribution of significant one-dimensional curvilinear defects, specifically dislocations, by leveraging just two scanning transmission electron microscope (STEM) images captured from different viewing angles. As part of this project, the imaging conditions were optimized with the specific objective of ensuring that the captured images are optimal for the subsequent reconstruction process. The optimization aimed to maximize the quality and usefulness of the images for the reconstruction of the 3D distribution of dislocations. The specific characteristics of these images were considered, and a quantitative assessment was conducted using topological data analysis (TDA) on the neural network outputs. The results demonstrated a significant reduction in imaging and post-processing times compared to conventional techniques such as electron tomography. The study revealed the robustness of neural networks in handling noise levels in images, highlighting their ability to extract relevant information from noisy data.

Further optimization of the "tilt-less" technique has resulted in an enhanced stereo-angle for imaging and improved reconstruction quality. By incorporating a pixelated detector, it was possible to achieve a stereo-angle of  $9.32^\circ$ , while also gaining better control over the tilt angle. These advancements have not only been applied successfully to reconstruct the 3D distribution of dislocations but also to assess the 3D distribution of nanoparticles under cryogenic conditions. As a result, this approach has significantly reduced the acquisition time, as only a single acquisition is now required compared to the previous method of using tomography with multiple images.

The developed techniques in this work enable real-time observation of dynamic processes within the 3D volume of materials, opening new frontiers of exploration.

*Keywords: Scanning transmission electron microscopy, Deep learning, Stereo-vision, Three-dimensional reconstruction, Cryo electron microscopy, Curvilinear defects, Nanoparticles*



# Résumé

Afin d'obtenir une compréhension plus complète de la microstructure des matériaux à l'échelle nanométrique et de mieux comprendre leurs propriétés, il existe un besoin croissant de méthodes plus efficaces et plus précises capables de rationaliser le processus d'imagerie 3D à l'aide d'un microscope électronique à transmission (MET) ainsi que la reconstruction, minimisant ainsi la nécessité d'une intervention manuelle.

Ce projet interdisciplinaire se concentre sur le développement d'une méthode de reconstruction automatique de la stéréovision qui utilise des réseaux neuronaux d'apprentissage profond. L'objectif est d'obtenir la distribution 3D de défauts curvilignes unidimensionnels, en particulier des dislocations, en exploitant seulement deux images de microscope électronique à transmission à balayage (STEM) capturées à partir d'angles de vue différents. Dans le cadre de ce projet, les conditions d'imagerie ont été optimisées dans le but spécifique de garantir que les images capturées sont optimales pour le processus de reconstruction ultérieur. L'optimisation visait à maximiser la qualité et l'utilité des images pour la reconstruction de la distribution 3D des dislocations. Les caractéristiques spécifiques de ces images ont été prises en compte et une évaluation quantitative a été réalisée à l'aide de l'analyse des données topologiques (TDA) sur les sorties du réseau neuronal. Les résultats ont démontré une réduction significative des temps d'imagerie et de post-traitement par rapport aux techniques conventionnelles telles que la tomographie électronique. L'étude a révélé la robustesse des réseaux neuronaux dans la gestion des niveaux de bruit dans les images, soulignant leur capacité à extraire des informations pertinentes à partir de données bruitées.

L'optimisation de la technique "sans inclinaison" a permis d'obtenir un meilleur angle stéréoscopique pour l'imagerie et d'améliorer la qualité de la reconstruction. En incorporant un détecteur pixellisé, il a été possible d'obtenir un stéréo-angle de  $9,32^\circ$ , tout en obtenant un meilleur contrôle de l'angle d'inclinaison. Ces progrès ont été appliqués avec succès non seulement à la reconstruction de la distribution 3D des dislocations, mais aussi à l'évaluation de la distribution 3D de nanoparticules dans des conditions cryogéniques. En conséquence, cette approche a permis de réduire considérablement le temps d'acquisition, puisqu'une seule acquisition est désormais nécessaire par rapport à la méthode précédente qui consistait à utiliser la tomographie avec plusieurs dizaines d'images.

Les techniques développées dans ce travail permettent d'observer en temps réel les processus dynamiques dans le volume 3D des matériaux, ouvrant ainsi de nouvelles frontières

d'exploration.

*Mots-clefs : Microscopie électronique à balayage en transmission, Apprentissage profond, Stéréovision, Reconstruction tridimensionnelle, Cryo-microscopie électronique, Défauts curvilignes, Nanoparticules*

# Contents

<b>Acknowledgements</b>	<b>iii</b>
<b>Abstract (English/Français)</b>	<b>v</b>
<b>List of Figures</b>	<b>xi</b>
<b>List of Tables</b>	<b>xxi</b>
<b>1 Introduction</b>	<b>1</b>
<b>2 Materials and methods</b>	<b>7</b>
2.1 Materials . . . . .	7
2.2 Sample preparation . . . . .	8
2.2.1 FIB milling . . . . .	8
2.2.2 Electropolishing . . . . .	9
2.3 Microstructure of TiAl alloy . . . . .	10
2.3.1 Diffraction analysis . . . . .	12
2.3.2 Orientation mapping in TEM with NanoMEGAS ASTAR . . . . .	13
2.3.3 Chemical analysis . . . . .	14
2.4 STEM imaging of dislocations . . . . .	15
2.4.1 Optimization of imaging conditions . . . . .	17
2.5 Tomographic reconstruction of dislocations . . . . .	17
2.6 Stereo 3D reconstruction . . . . .	18
2.7 Concluding remarks . . . . .	20
<b>3 Stereo 3D reconstruction of dislocations by deep learning neural networks</b>	<b>23</b>
3.1 Introduction . . . . .	23
3.2 Image rectification . . . . .	24
3.3 Dislocation detection and matching . . . . .	25
3.3.1 Pre-trained contour detection network . . . . .	26
3.3.2 Feature Volume . . . . .	27
3.3.3 3D CNN for Matching Cost Estimation . . . . .	27
3.3.4 Disparity Computation . . . . .	28
3.4 Loss Function . . . . .	29
3.4.1 Disparity Loss . . . . .	29

3.4.2	Variance Loss . . . . .	29
3.4.3	Warp Loss . . . . .	30
3.5	Disparity Refinement . . . . .	30
3.6	3D Reconstruction . . . . .	31
3.7	Datasets and networks' training procedure . . . . .	31
3.8	Evaluation of 3D reconstruction's precision . . . . .	32
3.8.1	Re-Projection Errors . . . . .	32
3.8.2	Comparison to Tomography . . . . .	32
3.8.3	3D CNN's precision evaluation . . . . .	34
3.9	Additional network training with GAN-SPADE . . . . .	35
3.9.1	GAN-SPADE network's principle . . . . .	37
3.9.2	Synthetic dataset generation . . . . .	37
3.10	Concluding remarks . . . . .	39
<b>4</b>	<b>Tilt-less 3D imaging and reconstruction of dislocations</b>	<b>41</b>
4.1	Tilt-less 3D imaging principle . . . . .	42
4.2	3D imaging and reconstruction with objective aperture displacement . . . . .	43
4.3	One-shot 3D imaging using segmented detector . . . . .	45
4.3.1	Crystallographic coordinate system for 3D reconstruction . . . . .	48
4.4	Tilt-less 3D imaging and reconstruction using pixelated detector . . . . .	48
4.4.1	4D-STEM experimental procedure . . . . .	49
4.4.2	3D reconstruction by deep learning neural networks . . . . .	50
4.4.3	Network training with 4D STEM images . . . . .	51
4.4.4	Convergence angle maximum . . . . .	52
4.5	Concluding remarks . . . . .	54
<b>5</b>	<b>Quantification of 3D reconstruction</b>	<b>55</b>
5.1	Introduction . . . . .	55
5.2	Quantification of various STEM imaging conditions . . . . .	59
5.2.1	Excitation error ( $s_g$ ) . . . . .	60
5.2.2	Detectors' collection semi-angle $\beta$ . . . . .	63
5.2.3	Pixel size and time . . . . .	65
5.3	Quantification of the results from segmented detector . . . . .	67
5.3.1	$\beta_{in}$ . . . . .	68
5.3.2	Pixel size and time . . . . .	69
5.4	Quantification of the results from pixelated detector . . . . .	70
5.4.1	Pixel size and time . . . . .	70
5.4.2	Radius of a "virtual" detector . . . . .	72
5.5	Concluding remarks . . . . .	74



---

<b>6</b>	<b>3D distribution of nanoparticles</b>	<b>75</b>
6.1	Introduction . . . . .	75
6.2	Material system and sample preparation . . . . .	76
6.3	Cryo-STEM 3D imaging with segmented detector . . . . .	77
6.4	Detection and 3D reconstruction . . . . .	77
6.4.1	Denoising . . . . .	78
6.4.2	Detection . . . . .	79
6.4.3	3D reconstruction . . . . .	80
6.5	Radial distribution analysis . . . . .	81
6.5.1	Comparison to tomography . . . . .	82
6.6	Application to other samples . . . . .	84
6.6.1	Sample with a high concentration of nanoparticles . . . . .	84
6.6.2	Shortened nanoparticle agglomerates . . . . .	85
6.6.3	Long nanoparticle agglomerates . . . . .	86
6.7	Cryo-STEM 3D imaging with pixelated detector . . . . .	86
6.7.1	Detection technique . . . . .	87
6.7.2	3D reconstruction and RDA . . . . .	89
6.7.3	Large convergence semi-angle . . . . .	90
6.7.4	Application to other samples . . . . .	91
6.8	Concluding remarks . . . . .	93
<b>7</b>	<b>Conclusion</b>	<b>95</b>
7.1	Achieved results . . . . .	95
7.2	Outlook . . . . .	97
	<b>Bibliography</b>	<b>107</b>
	<b>Curriculum Vitae</b>	<b>109</b>



# List of Figures

2.1	Scanning electron microscopy (SEM) images showing TEM lamella preparation technique using FIB milling. (a) Removing the material around the region of interest in the bulk sample of TiAl alloy. (b) Transferring the region of interest to a TEM support grid using a micro-manipulator in the FIB. (c) Final overview of the prepared TEM lamella glued on the TEM support grid. . . . .	8
2.2	Bright-field (BF) STEM images of TiAl alloy prepared by (a) FIB. (b) Electropolishing. (c) Electropolishing in combination with BIB milling. . . . .	9
2.3	(a) Initial semi-cylindrical bulk sample of TiAl alloy, (b) Schematic representation of the bulk sample, (c) Surfaces of the semi-cylindrical sample used for the sample preparation by electropolishing technique. The diameter of the final TEM foil samples is 3 mm. . . . .	10
2.4	Ti-Al binary phase diagram [46]. The vertical blue line corresponds to the composition of the bulk material Ti-46.8Al-1.7Cr-1.8Nb (at.%) used for this research.	11
2.5	Unit cells sketches for two phases of TiAl alloy: (a) $\gamma$ -phase unit cell with the lattice parameter $a=0.4\text{nm}$ , $b=0.4\text{nm}$ , and $c=0.405\text{nm}$ , the theoretical ratio for Ti/Al is equal to 1. (b) $\alpha_2$ -phase unit cell with the lattice parameter $a=0.577\text{nm}$ , $b=0.577\text{nm}$ , and $c=0.462\text{nm}$ , the theoretical ratio for Ti/Al is equal to 3. Green and red spheres represent Ti and Al atoms respectively. . . . .	12
2.6	Orientation-phase mapping of the electropolished TiAl TEM samples: (a) Bulk sample's scheme with crystallographic axes of $\gamma$ -phase, (b) Virtual BF image of the region of interest, highlighted by a white cross in (a), (c) Corresponding phase map, where red areas represent $\gamma$ -TiAl and green areas are $\alpha_2$ -phase precipitates.	13
2.7	EDX analysis results for the FIB sample of the TiAl alloy: (a) BF-STEM image of the region for quantitative analysis, (b) STEM-EDX map of Ti, (c) STEM-EDX map of Al, (d) STEM-EDX map of Cr, (e) STEM-EDX map of Nb. . . . .	14
2.8	Schematic illustration of the STEM imaging with different detectors in the systematic row diffraction condition. . . . .	16
2.9	Dislocations in $\gamma$ -phase TiAl alloy experimentally imaged and simulated with CUFOUR software in two-beam diffraction condition $g=(002)$ with different TEM modes: (a) Bright-field TEM image, (b) Weak-beam dark-field TEM image, (c) Bright-field STEM image, (d) BF-TEM simulated image, (e) Weak-beam dark-field simulated image, (f) BF-STEM simulated image. . . . .	17

2.10 Tomographic 3D reconstruction utilizing SIRT and 45 BF-STEM images of dislocations in TiAl alloy: (a), (b) BF-STEM images of dislocations with $0^\circ$ and $30^\circ$ of tilt respectively, (c), (d) Tomogram visualization oriented to the same angle as images in their left, (e), (f) Tomogram visualization from the left and the right side views correspondingly, (g) Tomogram slice from the center of the depth volume. . . . .	19
2.11 Stereographic 3D visualization of dislocations in TiAl alloy utilizing anaglyphs made from aligned stereo-pairs of BF-STEM images acquired under various tilt angles. The value of the stereo-angle of each pair is displayed in the lower-left corner of the corresponding anaglyph. Best viewed in red-cyan glasses. . . . .	20
3.1 Stereo reconstruction processing steps. In the first step, images are aligned such that the tilt axis is vertical and at the image center. Dislocation segments are detected using UNet [57] in the second stage. Later, features of UNet are provided to a 3D CNN in order to compute horizontal disparity between corresponding dislocation segments. At the final stage, the depth value for every detected dislocation pixel is computed using disparity estimations. Green blocks in the figure represent the stages that are learned from annotated training data. . . . .	24
3.2 Stereo Contour Detection and Matching Network architecture. Layers with learnable parameters are shown in blue. Feature volume, $V_f$ , and cost volume, $V_c$ , are depicted as gray and green 3D volumes respectively . . . . .	26
3.3 Representative BF-STEM image of dislocations in a TiAl alloy thin foil in two-beam diffraction condition with $\mathbf{g}=(002)$ (a) and corresponding detected dislocations (b). The detection network manages to detect dislocations having complex shapes even in noisy images while still being able to reject unrelated dark sections of the image. . . . .	27
3.4 Feature volume construction is shown from the top view. For each pixel in the left image, the features of this pixel and candidate pixels for a match in the right image are back-projected to 3D and concatenated to form feature volume. For a specific pixel at location $(u, v)$ in the left image and a candidate pixel at location $(u + d, v)$ , the back-projected point in feature volume is depicted as a blue circle in the figure. The value $d$ for the given pixel is the disparity level that defines the depth of the pixel with respect to the center image plane. . . . .	28
3.5 3D Reconstruction of dislocation networks in TiAl alloy shown in Fig.3.3 . . . . .	31
3.6 Re-projections to other views. Estimated 3D dislocations in the TiAl sample that are reconstructed using a stereo-pair with $8^\circ$ separation are re-projected to views with $-44^\circ$ , $-6.39^\circ$ , $+8^\circ$ , and $+44^\circ$ tilt angles. In the top row of images, four views are shown with green marks being 3D dislocation points re-projected onto raw images. In the bottom row, the dislocation ground-truths for these views are shown. For all presented views, it can be seen that re-projections of the estimated 3D structure are consistent with raw images and human-annotated dislocations ground truth. . . . .	33

3.7	Comparison of reconstruction results of stereo approach and tomography. TiAl sample region previously shown in Fig.3.6 is reconstructed by tomography (shown in white) utilizing full image sequence with 45 images covering the angular range $(-48^\circ, 50^\circ)$ and by stereo CNN method with stereo images having $2^\circ$ in between (shown in yellow). . . . .	33
3.8	Two 3D tomography reconstruction techniques across an increasing number of images given as input compared to the stereo method using two images as input. Images are sampled regularly for each case of tomographic reconstruction from the sequence with 45 images spanning angular range $(-48^\circ, 50^\circ)$ . . . . .	34
3.9	Synthetic dislocation dataset generation pipeline using GAN-SPADE deep learning neural network: (a) Skeletonized 3D reconstruction from the manually labeled training dataset, (b), (c) 2D projections of (a) given as an input to pre-trained (d) GAN-SPADE, (e), (f) Synthetically generated dislocations from semantic layouts (b) and (c). . . . .	38
3.10	(a), (b), (c), (d) Synthetically generated dislocation images by GAN-SPADE network and (e), (f), (g), (h) corresponding semantic layout that was given to the network as an input. . . . .	38
4.1	Schematic illustration of the tilt-less 3D imaging technique: (a) Imaging with an inclined direct beam (imaging beam 1 and 2), colored in red and orange: an aperture in the back focal plane (BFP) is placed on the edge of the directly transmitted disk, which is collected by an annular detector. (b) Imaging with a conical beam along the optical axis, colored in blue: the BFP aperture is removed, and the on-axis BF detector receives the center of the direct disk. (c) Illustration of the convergent beam electron diffraction (CBED) pattern corresponding to the diffraction condition shown in (a). Orange and red circles indicate the position of the BFP aperture for imaging conditions of beams 1 and 2, respectively. Courtesy of Emad Oveisi [9]. . . . .	42
4.2	Tilt-less 3D imaging workflow with objective aperture displacement: (a) STEM diffraction pattern in two-beam diffraction condition with yellow masks representing objective aperture positions, Stereo-pair of BF-STEM images (b) and (c) recorded from the two positions of the TEM objective aperture in the BFP (a), resulting anaglyph of the dislocations in TiAl alloy (d). Best viewed with red-cyan glasses. . . . .	44
4.3	3D reconstruction pipeline from the tilt-less 3D imaging with objective aperture displacement: (a), (b) BF-STEM stereo-pair with $1.4^\circ$ of stereo-angle, (c), (d) Corresponding segmentation by UNet neural network, (e) Final 3D reconstruction by 3D CNN. . . . .	44
4.4	Single-shot 3D imaging scheme with segmented detector: electron probe with convergence angle $\alpha$ is scanning pixel by pixel the sample with dislocations, transmitted beam is recorded in the segmented detector with four quadrants: A, B, C, and D, allowing to acquire four STEM images simultaneously. . . . .	46

- 4.5 Tilt-less 3D imaging and reconstruction of dislocations workflow using a segmented detector with four quadrants: (a) Segmented detector's scheme superimposed with the STEM diffraction pattern in two-beam diffraction condition, where two opposite sides of the BF disc with the same excitation error cover two opposite segments B and D of the segmented detector, (b) Stereo-pair STEM images of dislocations in TiAl alloy acquired from the segments B and D, (c) Corresponding segmentation results by pre-trained UNet network, (d) Final 3D reconstruction of dislocations performed by 3D CNN in the crystallographic coordinate system. . . . . 47
- 4.6 Tilt-less 3D imaging of dislocations in TiAl alloy using  $150\mu\text{m}$  condenser aperture with segmented detector: (a) Virtual phase plate of the electron beam from the probe corrector software acquired with the  $70\mu\text{m}$  condenser aperture, (b), (c) Stereo-pair STEM images of dislocations in TiAl alloy acquired with 60 mrad convergence angle from the segments B and D, (d), (e) Corresponding segmentation results by pre-trained UNet network. . . . . 48
- 4.7 4D-STEM imaging workflow with pixelated detector: (a) Schematic illustration of 4D STEM imaging on a pixelated detector with (256, 256) pixels, (b) Averaged scan region in a real space, (c) Calibrated diffraction pattern in a reciprocal space integrated from the red rectangular at (b), (d) Four "virtual" detector positions on the diffraction pattern, (e) and (f) - Virtual BF-STEM images from left and right detector positions, (g) and (h) - Virtual BF-STEM images from top and bottom detector positions along the Kikuchi line at the (d). Stereo-angle between each pair of images is 6.88 degrees. . . . . 50
- 4.8 3D reconstruction pipeline from images acquired with pixelated detector: (a) Stereo-pair of dislocations in TiAl alloy created from 4D-STEM dataset, (b) Segmentations of stereo-pair in (a) by UNet neural network with detected dislocation lines, (c) 3D reconstruction from detected dislocations in (b) by 3D CNN in the crystallographic frame of reference. Stereo-angle is  $6.54^\circ$ . . . . . 51
- 4.9 Training dataset creation from 4D-STEM dataset: (a) Diffraction pattern in two-beam condition projected on the pixelated detector with circles representing "virtual" detectors with various radii and same coordinates of the circles' center, (b) Labeled virtual BF-STEM image of dislocations in TiAl, (c)-(h) Virtual BF-STEM images created from circles in (a) with radii 5, 10, 15, 20, 30, 40 pixels correspondingly. . . . . 52
- 4.10 Automatic 3D reconstruction from STEM images acquired with pixelated detector: (a) Virtual BF-STEM stereo-pair of dislocations in TiAl alloy, (b) Detected from (a) dislocations by UNet neural network, (c) 3D reconstruction by 3D CNN in the crystallographic frame of reference and nm-scale. Stereo-angle between the images is  $9.32^\circ$ . . . . . 53

5.1	Grayscale images obtained from different types of filtrations. For visibility reasons, a colored map was chosen to represent grayscale values. The original binary image (a) was used to illustrate filtrations: (b) height filtration with vector (-1,-1), (c) the radial filtration with the center in the blue leaf, (d) density filtration, (e) dilation filtration. Courtesy of Adélie Garin, [76]. . . . .	56
5.2	Dilation filtration example: (a) on a manually labeled ground-truth image and (b) on a UNet segmentation of experimentally acquired STEM image of dislocations in TiAl alloy, (c) and (d) corresponding persistence diagrams, (e) topological score of the ground-truth image (a) and UNet segmentation of experimental STEM image (b) for the dilation filtration. . . . .	58
5.3	Schematic representation of the positive excitation error $s_g$ in two-beam diffraction condition. . . . .	60
5.4	Quantification procedure of various $s_g$ : (a) Aligned STEM images of dislocations in TiAl alloy acquired with different values of $s_g$ and their corresponding diffraction patterns in two-beam diffraction condition, (b) Segmentation results from the pre-trained UNet neural network, (c) Manually annotated ground-truth, (d) TDA results representing “topological” distance for H0 and H1 for each filtration utilized. . . . .	61
5.5	Final topological score calculation: (a) and (b) TDA results representing “topological” distance for H0 and H1 respectively for each filtration utilized with assigned weights and minimized errors, (c) Final scores with Image N.2 highlighted as the topologically closest to the ground-truth. . . . .	62
5.6	Quantification of the various detector’s collections angles $\beta$ , as a function of CL: Image N.0 - manually labeled ground-truth (GT), BF-STEM images of dislocations N.1-11 acquired on the BF detector, BF-STEM images of dislocations N.12-16 acquired on the HAADF detector, and corresponding detected dislocations from UNet neural network with TDA quantification results. . . . .	63
5.7	Quantification procedure of the STEM image’s pixel size: (a) BF-STEM images of dislocations in TiAl alloy acquired with different values of the pixel size, (b) corresponding segmentations from UNet neural network, (c) manually labeled ground-truth, (d) TDA quantification results. . . . .	66
5.8	Quantification procedure of the STEM image’s dwell time: (a) BF-STEM images of dislocations in TiAl alloy acquired with different values of the dwell times, (b) corresponding segmentations from UNet neural network, (c) manually labeled ground-truth, (d) TDA quantification results. . . . .	67
5.9	Quantification procedure of the BF-STEM images acquired on a segmented detector with three different values of $\beta_{in}$ as a function of CL: TDA results demonstrate that image N.2 obtained the highest topological score and proximity to the ground-truth (GT) image. . . . .	68

5.10	Quantification procedure of the BF-STEM images acquired on a segmented detector with different values of dwell time (a) and pixel size (e): after comparison of the corresponding segmentation images from UNet (b) and (f) to the manually labeled ground-truth images (c) and (g), TDA results demonstrated that images with $8\mu\text{s}$ of dwell time and 1.9nm of pixel size (highlighted by red circles in (d) and (h)) obtained the highest topological score to the ground-truth images. . .	69
5.11	Quantification procedure of the virtual BF-STEM images of dislocations acquired on a pixelated detector with different dwell times (a) and pixel sizes (e): (b) and (f) corresponding segmentations from UNet neural network, (c) and (g) manually labeled ground-truth images, (d) and (h) TDA quantification results. . . . .	71
5.12	Quantification procedure of the virtual BF-STEM images acquired on a pixelated detector with different radii of the "virtual" detectors with centers at $4.66^\circ$ of virtual tilt: (a) virtual BF-STEM images of dislocations in TiAl alloy obtained with different values of "virtual" detectors' radii, (b) corresponding segmentations from UNet neural network, (c) manually labeled ground-truth, (d) TDA quantification results. . . . .	73
6.1	Schematic illustration of the single-shot 3D tilt-less imaging of nanoparticles in vitrified ice with the segmented detector with four BF-STEM images acquired simultaneously from segments A, B, C, and D. . . . .	78
6.2	3D reconstruction pipeline of nanoparticles imaged on a segmented detector: (a) An example of BF-STEM image (from the segment A), (b) Result of the edge detection after denoising the image (a), (c) Detected nanoparticles highlighted by red circles, (d) Final 3D reconstruction after application of the steps (b) and (c) on all four images from segments A, B, C, and D (shown in Fig. 6.1). . . . .	79
6.3	3D reconstruction of nanoparticles in vitrified ice: (a) STEM images from A, B, C, and D regions of the segmented detector (shown clockwise) with detected particles shown in red circles. For a chosen particle in region A (depicted in a yellow circle), correspondences are searched on line segments shown as yellow lines in B, C, and D images. (b) If consistent detections are found in all 4 images, a suitable depth value is assigned to the particle. . . . .	80
6.4	Radial distribution function $g(r)$ of the nanoparticles in vitrified ice with 10mg/ml concentration obtained from the 3D reconstruction in Fig. 6.3 (b). . . . .	82
6.5	Radial distribution function $g(r)$ of the nanoparticles in vitrified ice with 10mg/ml concentration obtained from the 3D reconstruction by 3D tilt-less imaging in STEM mode (with the stereo-angle of $3^\circ$ ) and from the TEM tilt series. . . . .	83
6.6	Radial distribution analysis of nanoparticles with a high concentration: (a) BF-STEM image of dispersed nanoparticles (segment A) in vitrified solution with 40mg/ml concentration, (b) 3D reconstruction using all four views by the 3D tilt-less imaging technique, (c) Radial distribution function $g(r)$ of the nanoparticles. . . . .	84



6.7	Radial distribution analysis of nanoparticles forming shortened agglomerates in a vitrified solution: (a) BF-STEM image of agglomerated nanoparticles (segment A) in vitrified solution with 10mg/ml concentration, (b) 3D reconstruction using all four views by the 3D tilt-less imaging technique, (c) Radial distribution function $g(r)$ of the nanoparticles. . . . .	85
6.8	Radial distribution analysis of nanoparticles forming long agglomerates in a vitrified solution: (a) BF-STEM image of agglomerated nanoparticles (segment A) in vitrified solution with 10mg/ml concentration, (b) 3D reconstruction using all four views by the 3D tilt-less imaging technique, (c) Radial distribution function $g(r)$ of the nanoparticles. . . . .	86
6.9	4D-STEM cryo-imaging workflow with pixelated detector: a) Schematic illustration of the 4D-STEM imaging of nanoparticles in vitrified solution on the pixelated detector with (256, 256) pixels, b) Calibrated diffraction pattern in reciprocal space with four "virtual" detectors with 30, 40, and 50 pixels radii and the same coordinate of a center, c) Four virtual BF-STEM images obtained from the corresponding "virtual" detectors in b) with 50 pixels radii. . . . .	87
6.10	3D reconstruction pipeline of nanoparticles in a vitrified solution imaged on a pixelated detector: (a) An example of virtual BF-STEM image obtained from the 4D-STEM dataset from a "virtual" detector with 50 pixels of radius, (b) Image (a) after applying thresholding operation, (c) Detected on thresholded image contours drawn on an original STEM image, (d) 3D reconstruction after performing steps (b)-(c) on all four virtual STEM images extracted from the 4D dataset. Stereo-angle in each stereo-pair is $3^\circ$ . . . . .	88
6.11	Radial distribution analysis of nanoparticles with 10 mg/ml of concentration: (a) an example of virtual BF-STEM image of nanoparticles extracted from 4D-STEM dataset with 70 pixels radius of "virtual" detector, (b) 3D reconstruction by 3D tilt-less imaging technique using four virtual BF-STEM images, (c) Radial distribution function $g(r)$ of the nanoparticles calculated from the 3D reconstruction. . . . .	90
6.12	3D reconstruction procedure of virtual BF-STEM images acquired with 60 mrad of convergence semi-angle: (a) an example of virtual BF-STEM image of nanoparticles extracted from 4D-STEM dataset with 80 pixels radius of "virtual" detector, (b) Image (a) after applying thresholding operation, (c) Detected on thresholded image contours drawn on an original STEM image, (d) 3D reconstruction after performing steps (b)-(c) on all four virtual STEM images extracted from the 4D dataset. Stereo-angle in each stereo-pair is $6^\circ$ . . . . .	91
6.13	Radial distribution analysis of nanoparticles with 40 mg/ml of concentration: (a) an example of virtual BF-STEM image of nanoparticles extracted from 4D-STEM dataset with 70 pixels radius of "virtual" detector, (b) 3D reconstruction by 3D tilt-less imaging technique using four virtual BF-STEM images, (c) Radial distribution function $g(r)$ of the nanoparticles calculated from the 3D reconstruction. . . . .	92

- 6.14 Radial distribution analysis of nanoparticles with 2.5 mg/ml of concentration: (a) an example of virtual BF-STEM image of nanoparticles extracted from 4D-STEM dataset with 70 pixels radius of "virtual" detector, (b) 3D reconstruction by 3D tilt-less imaging technique using four virtual BF-STEM images, (c) Radial distribution function  $g(r)$  of the nanoparticles calculated from the 3D reconstruction. 92
- 7.1 Multiple views of the 3D volume generated by the NeuS network, utilizing (multiple) STEM images of dislocations as an input. Light grey lines correspond to the dislocation structures, and dark grey regions to the grain boundaries reconstructed from the STEM images. . . . . 98

# List of Tables

3.1	Depth estimation errors (in pixels) for stereo setups with different angle separations. For all experiments, the network is trained using the loss function that combines all three loss terms. Results presented without the refinement stage of section 3.5 and with it. . . . .	35
3.2	Comparison of disparity estimation with different combinations of loss terms. Results are presented for three subsets of test data. Stereo pairs with $8^\circ$ angular range are used for the experiments. . . . .	36
5.1	BF and HAADF STEM detectors collection semi-angles $\beta$ (in mrad) as a function of camera length for the sequence of images acquired in Fig. 5.6. . . . .	64





# 1 Introduction

Modern transmission electron microscopy (TEM) is currently revolutionizing the field of imaging of nanosized objects in the domains of biology, material science, and many other disciplines. TEM becomes more and more powerful and can produce high-resolution imagery in large quantities. The resolution strength of modern TEM noticeably improved in recent years resolving the features with less than one Å in size.

TEM enables researchers to study the fine details of material microstructure and the arrangement of atoms in crystal structures and can be used to study a wide range of materials, including metals, ceramics, polymers, and biological samples. TEM is not only a high-resolution imaging tool, but also a powerful analytical tool that can be used to determine chemical composition, crystal structure, and other properties of materials at the nanoscale. With the growing interest in nanotechnology and the development of advanced materials, the demand for TEM and related tools such as image processing software, and analysis tools is increasing rapidly.

However, TEM delivers a two-dimensional (2D) projection of the sample under consideration while many areas of physical and biological sciences now require 3D reconstructions of nanosized objects.

Among important structures that require to be visualized in 3D, are dislocations, which are curvilinear, one-dimensional crystallographic defects in materials that represent irregularities in the periodic arrangements of the atoms. They play an important role in the mechanical, magnetic, electrical, and optical properties of the material [1], [2]. To investigate the interaction between dislocations and second-phase particles or other planar defects one needs to study the configuration of the curved dislocation line or more complex dislocation network.

Understanding the 3D distribution of dislocations is important for several reasons:

- Understanding the behavior of dislocations: Dislocations are the primary carriers of plastic deformation in materials. By knowing their configurations, researchers can better understand how materials deform under stress and how dislocations interact with each

other, which can affect the overall mechanical properties of the material [3], [4].

- **Improving material design:** The 3D distribution of dislocations can be used to design new materials with improved mechanical properties. By manipulating the density and distribution of dislocations, it is possible to tailor the mechanical properties of the material to suit specific applications [5].
- **Predicting material failure:** Dislocation interactions can lead to the formation of cracks, which can propagate and lead to catastrophic failure of the material. By understanding their 3D distribution, researchers can develop models to predict the onset of failure in materials and improve their safety [6], [7].

Development of the TEM imaging techniques allowed to observe and study these crystallographic defects in more detail. However, as TEM micrographs represent the 2D projection of the sample where the missing information along the incident beam direction is lost, the 3D structure of the dislocation lines is not clear. Conventionally, to recover the missing 3D information of the dislocation networks a tomographic 3D reconstruction technique is used. This is an intensity-based 3D reconstruction technique, where multiple images of dislocations are acquired over a wide range of tilt angles [8]. Due to the instrument's limitations regarding the tilting angular range, it is not possible to acquire images of the sample from all the views, therefore it creates uncertainties in the final 3D reconstruction, known as the missing wedge problem. It is also caused by the fact that the tomography technique using Weighted Back-Projection (WBP) or Simultaneous Iterative Reconstruction Technique (SIRT) algorithms performs the 3D reconstruction in a structure-unaware manner. Decreasing the tilting range causes elongation and thickening of the dislocation lines in the final 3D reconstruction, and it has been demonstrated that SIRT reconstruction with TEM images of less than  $10^\circ$  of tilt range is providing an unsatisfactory 3D reconstruction which is difficult to interpret [9].

Utilizing geometric and discrete reconstruction methods for tomography incorporating geometric prior knowledge or the discrete number of grey levels about the reconstruction subject has shown to be a successful approach to overcoming the missing wedge problem and reducing the number of images from different viewing angles [10]–[12]. Other reconstruction algorithms, such as total variation minimization (TVM), utilize an alternative type of prior knowledge by assuming that the reconstructed object possesses a sparse gradient at the nanometer scale [13]. This assumption holds merit within the nanoscale domain where the valid presumption of sharp boundaries between distinct compounds often exists, resulting in a sparse gradient for the object. This technique was previously employed for 3D reconstruction of various nanoparticle types [14], [15]. Alternatively, it was evidenced that the utilization of reconstruction algorithms based on compressed sensing (CS) techniques and a phase-field approach enhances the quality of limited-angle tomographic reconstructions, as well as suppresses the artefacts [16]–[18]. In particular, dynamic CS algorithms were developed to perform updating real-time tomographic reconstruction through the continuous acquisition of new specimen projections [19].

Another challenge of performing the 3D imaging of dislocations via the acquisition of tilt series comes from the crystallographic nature of these defects in a specimen. When tilting the crystalline sample it is necessary to preserve a particular diffraction condition in order to maintain the contrast of dislocations and the image background uniform [20].

In the case of one-dimensional defect imaging stereo 3D reconstruction proved itself an acceptable alternative technique compared to laborious tomography. It has been demonstrated that only two images acquired from two different tilt-angles (i.e. stereo-pair) are sufficient to obtain a precise 3D reconstruction of dislocations [21], [22]. Even a 3D reconstruction of dislocations from a single electron micrograph was performed, using the knowledge of the sample's crystallographic orientation and the limited number of defect configurations in the FCC (face-centered cubic) structured material [23].

In order to perform 3D visualization of dislocations from a stereo-pair, algorithms based on classical computer vision techniques were developed [9]. It allowed to obtain stereo 3D reconstruction of dislocations from scanning TEM (STEM) images in a semi-automated manner by tracing dislocation with the help of a microscopy user on both views and then performing matching of corresponding points and triangulation.

However, all developed state-of-the-art methods for stereo 3D imaging and reconstruction of 1D curvilinear features in TEM images rely heavily on manual intervention to a certain extent: manual or semi-automated tracing of the dislocation lines, matching corresponding points, or extended prior knowledge about the sample microstructure. This severely restricts the amount of data that can be processed and interpreted.

Nowadays artificial intelligence is already conquering the field of data treatment in TEM and improving the acquisition of data [24]. For example, deep convolutional neural networks (CNNs) trained on position averaged convergent beam electron diffraction (PACBED) patterns allowed to perform their analysis in an order of magnitude faster than conventional methods while maintaining the accuracy of the measurements [25]. Deep CNNs were also applied to perform the semantic segmentations of various defects in steels: dislocation lines, precipitates, and voids [26]. It has been demonstrated that this automatic approach exceeds the mean performance of human experts, introducing a workflow that holds great promise for fast and statistically significant quantification of materials defects. Automatic segmentation algorithms based on deep learning neural networks were also applied to atomically resolved TEM images and proven to be able to successfully detect individual atoms and atomic columns on the noisy and unprocessed data [27].

In the growing field of biological specimen imaging in TEM, where the signal-to-noise ratio is typically low, neural networks found applications in denoising raw experimental datasets. In particular, progress has been made in the 3D reconstruction of STEM bio-images utilizing the Neural Radiance Fields (NeRF) algorithm [28]. Neural Radiance Fields (NeRF) is a type of deep learning algorithm for synthesizing high-quality 3D models of real-world scenes from 2D images. By learning the specifics of the noise in STEM images of biological specimens, it was



possible to successfully separate 3D signal and noise without supervision and obtain precise 3D reconstructions of cells infected with SARS-CoV-2. Deep learning algorithms were also successfully implemented in removing imaging artifacts, associated with charge damage, and producing denoised outputs [29].

Recently, advancements are made not only in post-processing algorithms for S/TEM but also in new hardware devices. The development of novel detectors in STEM is an active area of research, with applications in materials science, nanotechnology, and biological imaging. Consequently, significant improvements were produced in imaging speed, sensitivity, and resolution. In particular, the development of direct electron detectors (DEDs) has greatly contributed to the recent advancements in cryo-EM, allowing for the determination of high-resolution structures of biological molecules and complexes that were previously challenging or impossible to study using traditional methods. Recent progress in pixelated detector technology further revolutionizes STEM imaging, mainly in the field of material science [30]. These detectors with high detective quantum efficiency (DQE) allow to acquire the four-dimensional (4D) datasets, that are used for virtual diffraction imaging, orientation, and strain mapping, measurements of thickness and tilt of samples [31]. Pixelated detectors also opened new perspectives in phase contrast imaging methods, like ptychography, that enable the recovery of both amplitude and phase information of a sample, to form an image with much higher resolution than can be achieved by traditional microscopy techniques.

## Motivations

The goal of the project named *Synergistic Approach to Capturing and Exploiting Microscopy Images (SCEM)* aims at the automatic and fast 3D reconstruction of one-dimensional and curvilinear structures just from a few TEM micrographs (projections) using a novel deep-learning neural network approach as well as optimization and improvement in the acquisition of the TEM images, where images are acquired in a manner that the automated reconstruction tools are most effective.

Jointly, the progress in the field of deep learning algorithms and improvements in the STEM detector technology allows for overcoming the barriers present in the past. In this work, an effort will be made in the development of 3D imaging techniques and image analysis methods for automated 3D reconstruction of point-like and one-dimensional curvilinear structures that appear in electron microscopy images. It is important to optimize both 3D imaging techniques and algorithms to work with each other to take maximum advantage of modern electron microscopes and detectors. For this, tools from topology analysis will be implemented to analyze neural network outputs of the STEM images acquired with various imaging conditions in order to select the ones that are preferable for neural networks. This analysis will allow to perform 3D reconstruction via neural networks with high precision. In combination with the development of the stereo 3D reconstruction algorithms, the process of data acquisition and post-treatment can be drastically accelerated in comparison to conventional tomography, and ultimately, replace it. Acquisition of a stereo-pair can be further optimized by utilization of

novel tilt-less 3D imaging technique in STEM mode, developed earlier at EPFL [32]. Applying this method on fast segmented and pixelated detectors will allow to simultaneously acquire a stereo-pair at a single sample tilt. There are many potential applications of this approach where it is required to obtain 3D reconstructions of nanosized objects. In particular, tomography can be replaced in the field of cryoET, where previously scientists utilized electron tomography imaging and reconstruction techniques to obtain the 3D distribution of nanoparticles in a vitrified solution. Also, due to the possibility of fast acquisition of a stereo-pair with this approach, there is great potential in the investigation of dynamical processes in the 3D volume of the specimens, and for 3D imaging of radiation-sensitive materials.

### **Objectives and structure of the thesis**

The goal of the SCEM project is to optimize electron microscopy 3D imaging techniques and post-processing methods to work together and to deliver to the community the opportunity to treat a large amount of data and automatically extract useful information from 2D images.

This thesis consists of six chapters. Current Chapter 1 is the Introduction to the thesis with an overview of current state-of-the-art techniques for 3D electron imaging and reconstruction, along with the implementation of modern AI methods for electron microscopy and post-processing.

Chapter 2 is dedicated to the material selection and methods used in this work for sample preparation, analysis, and imaging.

In Chapter 3 novel approach for automatic 3D reconstruction of curvilinear 1D structures from the electron microscopy stereo-pairs is proposed. The method is based on deep learning neural networks.

Chapter 4 is assigned to the tilt-less 3D imaging technique and improvement done in this field with the development of modern STEM detectors and Cs-corrected electron microscopes.

Chapter 5 is dedicated to the quantification of various STEM imaging conditions using a topological analysis tool that allows the selection of the optimal conditions for dislocation STEM imaging and following 3D reconstruction.

Chapter 6 describes the application of the tilt-less technique to the new material system, specifically to determine the 3D distribution of the nanoparticles in vitrified ice via a single acquisition. 3D STEM imaging in cryo-condition was performed for the first time along with the 3D reconstruction using a classical computer vision approach.

Chapter 7 presents achieved results and future developments that will improve further the 3D reconstruction of point-like and curvilinear 1D structures.

This thesis was financially supported by the Swiss National Science Foundation (SNSF), project No. 177237.



## 2 Materials and methods

In this chapter, I will introduce the main information about the selected material with one-dimensional curvilinear defects as well as the analysis methods. Common sample preparation techniques of the metallic alloys will be discussed together with the microstructure analysis of the titanium aluminide TiAl alloy, using TEM diffraction, chemical analysis, and orientation mapping with the precessed probe. Then the advantages of STEM imaging of the dislocations and simulations of the dislocation contrast in conventional TEM and STEM imaging modes will be presented. Tomographic reconstruction of dislocations from STEM images will be presented further and the advantages of stereo 3D reconstruction for curvilinear structures will be discussed.

### 2.1 Materials

Titanium aluminide TiAl alloy was chosen as the main material to study dislocations' distribution in the 3D volume of the sample. Titanium aluminide has three major intermetallic compounds:  $\gamma$ -TiAl,  $\alpha_2$ -Ti<sub>3</sub>Al, and TiAl<sub>3</sub>. Among all the three compounds,  $\gamma$ -TiAl has acquired the most interest for high-temperature applications, especially in aeronautic and aerospace industries, racing applications [33]–[35]. It has several advantages: mechanical properties including elastic stiffness and high-temperature strength are high, it has good oxidation resistance, high microstructural stability during long-term thermal exposure, and a low density, around 4g/cm<sup>3</sup> [33], [35]–[39].

For microstructural investigation of an annealed TiAl-based alloy, firstly, a proper sample preparation method should be found among focus ion beam lamella extraction, electropolishing, and ion milling.

## 2.2 Sample preparation

Sample preparation is a crucial step for 3D electron imaging of dislocations. The aim is to obtain electron transparent sections of different thicknesses – with an adequate number of dislocations – without introducing damage inside of the sample. In order to achieve clear visibility of dislocation networks and preserve initial dislocation structures in the material two sample preparation techniques were tested: focused ion beam (FIB) milling and mechanical polishing in combination with electropolishing.

### 2.2.1 FIB milling

Focused ion beam milling is a sample preparation technique where a beam of Ga ions with high energy is focused on the sample by electromagnetic lenses in order to mill the material around the region of interest and to obtain a thin electron transparent lamella [40].

For TEM lamella preparation from TiAl bulk material, first, a carbon film is deposited on one side of the materials to cover and protect the region for preparing the specimen. Then, we use a FIB with Ga source (FIB-SEM Zeiss NVision 40) to mill both sides so that it can be taken out by micromanipulator and glued on support where the final thinning takes place as depicted in Fig.2.1. For milling Ga ions with an energy of 30keV are used, then 5keV at the very end for fine polishing of the lamella. The thickness of the final lamella is approximately 200 nm.

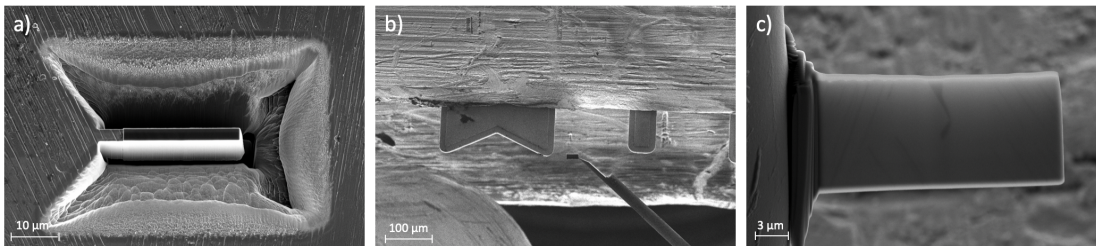


Figure 2.1: Scanning electron microscopy (SEM) images showing TEM lamella preparation technique using FIB milling. (a) Removing the material around the region of interest in the bulk sample of TiAl alloy. (b) Transferring the region of interest to a TEM support grid using a micro-manipulator in the FIB. (c) Final overview of the prepared TEM lamella glued on the TEM support grid.

As an advantage, the FIB milling sample preparation technique has high positional accuracy. However, the ion beam can form defective, amorphous regions in the specimen and induce new defects in the material, for example, dislocation loops and new dislocations that can be seen in Fig. 2.2(a) [41], [42].

### 2.2.2 Electropolishing

The principle of electropolishing is the anodic dissolution of a pre-polished surface in an electrolyte bath. The machine pumps out a negatively charged electrolyte jet to hit the surface on both sides so that a thinned area is created until perforation of the specimen occurs and the operation is automatically terminated. A light signal is used to detect the hole in the specimen. When the receiver gets a certain intensity of light, the process is automatically stopped, and the audible alarm and reset light are activated [43].

To prepare an electron transparent foil from the bulk sample, the specimen was first mechanically thinned with diamond discs and then electropolished (electrolyte bath composition: 5 vol.% perchloric acid, 35 vol.% 1-butanol and 60 vol.% methanol; voltage: 35 V). Due to the low success rate for electropolished sample preparation, broad beam ion (BIB) milling with a few keV energy gallium ions is used to further decrease the thickness around the hole for unsuccessful samples with prevailing electron non-transparent regions. The main difference between focus ion beam milling and broad ion beam milling (BIB) is the ion beam source and its energy. FIB is done with highly focused and high-energy gallium ions (often 30 keV), while BIB milling is typically done with beams up to a few millimeters in diameter, with energies of up to a few keVs. On one hand, FIB has a higher positional accuracy that BIB milling cannot guarantee. On the other hand, BIB milling is less prone to cause damage or ion implantation than FIB. Therefore, after FIB cutting, BIB milling is often used to remove the damage created by FIB on the surface [44].

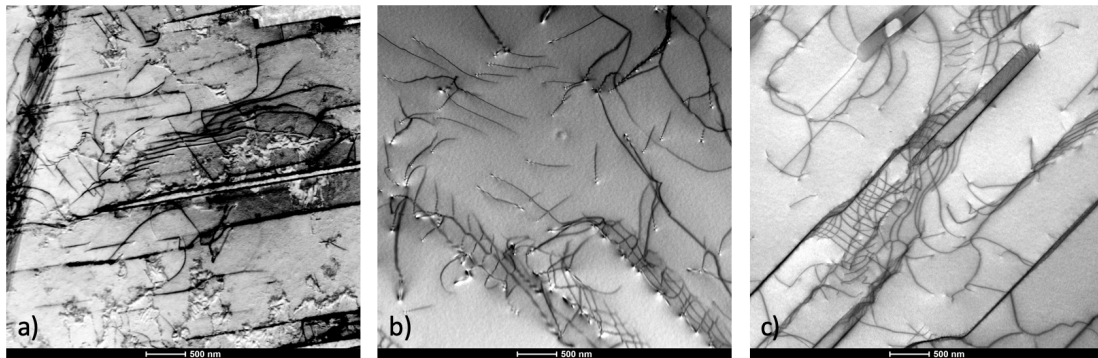


Figure 2.2: Bright-field (BF) STEM images of TiAl alloy prepared by (a) FIB. (b) Electropolishing. (c) Electropolishing in combination with BIB milling.

As we can observe in Fig.2.2 electropolished samples (b) and (c) have clear visibility of dislocation lines which is important for reconstruction purposes. At the same time, the sample prepared by FIB (a) shows a lot of induced defects and no sharp dislocation lines. The electropolishing technique is clearly the most promising one for our material system.

Electropolished TEM samples were prepared from the two sides of a semi-cylindrical bulk TiAl sample for the following microstructural analysis, illustration of the initial sample and surfaces used for sample preparation are depicted in Fig. 2.3. All together, 46 samples were

prepared for the following microstructural analysis from two sets of the two surfaces of the semi-cylindrical material: 30 TEM samples from the rectangle area and 16 samples from the base area, with each disc 3 mm in diameter.

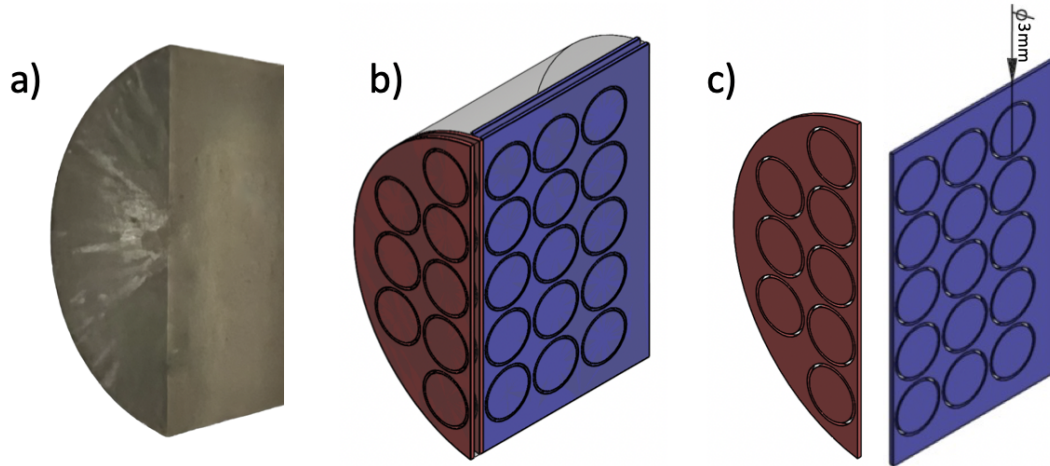


Figure 2.3: (a) Initial semi-cylindrical bulk sample of TiAl alloy, (b) Schematic representation of the bulk sample, (c) Surfaces of the semi-cylindrical sample used for the sample preparation by electropolishing technique. The diameter of the final TEM foil samples is 3 mm.

### 2.3 Microstructure of TiAl alloy

Engineering alloys based on the TiAl usually have Al concentrations of 45–48 at%. The composition of our bulk material is Ti-46.8Al-1.7Cr-1.8Nb (at.%). The binary atomic phase diagram is shown in Fig. 2.4, and the composition of this material corresponds to the blue line in the phase diagram. Therefore, at room temperature, this material contains two phases: ductile  $\gamma$ - and brittle  $\alpha_2$ -phases. As calculated from the phase diagram using the law of leverage, more than 80% of this material at room temperature is  $\gamma$ -phase without considering the influence of Nb and Cr.  $\gamma$ -phase, the dominant phase in this material, is composed of the tetragonal unit cell with  $L1_0$  intermetallic structure, while for  $\alpha_2$ -phase, the unit cell is hexagonal close packing (HCP) structure, sketches of the corresponding unit cells are depicted at the Fig. 2.5. The advantages mentioned above mainly concern the  $\gamma$ -phase and the main strengthening mechanism of this material is the solid solution strengthening precipitate hardening with  $\alpha_2$ -phase. As a result, the duplex alloy is more suitable for engineering applications. Cr is added to enhance the ductility of the material and Nb is added to strengthen and increase oxidation resistance [45].

Given that the  $\gamma$ -phase constitutes the principal phase in TiAl alloys, plastic deformation predominantly occurs on the  $\{111\}$  planes of the  $\gamma$ -phase through mechanisms such as dislocation glide or twinning under most conditions [47]. The primary dislocation types for this type of structure comprise ordinary dislocations with a Burgers vector  $\mathbf{B} = \frac{1}{2}\langle 110 \rangle$  and



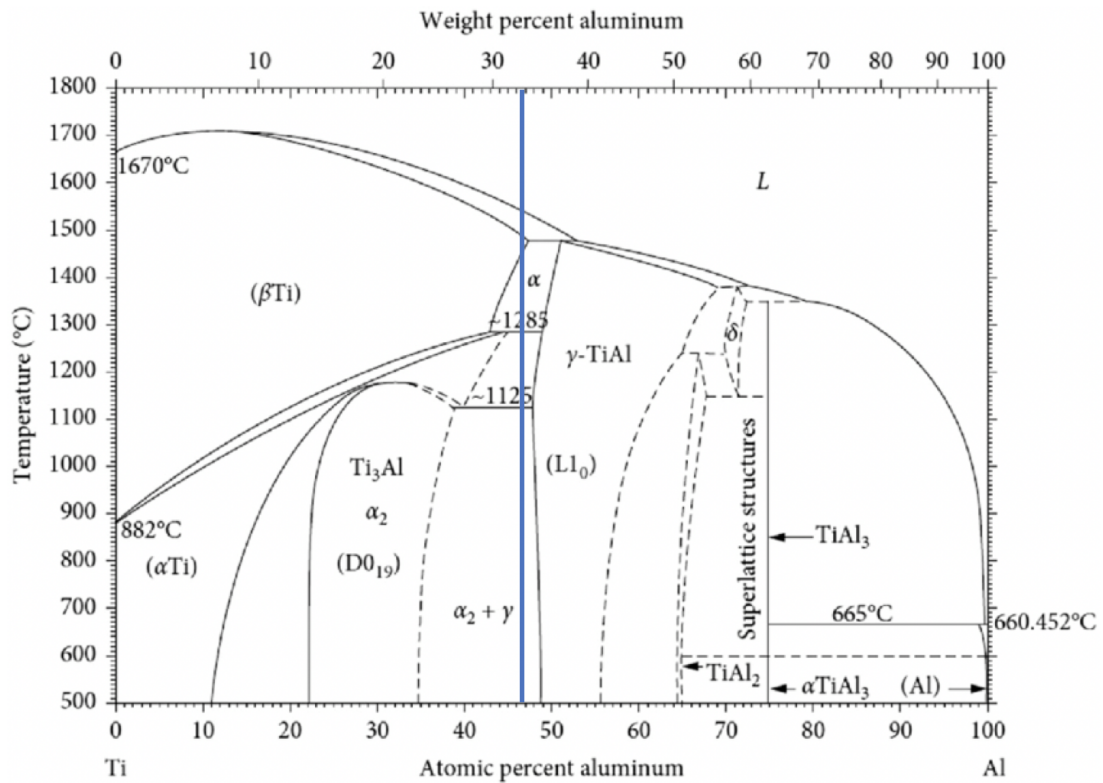


Figure 2.4: Ti-Al binary phase diagram [46]. The vertical blue line corresponds to the composition of the bulk material Ti-46.8Al-1.7Cr-1.8Nb (at.%) used for this research.

superdislocations characterized by  $\mathbf{B}=\langle 101 \rangle$  and  $\mathbf{B}=\langle 112 \rangle$ . Additionally, mechanical twinning occurs along  $\frac{1}{6}\langle 112 \rangle\{111\}$ . Recently, it was established that twinning serves as the dominant deformation mechanism at room temperature, thereby contributing to the reduced ductility observed in TiAl  $\gamma$ -phase [48].

To identify the microstructural parameters and chemical composition of TiAl alloy composed of the two mentioned above phases, 3 types of experiments were performed in TEM:

- Diffraction analysis to determine the crystallographic orientation relationship between the two phases of the material.
- Orientation mapping in TEM (NanoMEGAS ASTAR) to obtain phase and orientation maps over a larger surface than it is possible with diffraction analysis in a given period of time.
- Energy dispersive X-Ray (EDX) spectroscopy to identify the chemical composition of the alloy.



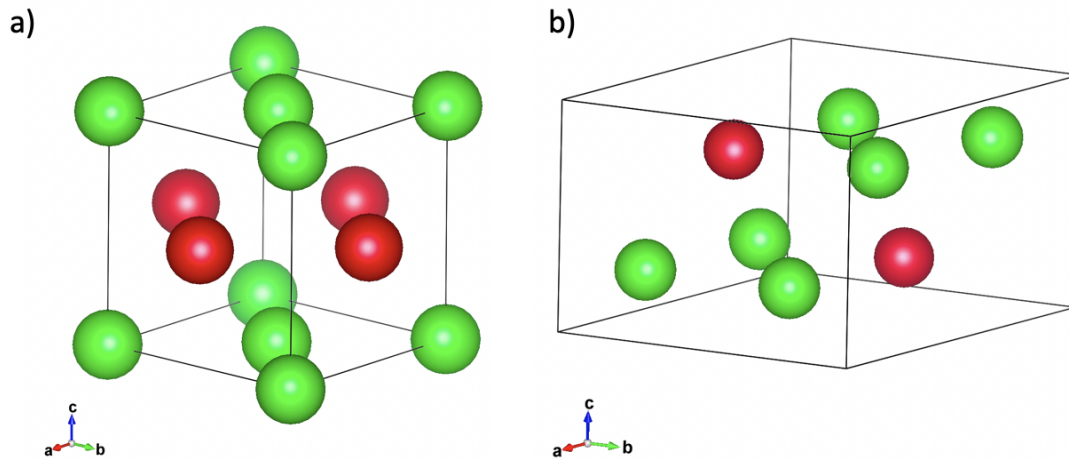


Figure 2.5: Unit cells sketches for two phases of TiAl alloy: (a)  $\gamma$ -phase unit cell with the lattice parameter  $a=0.4\text{nm}$ ,  $b=0.4\text{nm}$ , and  $c=0.405\text{nm}$ , the theoretical ratio for Ti/Al is equal to 1. (b)  $\alpha_2$ -phase unit cell with the lattice parameter  $a=0.577\text{nm}$ ,  $b=0.577\text{nm}$ , and  $c=0.462\text{nm}$ , the theoretical ratio for Ti/Al is equal to 3. Green and red spheres represent Ti and Al atoms respectively.

### 2.3.1 Diffraction analysis

Diffraction analysis was performed on the Thermo Scientific Tecnai Osiris (S)TEM machine at the Interdisciplinary Centre for Electron Microscopy (CIME)-EPFL, this microscope is equipped with high brightness Schottky Field Emission Gun (X-FEG), Super X EDX detector system, and four STEM detectors. Selected Area Electron Diffraction (SAED) patterns were acquired from different grains of the sample with parallel electron illumination in the TEM mode. When diffraction patterns needed to be obtained from small grains, Convergent Beam Electron Diffraction (CBED) was used, a technique that enables very localized crystallographic analysis on the nanometer scale. To identify the orientation of experimentally acquired diffraction patterns they were compared with simulated diffraction patterns from JEMS software [49], which allows to simulate SAED and CBED patterns. Since TiAl alloy has two different phases, two unit cell parameters were used to do the simulation: from  $\gamma$ -phase and the  $\alpha_2$ -phase, as depicted in Fig. 2.5.

After performing the TEM diffraction analysis on the different grains in electropolished and FIB lamella TiAl samples, it was confirmed that there are two phases in the material: tetragonal TiAl ( $\gamma$ -phase) and hexagonal close packing  $\text{Ti}_3\text{Al}$  ( $\alpha_2$ -phase), which is consistent with the phase diagram in Fig. 2.4. It was observed that the large grains correspond to the  $\gamma$ -phase of TiAl, while  $\alpha_2$ -phase corresponds to the small grains with expanded lattice parameter  $c=0.462\text{nm}$ .  $\gamma$ -phase and  $\alpha_2$ -phase have crystallographic orientation relationship of  $(1, -1, 1)\gamma // (0, 0, -2)\alpha_2$  and they show a lamellar structure in this material.

### 2.3.2 Orientation mapping in TEM with NanoMEGAS ASTAR

To study the sample's microstructure on a larger scale one needs to perform the orientation-phase mapping. The fast acquisition of those maps is possible with the NanoMEGAS ASTAR tool, which allows to automatically acquire crystal orientation maps, and phase maps in TEM by collecting precession electron diffraction (PED) patterns and performing cross-correlation comparisons with pre-simulated electron diffraction templates. Experiments were performed on the Thermo Scientific Tecnai Osiris (S)TEM machine at CIME equipped with a NanoMEGAS DigiSCAN unit where beam scanning is done in TEM mode and PED patterns were recorded on a fast CCD Stingray camera.

PED patterns have advantages compared to conventional SAED patterns: they remove the excitation errors due to the curvature of the Ewald sphere and they also reduce dynamic scattering effects (e.g. Kikuchi lines), and the number of diffraction spots intercepted by the Ewald sphere in PED patterns improves significantly, which makes the following indexing of the patterns more reliable and precise [50].

To form the narrow precessed beam the smallest condenser aperture available at the current microscope with size  $10\ \mu\text{m}$  was used to obtain a probe with around 5 nm in diameter, which defines the spatial resolution on the specimen. The FEG electron source of the microscope allowed to preserve the brightness of the beam. The precession angle of the beam was 0.5 degrees. The step size for scanning was set to 10 nm with 300 steps, so the area during one acquisition was composed of  $3 \times 3\ \mu\text{m}$ .

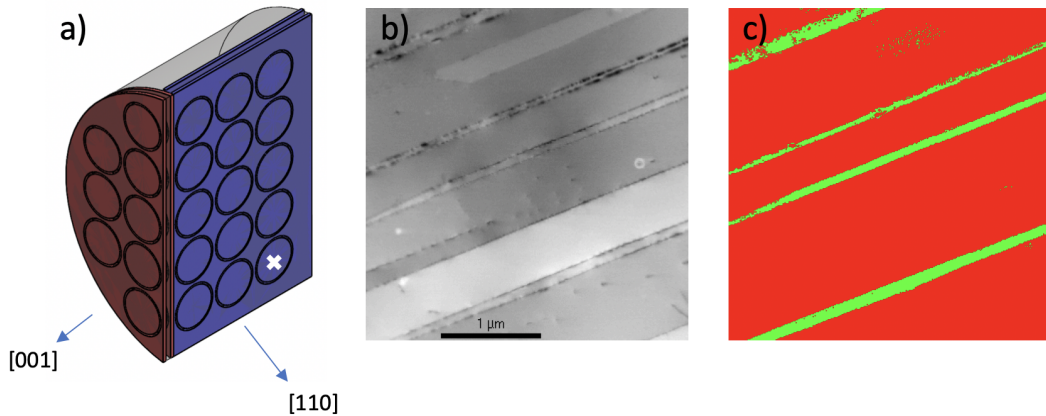


Figure 2.6: Orientation-phase mapping of the electropolished TiAl TEM samples: (a) Bulk sample's scheme with crystallographic axes of  $\gamma$ -phase, (b) Virtual BF image of the region of interest, highlighted by a white cross in (a), (c) Corresponding phase map, where red areas represent  $\gamma$ -TiAl and green areas are  $\alpha_2$ -phase precipitates.

Acquisition and following analysis of the PED patterns from different samples allowed to map the initial semi-cylindrical bulk sample to identify the crystallographic orientations. Fig. 2.6 shows a schematic representation of the initial TiAl bulk sample with crystallographic axes as a

result of ASTAR experiments and an example of the phase map acquired from the bottom-right sample from the rectangular region of the semi-cylinder.

### 2.3.3 Chemical analysis

To obtain a chemical characterization and elemental analysis of the TiAl sample, Energy Dispersive Spectrometry in Scanning TEM (STEM-EDS) measurements were performed on the Thermo Scientific Tecnai Osiris microscope equipped with a Super-X detection system comprised of four SDD EDX detectors.

EDX measurement results also support the distribution of the two phases previously shown in the binary phase diagram, see Fig. 2.7. The average Ti/Al ratio of  $\alpha_2$ -phase is 1.77, which is consistent with previous EDX measurements [51]. However, sometimes, a small deviation appears for the Ti/Al ratio of  $\gamma$ -phase, the average Ti/Al ratio is 1.18. It may be caused by the existence of  $\alpha_2$ -phase precipitates or from the sample preparation. The Nb/Cr ratio in Fig. 2.7 shows that Nb is rich in  $\gamma$ -phase and Cr is rich in  $\alpha_2$ -phase. Since the Cr atom can occupy the Al site in  $\alpha_2$ -phase and the radius of the Cr atom is slightly larger than the Al atom, the unit cell lattice parameter  $c$  is expanded.

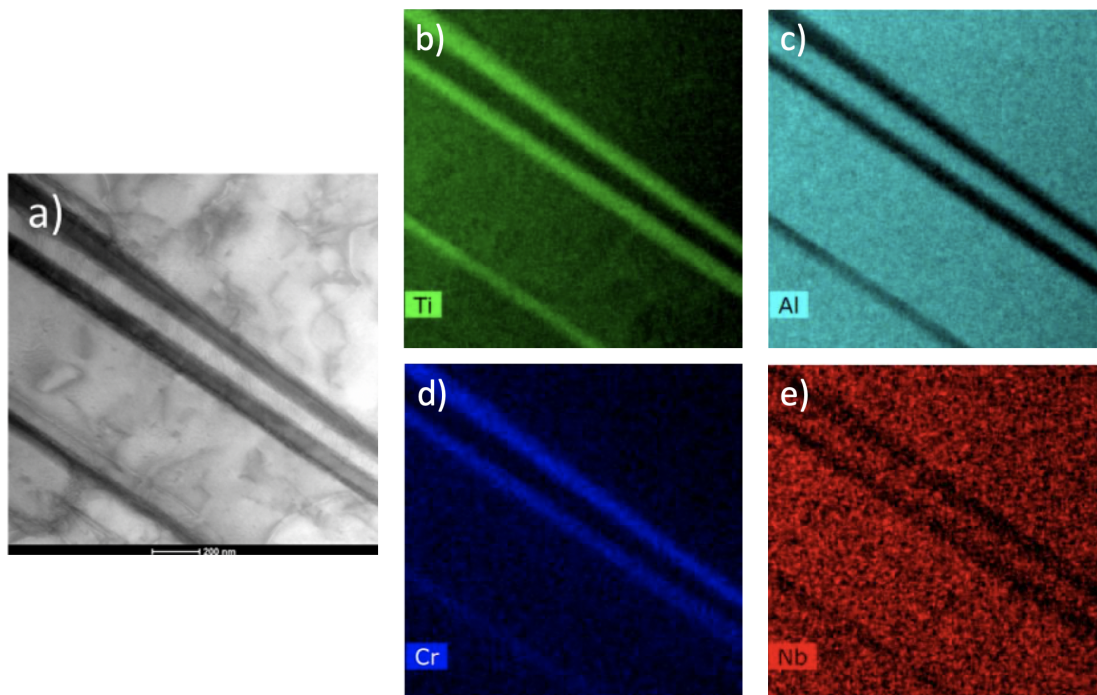


Figure 2.7: EDX analysis results for the FIB sample of the TiAl alloy: (a) BF-STEM image of the region for quantitative analysis, (b) STEM-EDX map of Ti, (c) STEM-EDX map of Al, (d) STEM-EDX map of Cr, (e) STEM-EDX map of Nb.

## 2.4 STEM imaging of dislocations

STEM imaging mode is a widely used electron imaging technique in the field of material science, in particular, for defect analysis. The principle of reciprocity makes it possible to expect the same contrast formation mechanisms, in particular when imaging dislocations.

The main contributions to the contrast of dislocations in TEM and STEM include:

- Diffraction condition (adjusted by tilting the sample with respect to the electron beam direction and allowing to fulfill the Bragg condition, exciting only one  $\mathbf{g}$ -vector, so-called two-beam diffraction condition).
- Imaging mode (allows to choose the intensity from the primary beam, i.e. to form the bright-field image with intensity coming from the direct beam, or dark-field image, where the intensity comes from the diffracted beam).
- Excitation error (choosing the exact Bragg condition or with a small deviation from it).
- The dislocation visibility condition (when the magnitude of the scalar product between the diffraction vector  $\mathbf{g}$  and the Burgers vector  $\mathbf{B}$  is maximum, invisibility condition applies when the scalar product is close to zero).

Despite that, slight deviations still appear in defect imaging in STEM mode compared to TEM imaging, due to the convergence of the electron beam and various detectors with different acceptance angles [52], [53].

The microscope setup for STEM imaging is shown schematically in Fig. 2.8, where a beam with convergence angle  $2\alpha$  passes through the sample forming a convergent beam electron diffraction (CBED) pattern with transmitted and diffracted discs projected into the BF and annular detectors. For the acquisition of a tilt series or stereo images of dislocations, it is important during the tilt of the sample to preserve the same value of the excitation error (along the lines in the transmitted disc) in order to maintain similar contrast in the images. Variation of the Camera length (CL) allows for adjustment of the collection angle of the detectors and projecting particular reflections on the chosen detector.

The advantages of STEM imaging compared to conventional TEM (CTEM) imaging include the absence of bend contours, the possibility to image thicker specimens, and in the case of dislocation imaging - a reduced oscillatory contrast along the dislocation line [54].

The difference between CTEM and STEM images of dislocations in  $\gamma$ -phase TiAl is shown in Fig. 2.9. As one can observe, bright-field (BF) and weak-beam dark-field (WBDF) TEM dislocation images have oscillatory contrast along the dislocation line due to the different depths in the foil at which dislocations are found, as well as the presence of bend contours due to difference in orientation of the foil. On the contrary, the BF STEM image smears out the



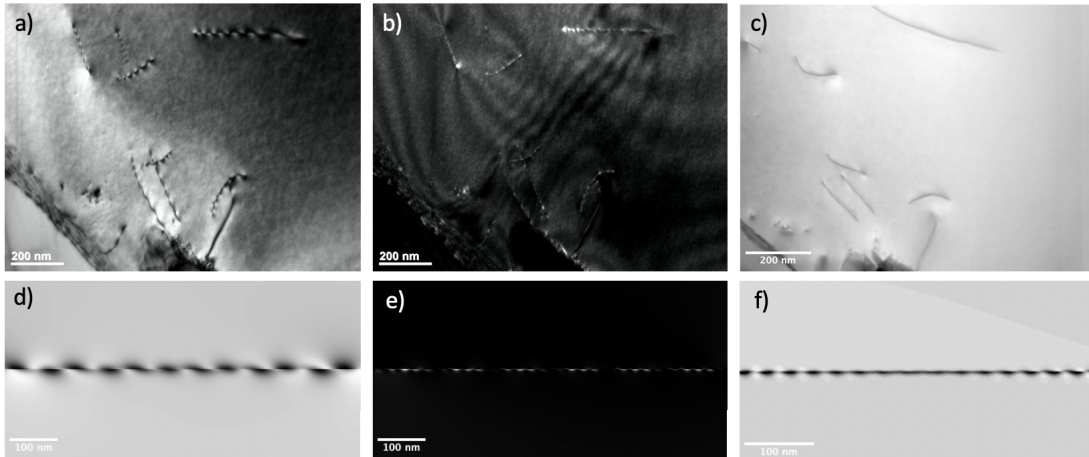


Figure 2.9: Dislocations in  $\gamma$ -phase TiAl alloy experimentally imaged and simulated with CUFOUR software in two-beam diffraction condition  $g=(002)$  with different TEM modes: (a) Bright-field TEM image, (b) Weak-beam dark-field TEM image, (c) Bright-field STEM image, (d) BF-TEM simulated image, (e) Weak-beam dark-field simulated image, (f) BF-STEM simulated image.

### 2.4.1 Optimization of imaging conditions

Due to the many variables in STEM imaging affecting the contrast of the defects and the background of the images, experiments with different imaging and diffraction conditions were performed in order to access the experimental parameters that deliver the optimal image contrast for further post-processing and work the best with deep learning neural networks. STEM images of dislocations were acquired under various detector collection angles, scan pixel sizes, pixel dwell times, and excitation errors. In order to quantify the results and be able to choose optimal values, a special quantification tool was developed in collaboration with the UPHESS laboratory at EPFL. Chapter 5 of the thesis is dedicated to a detailed explanation of the topological quantification technique and analysis of various experimental parameters.

## 2.5 Tomographic reconstruction of dislocations

3D reconstruction of dislocations using the tomography technique is a widespread approach in the field of electron microscopy allowing to obtain the 3D distribution of these linear defects in the sample volume. As mentioned in the introduction of this chapter, performing a tomographic 3D reconstruction requires an investment of a considerable amount of time, the application of 3D reconstruction software, as well as usage of a special tomography holder that allows tilting the sample over a wide range of angles, around  $\pm 80$  degrees. In the case of dislocation 3D imaging, it is also necessary to properly orient the sample in the microscope and follow precisely the same diffraction condition during tilting, to maintain the same value of  $s_g$  and to retain similar contrast in all tilt series.



Due to the advantages of STEM dislocation imaging compared to the conventional TEM imaging, tilt series of dislocations in the TiAl alloy were acquired in the STEM mode on a Thermo Scientific Tecnai Osiris transmission electron microscope at 200 kV. Images were acquired in bright-field (BF) configuration for which a 70  $\mu\text{m}$  condenser aperture was used to form the probe with 12.4 mrad convergence semi-angle and the detector collection semi-angle was set to 18.4 mrad so that the rim of the direct disc (000) covers the BF detector. Tilt-series of BF-STEM images with 1024x1024 pixels resolutions was acquired while the sample was tilted within  $\pm 50$  degree tilt range and imaged every 2 degrees with slightly positive deviation from the  $\mathbf{g}=(002)$  two-beam diffraction condition. The sample was carefully oriented using a Fischione Instruments dual-axis tomography holder (model 2040) so that the deviation parameter  $s_g$  remains constant throughout the tilt range. To ensure the stability of the sample across all tilt angles during experiments, we used an alpha-wobbler with an inclination of  $\pm 10$  degrees. The maximum lateral shift of the sample during tilt was 100 pixels, which corresponds to 300 nm. The relative precision of the sample tilt is  $< 0.1$  degree.

To align the tilt series of dislocations and to obtain the tomographic reconstruction of dislocations Inspect3D software was used, which allows performing 3D reconstruction with Simultaneous Iterative Reconstruction Technique (SIRT), conventionally used in the field of material science. The process was followed by interactive visualization applying Chimera software, whereby by adjustment of the different threshold values one can obtain a representation of 3D tomographic reconstruction.

An example of BF-STEM images from the 45 image stack used for SIRT tomographic reconstruction is depicted in Fig. 2.10 jointly with the different views of the tomogram visualized by the Chimera software. As one can observe, SIRT reconstruction delivers accurate results within the tilting range of the reconstruction, however, side views (e) and (f) demonstrate blurred outline of dislocation lines due to the missing wedge problem and the fact that this technique performs reconstruction in a structure-unaware manner.

The goal of performing tomographic 3D reconstruction and visualization of the dislocations, in this case, was to compare it to the stereo 3D reconstruction by CNNs (which will be introduced in the following chapter of the thesis) since the ground truth is not available (i.e. real distribution of the dislocation in the 3D volume of the sample is not known).

## 2.6 Stereo 3D reconstruction

Stereo 3D reconstruction of the curvilinear and point structures in microscopic images proved to be a promising approach compared to tomography which requires a significant investment of time, while stereo 3D imaging requires the acquisition of only two different views on a sample. Also due to the long electron exposure time in a particular region of the sample, electron tomography has limitations when applied to radiation-sensitive materials.

While tomography is an established and mature technique to visualize the 3D distribution of

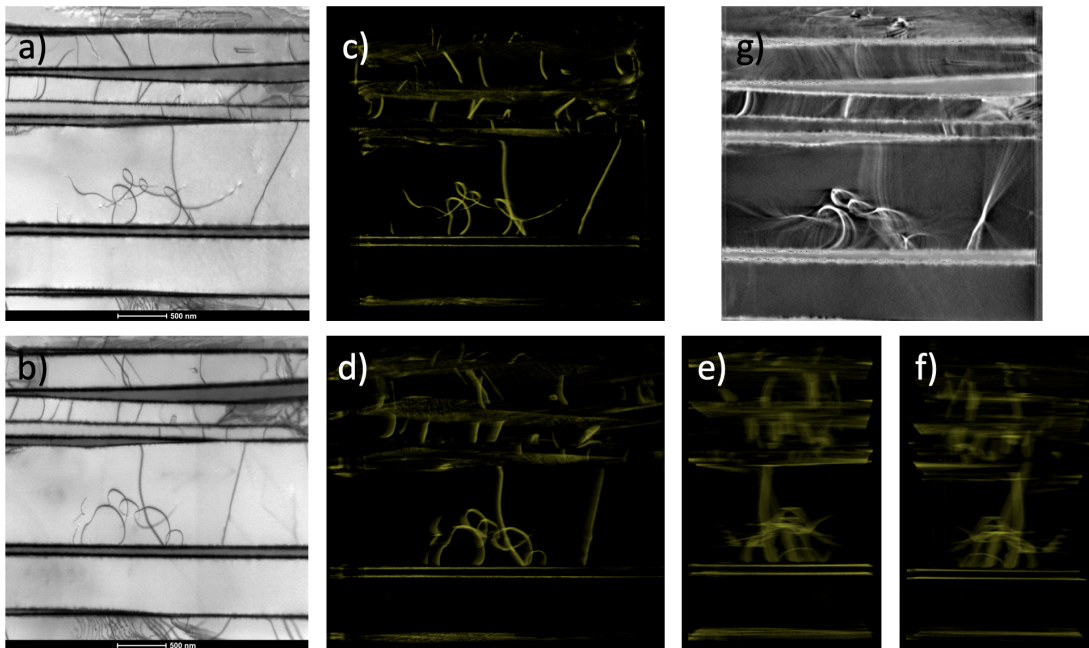


Figure 2.10: Tomographic 3D reconstruction utilizing SIRT and 45 BF-STEM images of dislocations in TiAl alloy: (a), (b) BF-STEM images of dislocations with  $0^\circ$  and  $30^\circ$  of tilt respectively, (c), (d) Tomogram visualization oriented to the same angle as images in their left, (e), (f) Tomogram visualization from the left and the right side views correspondingly, (g) Tomogram slice from the center of the depth volume.

the specific features in the volume of the sample, stereo 3D reconstruction is lacking special dedicated software to perform the 3D reconstruction and to provide visual results. One of the ways to visualize a stereoscopic 3D image of dislocations is to create an anaglyph by using color filters to produce a 3D effect when viewed with corresponding color-coded glasses. Anaglyph images typically use red and cyan color filters to create a stereoscopic effect for the human brain. However, reading an anaglyph image can be complicated for the unprepared viewer. There is also a limit in terms of the stereo-angle for constructing and viewing an anaglyph, which depends on various factors, such as the quality of the images, the resolution of the display, and the individual's visual acuity. Generally, the optimal viewing angle for anaglyph images is between 5 and 10 degrees, which allows for the best depth perception and minimizes the visual strain [56]. Other requirements for an anaglyph creation are that the stereo-pair of images must be acquired at the same magnification and focus, with lateral horizontal shifts of the features not more than 15% of the image width.

For the dislocation images acquired by means of an electron microscope, there is no assessment of the optimal stereo-angle for an anaglyph creation and reading. While it is strongly dependent on the dislocation configuration in the 3D volume and the viewing perspectives, it was still feasible to perform the evaluation of the limiting stereo-angles using the STEM image sequence of dislocations in TiAl alloy acquired for tomographic reconstruction in the previous



section of the thesis. Anaglyphs obtained from aligned STEM images with various stereo-angle can be seen in Fig. 2.11, best viewed with red-cyan glasses. Observation of anaglyphs made with angles greater than 8 degrees of tilt between the images becomes a challenging task for most microscopy users, due to the large values of horizontal shifts between corresponding dislocation points, i.e. stereo-shifts.

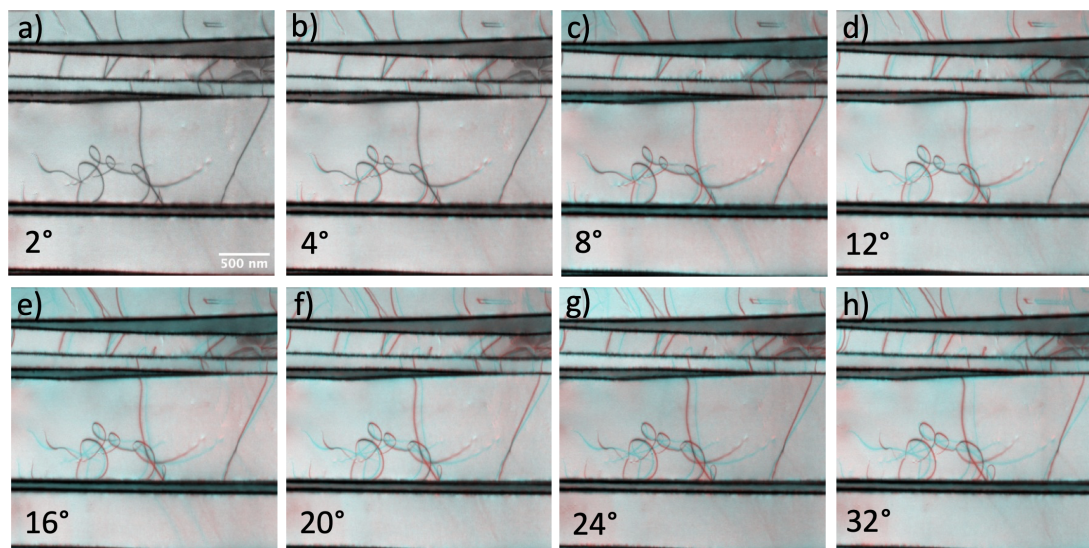


Figure 2.11: Stereographic 3D visualization of dislocations in TiAl alloy utilizing anaglyphs made from aligned stereo-pairs of BF-STEM images acquired under various tilt angles. The value of the stereo-angle of each pair is displayed in the lower-left corner of the corresponding anaglyph. Best viewed in red-cyan glasses.

Other existing techniques for stereo 3D reconstruction and visualization, as discussed in the introduction section, require more human effort and time, including manual or semiautomatic tracing of dislocation lines on both views, then computation of stereo-shifts and triangulation. Current algorithms do not allow the treatment of large amounts of data in a short period of time and are not capable of effectively processing images that contain intricate and complex structural shapes.

## 2.7 Concluding remarks

In this chapter, it was shown that the most appropriate sample preparation technique for TiAl alloy is the electropolishing technique in combination with BIB milling. This method allows obtaining electron transparent regions in the sample with a smooth variation of thickness with an adequate number of dislocation densities for the following 3D reconstruction, and in comparison to the FIB milling technique, does not introduce additional defects to the material.

Microstructural analysis of the TiAl sample was performed, which demonstrated the existence

of the two phases in the material: large grains of tetragonal  $\gamma$ -phase and hexagonal  $\alpha_2$ -phase precipitates. Large grains of the tetragonal phase incorporates numerous dislocations with a variety of outlines which make these regions in the sample an ideal candidate for dislocation studies and 3D imaging.

It was confirmed that STEM is the preferred imaging technique for dislocation structures due to the absence of dynamic effects, which results in effortless post-processing for 3D reconstruction. Since the STEM technique is impacted by a range of parameters that can alter image contrast, experiments with various imaging and diffraction conditions were performed. Using this approach, it was possible to achieve sharp contrast of dislocation lines with reduced image noise and uniform background.

After careful revision of the existing tomographic and stereo 3D reconstruction techniques, it was possible to arrive at the conclusion that rapid approaches for curvilinear and point-like 1D structures needed to be developed. Available methods required manual work and threshold adjustments, and importantly for material science, did not provide visualization in the crystallographic frame of reference.

Stereo 3D reconstruction for transmission electron microscopy is a promising and low-effort approach in terms of image acquisition. Obtaining a distribution of 1D and 2D structures in the volume of a sample could be automatized, due to the fact that for these structures a few projections are sufficient if one uses structure-aware reconstruction techniques. Also, with the help of new methods developed in the field of deep learning and computer vision, it became feasible to establish a fast and reliable fully automatic pipeline for 3D reconstruction, which will be presented in the next chapter.



# 3 Stereo 3D reconstruction of dislocations by deep learning neural networks

In this chapter of the thesis, a novel approach for automatic stereo 3D reconstruction of curvilinear structures from electron microscopy images will be presented. This approach is based on the convolutional neural network (CNN) model trained with STEM dislocation images. The automatic 3D reconstruction pipeline will be discussed with a detailed explanation of each step, as well as the dislocation dataset from three different materials used for training purposes. Various ways to enlarge the training dataset will be presented, due to the limited number of STEM images that is possible to acquire and label in a given period of time. Evaluation of the network's precision will be addressed using the tomogram presented in the previous chapter.

This work was done in collaboration with the Computer Vision Laboratory at EPFL in the framework of the SCEM project<sup>I</sup>.

## 3.1 Introduction

As mentioned above, progress in the field of computer vision and the development of deep learning algorithms found many applications in electron microscopy imaging and post-processing.

Tomographic 3D reconstruction of point-like or curvilinear structures using WBP or SIRT techniques requires a considerable amount of imaging and post-processing time. However, the application of modern approaches could simplify the process of 3D reconstruction with fewer images being acquired if structure-aware deep learning reconstruction algorithms are used.

Disadvantages of the tomography technique and of the currently available algorithms for 3D

---

<sup>I</sup>Parts of this chapter were adapted from the published article of [O Altingövde, A Mishchuk, G Ganeeva, E Oveisi, C Hebert, P Fua, '3D reconstruction of curvilinear structures with stereo matching deep convolutional neural networks', *Ultramicroscopy*, 234 (2022), doi: 10.1016/j.ultramic.2021.113460]. Authors contributions: GG acquired, processed, and labeled TEM data, and wrote the chapter, OA and AM developed neural networks' architecture, CH and PF supervised the project.

reconstruction defined the aim of this work, in particular, the development of an automatic approach to obtain a 3D reconstruction of the dislocations just from two different views on the sample, i.e. to perform stereo 3D reconstruction utilizing deep-learning neural networks.

The developed stereo 3D reconstruction pipeline contains four main steps:

- Image rectification, or alignment, so that a tilt axis is vertical on both views.
- Simultaneous detection of the dislocation lines on the stereo-pair.
- Stereo matching.
- Triangulation to transform the 2D contours into 3D dislocation models.

Stereo reconstruction processing steps are depicted in Fig.3.1

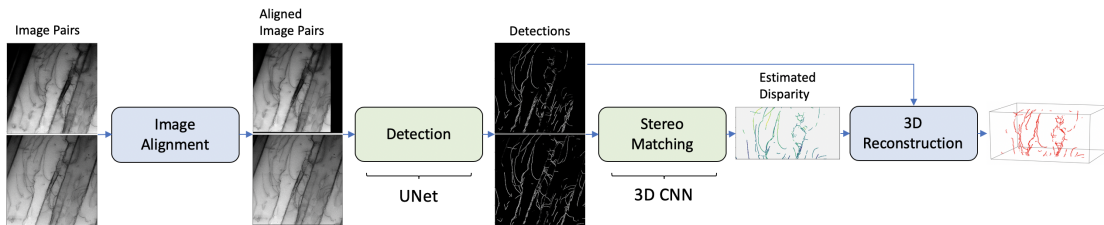


Figure 3.1: Stereo reconstruction processing steps. In the first step, images are aligned such that the tilt axis is vertical and at the image center. Dislocation segments are detected using UNet [57] in the second stage. Later, features of UNet are provided to a 3D CNN in order to compute horizontal disparity between corresponding dislocation segments. At the final stage, the depth value for every detected dislocation pixel is computed using disparity estimations. Green blocks in the figure represent the stages that are learned from annotated training data.

### 3.2 Image rectification

The requirement to perform the automatic stereo 3D reconstruction by deep learning neural networks are similar to the ones with classical tomography techniques: images need to be aligned so the tilt axis is vertical and at the image center, in this case, corresponding points on both images are along the so-called epipolar line. If the two images are aligned, then each pixel’s epipolar line is horizontal and at the same vertical position as that pixel. However, in reality, images acquired while the sample is tilted in the microscope are never perfectly aligned. Although the viewing angle can be controlled up to a degree, the region of interest is not necessarily located around the rotation axis and need to be centered manually during image acquisition. A manual search of the region causes translational misalignment between consecutive acquired images. Moreover, it is not always possible to maintain an exact vertical tilt-axis due to a non-perfectly compensated image rotation which may yield deviations up

to  $2^\circ$  from the vertical axis. Thus, we write the relationship between image coordinates of corresponding points  $\langle p, q \rangle$  in the original unaligned images as

$$\begin{aligned}(x_p, y_p) &= (x_q + d_q \cos \theta - t_x, y_q + d_q \sin \theta - t_y), \\ (\Delta x_{pq}, \Delta y_{pq}) &= (d_q \cos \theta - t_x, d_q \sin \theta - t_y),\end{aligned}\quad (3.1)$$

where  $\theta$  is the angle the tilt-axis makes with the vertical axis on the image plane,  $d_q$  is the disparity of point  $q$ ,  $(t_x, t_y)$  are translational shifts that occurred during acquisition on axes  $x$  and  $y$  of image plane respectively and  $(\Delta x_{pq}, \Delta y_{pq})$  are total displacements on image plane between correspondences prior to alignment. Hence the image transformation that corrects this misalignment is

$$\begin{aligned}T &= [I \mid t] \\ (\hat{x}_q, \hat{y}_q)^T &= T_{[2 \times 3]}(x_q, y_q, 1)^T\end{aligned}\quad (3.2)$$

where  $I$  is the  $2 \times 2$  identity matrix and  $T$  is the  $2 \times 3$  transformation matrix that translates point coordinates expressed in projective coordinates. The keypoints are automatically detected and matched using the Scale Invariant Feature Transform (SIFT) [58] to construct sparse correspondences between left and right images. These points are used to estimate the transformation  $T$  by iteratively solving a linear system of equations. At each iteration, outliers are eliminated using random sample consensus (RANSAC) [59]. After applying  $T$  to the right image, the total displacement between correspondences,  $(\Delta x_{pq}, \Delta y_{pq})$  becomes  $(d_q \cos \theta, d_q \sin \theta)$  and  $\theta$  can be computed as

$$\theta = \arctan\left(\frac{\Delta y_{pq}}{\Delta x_{pq}}\right).\quad (3.3)$$

Finally, the images are aligned by applying the rotation matrix

$$R = \begin{pmatrix} \cos \theta & -\sin \theta \\ \sin \theta & \cos \theta \end{pmatrix}\quad (3.4)$$

to the transformed right image. Once this is done, the epipolar lines are parallel to the horizontal axis of the images, which is a prerequisite for inputs to our deep network as discussed above.

### 3.3 Dislocation detection and matching

In this section, it is assumed that both images are aligned so for a point,  $p = (x, y)$  in the first image, the corresponding point  $q$  is at location  $(x + d, y)$  in the second image, where  $d$  is the *disparity* and proportional to the distance to the image plane. Disparity  $d$  corresponds to the difference between the horizontal coordinates of the same object in two different images.

To detect the dislocations in the 2D images and compute disparities for each one of their points, a deep network was used depicted by Fig.3.2. Its first step consists of a 2D *contour detection network C* in a Siamese configuration [60]. A Siamese network configuration is a type of neural network architecture where two or more identical subnetworks share the same weights and are trained to perform the same task on different input data. In the context of stereo vision, Siamese networks are used to capture the similarity or dissimilarity between corresponding image patches in the left and right images at different disparities. The Siamese configuration encourages feature sharing and reduces the number of trainable parameters compared to independently trained subnetworks. The two subnetworks in the Siamese network take the left and right images as input, respectively, and share the same convolutional layers to extract features from the images. The features maps produced by *C* for both views are combined into the *feature volume*, which is then concatenated and processed through additional layers of a 3D CNN to compute the matching *cost volume*.

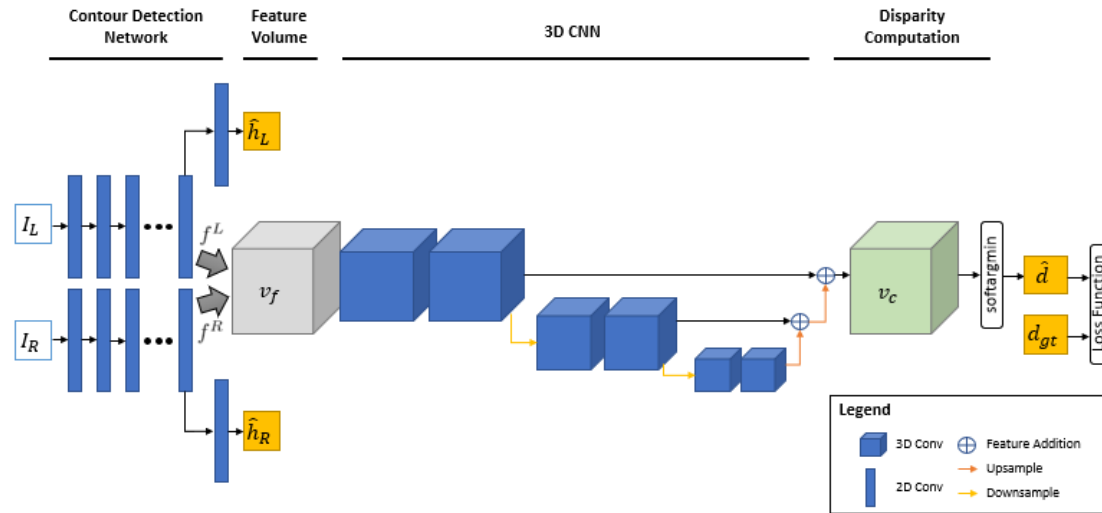


Figure 3.2: Stereo Contour Detection and Matching Network architecture. Layers with learnable parameters are shown in blue. Feature volume,  $V_f$ , and cost volume,  $V_c$ , are depicted as gray and green 3D volumes respectively

A description of each building block of architecture in more detail can be found below.

### 3.3.1 Pre-trained contour detection network

*Contour detection network C* extracts contour-specific features. The lateral resolution of *C* can achieve a sub-pixel level, enabling it to capture fine details and boundaries in images. The feature maps are denoted by  $f^L$  and  $f^R$  and contour detections by  $\hat{h}^L$  and  $\hat{h}^R$  for the left and right images,  $I_L$  and  $I_R$ , respectively. *C* is trained with binary cross-entropy loss. In Fig.3.3, an example of detection output by *C* is shown.

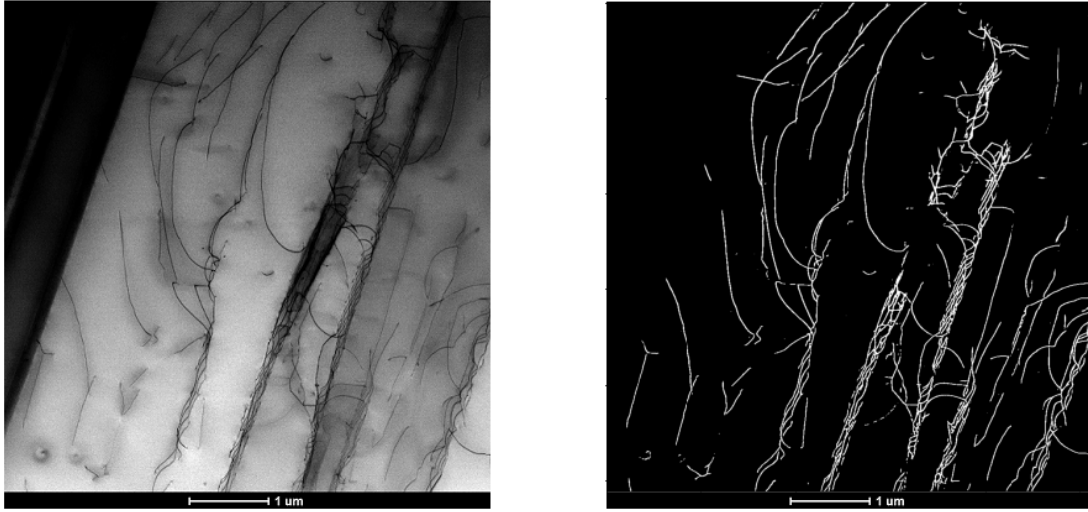


Figure 3.3: Representative BF-STEM image of dislocations in a TiAl alloy thin foil in two-beam diffraction condition with  $\mathbf{g}=(002)$  (a) and corresponding detected dislocations (b). The detection network manages to detect dislocations having complex shapes even in noisy images while still being able to reject unrelated dark sections of the image.

### 3.3.2 Feature Volume

Feature volume is a 3D representation that encodes the extracted features of two images at multiple scales or levels of abstraction. In computer vision, feature volumes are often used as input to neural networks for various tasks such as object detection, segmentation, and tracking. The advantage of using feature volumes over individual feature maps or flat feature vectors is that they capture information at multiple scales and levels of abstraction. This can improve the representation of complex visual patterns and make the feature representation more robust to variations in the input data.

As in many existing architectures [61], a feature volume  $V_f$  shown in Fig.3.4, is constructed by replicating the left and right feature maps once for every possible disparity value, and concatenating them into a tensor of size  $2 \cdot \text{feature size} \times \text{height} \times \text{width} \times \text{disparity range}$ , so that  $V_f(\cdot, u, v, d)$  is a concatenation of features  $f^L(\cdot, u, v)$  and  $f^R(\cdot, u + d, v)$ , where  $u$  and  $v$  are coordinates of the left image and  $d$  is disparity. This enables the evaluation of match hypotheses  $(u, v, d)$  by means of a 3D CNN as follows.

### 3.3.3 3D CNN for Matching Cost Estimation

A 3D CNN is used to compute a cost volume  $V_c$ , shown in green in Fig.3.2, from the feature volume  $V_f$ . In deep learning-based stereo vision, cost volume is a common representation that is used to capture the matching cost between the left and right images at different disparities.  $V_c$  is of size  $\text{height} \times \text{width} \times \text{disparity range}$  and an entry  $V_c(u, v, d)$  encodes the cost of matching a feature  $f^L$  at position  $u, v$  in the left feature map, to a feature  $f^R(u + d, v)$



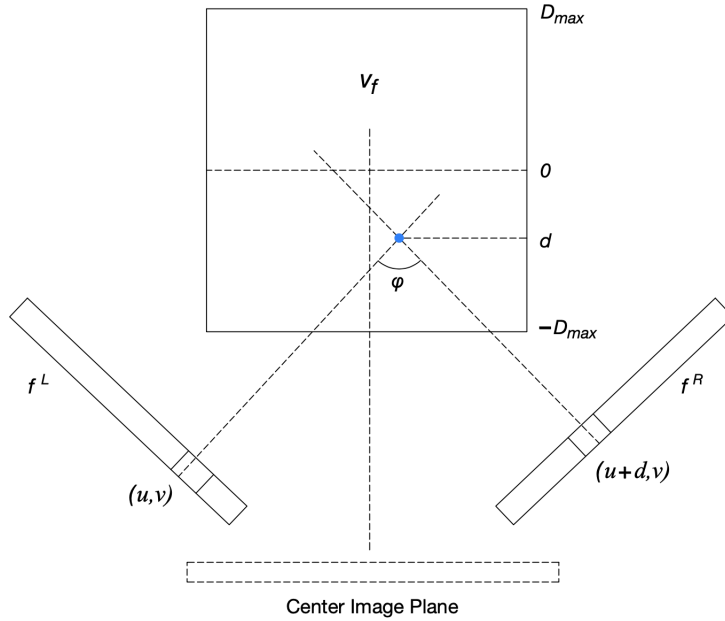


Figure 3.4: Feature volume construction is shown from the top view. For each pixel in the left image, the features of this pixel and candidate pixels for a match in the right image are back-projected to 3D and concatenated to form feature volume. For a specific pixel at location  $(u, v)$  in the left image and a candidate pixel at location  $(u + d, v)$ , the back-projected point in feature volume is depicted as a blue circle in the figure. The value  $d$  for the given pixel is the disparity level that defines the depth of the pixel with respect to the center image plane.

of the right feature map. 3D CNN consists of multiple stacked hourglass modules composed of 3D  $3 \times 3 \times 3$  convolution layers, shown in blue volumes in the center of Fig.3.2.

### 3.3.4 Disparity Computation

As mentioned before, the disparity is a key depth cue that is used to compute the 3D structure of a scene from stereo images. Disparity estimation is a challenging problem in stereo vision, and 3D CNNs have been shown to be effective in learning complex image features and estimating accurate disparities. To compute the disparity volume 3D CNN was utilized, which encodes the estimated disparity for each voxel in the input images. The output of the CNN is a disparity volume, where each voxel represents the estimated disparity between the corresponding pixels in the left and right images. The disparity map can be computed by taking the *argmin* or *argmax* of the disparity volume along the disparity dimension. Then the disparity map is used to compute the 3D structure of the scene by triangulating the corresponding points in the left and right images.

The optimum disparity for a pixel at location  $(u, v)$  is the one with the lowest matching cost which is encoded in cost volume,  $V_c$ . Therefore, a disparity estimate is an index of the minimum element along the disparity axis of  $V_c$  for each pixel, which could be found using the

*argmin* operation. However, *argmin* is not differentiable and can therefore not be used as part of neural network architecture. Instead, the differentiable *soft-argmin* was used defined as

$$\hat{d}_{uv} = \sum_{d=0}^{d_{max}} d \cdot \sigma(-V_c(u, v, d)) \quad (3.5)$$

where  $\sigma(\cdot)$  is the *softmax* operation,  $d$  is disparity level and  $V_c(u, v, d)$  is matching cost of pixel at location  $(u, v)$  for disparity  $d$  to be able to train neural network.

### 3.4 Loss Function

The loss function is a mathematical function that compares the difference between the predicted output of a neural network model and the true output, i.e. ground-truth. It is commonly used to measure how well the neural network models the training data and to optimize the model's parameters during training by minimizing the error between the predicted output and the ground-truth.

The stereo-matching network is trained with a loss function that is a weighted sum of three loss terms:

$$L = \gamma_{disp}L_{disp} + \gamma_{var}L_{var} + \gamma_{warp}L_{warp}, \quad (3.6)$$

where  $L_{disp}$ ,  $L_{var}$ , and  $L_{warp}$  represent a disparity, variance, and warp loss, which are described in more detail below.

#### 3.4.1 Disparity Loss

When the ground-truth disparity,  $d_{gt}$ , is available, the inconsistencies are penalized in the prediction  $\hat{d}$  by means of the smooth L1 loss

$$L_{disp} = \frac{1}{|\mathcal{A}|} \sum_{a \in \mathcal{A}} \begin{cases} 0.5 \cdot e_d^2, & \text{if } e_d < 1 \\ e_d - 0.5, & \text{otherwise} \end{cases}, \quad (3.7)$$

where  $e_d = \hat{d} - d_{gt}$  and  $|\mathcal{A}|$  is the set of pixels belonging to dislocations with available disparity annotations.

#### 3.4.2 Variance Loss

While minimizing  $L_{disp}$  encourages the network to find the correct disparity value, it is also important that it delivers a low variance around that ground-truth value so that the estimates

are accurate. Therefore, variance loss is defined as

$$L_{var} = \frac{1}{|\mathcal{A}|} \sum_{a \in \mathcal{A}} \hat{v}, \quad (3.8)$$

where  $\hat{v}_{uv} = \sum_{d=0}^{d_{max}} (d - d_{gt})^2 \cdot \sigma(-V_c(u, v, d))$ .

The disparity estimator defined in Eq. 3.5 may be seen as the probability-average of possible disparity levels by taking  $\sigma(-V_c(u, v, d))$  term as the probability of disparity level  $d$ . In this case,  $\hat{v}$  becomes the expectation of the squared deviations of disparity around the disparity ground truth. Minimizing  $L_{var}$ , therefore, minimizes the variance of the estimate  $\hat{v}$  around  $d_{gt}$ .

### 3.4.3 Warp Loss

Given the detection map of curvilinear structures in the right image,  $\hat{h}^R$  and the disparity,  $\hat{d}$ , the left detection map,  $\hat{h}^L$  can be reconstructed by shifting pixels with their corresponding disparity values. This operation is called *warping* and it is incorporated in warp loss

$$L_{warp} = L_{bce}(\text{warp}(\hat{h}^R, \hat{d}), h_{gt}^L). \quad (3.9)$$

where  $L_{bce}$  is the binary cross entropy loss. Minimizing  $L_{warp}$  enforces consistency between  $\hat{d}$ ,  $\hat{h}^R$  and  $\hat{h}^L$ .

The overall performance of 3D CNN depends on its capability to localize the minimum cost disparity level in  $V_c$  for each pixel. In other words, it is required to have low variance probability distributions over estimated disparity values to confidently make predictions. In this sense, complementing disparity loss with variance and warp loss terms allows further constraining of network training to have cost estimations not only centered at the ground-truth level but also have lower variances around it. This is especially important when training data is not abundant and cumbersome to annotate which is the case for electron microscopy imaging. In section 3.8.3, an ablation study on components of the loss function is presented to show strong evidence in favor of using complemented loss function over naive disparity loss.

## 3.5 Disparity Refinement

Disparity values are computed from the estimated cost volume using a *soft-argmin* operation as shown in Eq.3.5. In practice, this yields disparities that are within one or two pixels of what they should be. To improve accuracy, a standard technique is used to refine them [62], [63]. It is used to warp the dislocations found in the left image into estimates in the right image, which are then matched to the closest dislocation actually found in the right image to refine the disparity value. Warped dislocations are matched pixel-wise to the closest candidate within

a 3-pixel distance, which delivers the pixel accuracy required for accurate reconstruction. Dislocation pixels without any suitable candidate in this range are marked as erroneous and removed from the final 3D reconstruction.

In section 3.8.3, reconstructions obtained with and without this refinement stage are compared, and it was shown that, on average, it improves precision.

### 3.6 3D Reconstruction

Having disparity values computed, the 3D shapes of curvilinear structures can be reconstructed by applying triangulation with given viewing angles and the orthographic camera assumption.

In the stereo setup of verged orthographic cameras which is shown in Fig.3.4, the depth axis is defined the same as the disparity axis which is parallel to the surface normal of the imaginary center image. Given this definition of depth, its relation to the disparity  $d$  is

$$\text{depth} = \frac{d}{2\sin(\frac{\phi}{2})}, \quad (3.10)$$

where  $\phi$  is the angle between two views. The term  $\sin(\frac{\phi}{2})$  in Eq. 3.10 acts as a scaling factor between depth and disparity. In Fig. 3.5, a 3D reconstruction of dislocations from STEM images with  $4^\circ$  of stereo-angle is shown.

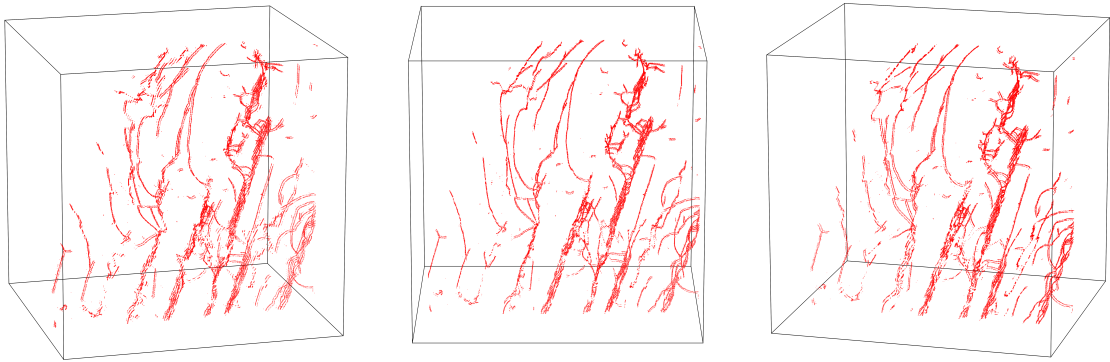


Figure 3.5: 3D Reconstruction of dislocation networks in TiAl alloy shown in Fig.3.3

### 3.7 Datasets and networks' training procedure

For deep learning neural network training and validation of the 3D reconstruction experiments, three stereo dislocation datasets were created each composed of stereo-pairs taken from image sequences of three different materials, representing large diversity of dislocation shapes and contrasts. Bright-field STEM images of dislocations were acquired from TiAl alloy, GaN lamella sample, and high-entropy (Cantor) alloy.

The dislocation dataset consists of 90 labeled stereo-pairs grayscale images split into the train, validation, and two test subsets. Segmentation masks and disparity maps were manually labeled for the task.

All images were resized to 512x512 and normalized to (0, 1). In order to increase the size and diversity of a training dataset, a variety of transformations were applied to the original images. The purpose of this operation, so-called 2D image augmentation, is to improve the robustness of the neural network model by exposing it to a wider range of training examples. 2D image augmentations that were used include random scaling, rotation, and brightness with parameters (0.7, 1.2), (-60, 60), and (0.8, 1.2) respectively. All models are optimized using the Adam algorithm [64] with beta parameters=(0.9, 0.999) and learning rates 0.001 and 0.0001 for detection and stereo matching networks respectively. The training was performed on Tesla V100. The PyTorch neural network framework was used for this implementation.

Occasionally, grain boundaries were observed on the STEM images of the training dataset. They were manually labeled together with dislocation lines, however, as another class of objects, so CNNs learned to ignore them when performing segmentation and 3D reconstruction.

### 3.8 Evaluation of 3D reconstruction's precision

When dealing with dislocations in real-world samples, reliable ground-truth is not available, because even human annotators experience difficulty reconstructing precise 3D curvilinear structures. Therefore, two different qualitative ways were proposed to evaluate the results and demonstrate their accuracy. Also, an ablation study is presented for different stereo setups with varying tilt angles and loss functions to quantitatively show their effect on the overall reconstruction performance.

#### 3.8.1 Re-Projection Errors

Once the 3D dislocations have been reconstructed, they can be back-projected into views that were *not* used to perform the reconstruction. When these projections superpose well with the actual dislocations, it is evidence that the 3D reconstructions were correct. In Fig. 3.6, it is shown for the case where stereo-pairs have  $8^\circ$  between them.

#### 3.8.2 Comparison to Tomography

To further evaluate the accuracy of the 3D reconstruction qualitative comparison of reconstructed 3D dislocations from the tomography baseline method and our neural network reconstruction has been done, as depicted in Fig. 3.7. In comparison with the tomography method, which uses a sequence of 45 images covering the angular range ( $-48^\circ$ ,  $50^\circ$ ), only one stereo-pair has been used with  $2^\circ$  difference between the views.

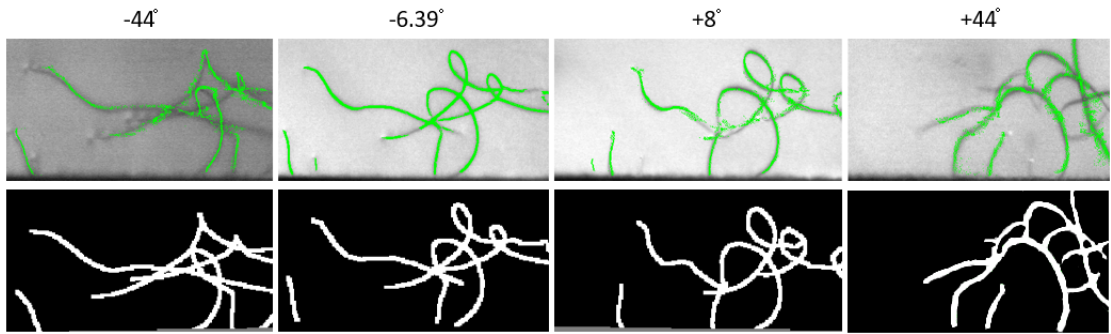


Figure 3.6: Re-projections to other views. Estimated 3D dislocations in the TiAl sample that are reconstructed using a stereo-pair with  $8^\circ$  separation are re-projected to views with  $-44^\circ$ ,  $-6.39^\circ$ ,  $+8^\circ$ , and  $+44^\circ$  tilt angles. In the top row of images, four views are shown with green marks being 3D dislocation points re-projected onto raw images. In the bottom row, the dislocation ground-truths for these views are shown. For all presented views, it can be seen that re-projections of the estimated 3D structure are consistent with raw images and human-annotated dislocations ground truth.

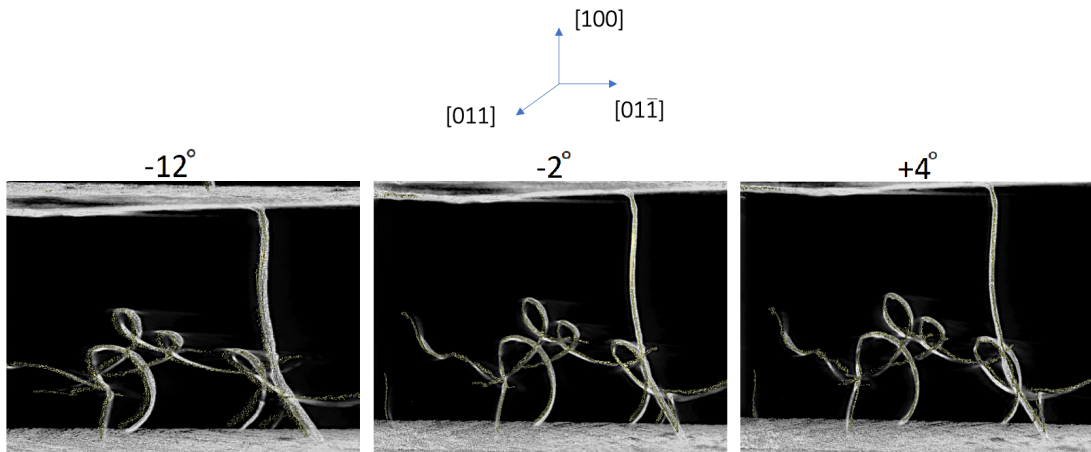


Figure 3.7: Comparison of reconstruction results of stereo approach and tomography. TiAl sample region previously shown in Fig.3.6 is reconstructed by tomography (shown in white) utilizing full image sequence with 45 images covering the angular range  $(-48^\circ, 50^\circ)$  and by stereo CNN method with stereo images having  $2^\circ$  in between (shown in yellow).

Established tomography techniques are mainly brute-force multi-view reconstruction algorithms and rely on geometric constraints to reconstruct 3D shapes. On the other hand, the stereo approach incorporates visual similarities of dislocation segments to lower the ambiguities that may occur when a sufficient number of images for reliable reconstruction is not available or cumbersome to acquire.

To this end, in order to evaluate our method, the stereo approach was compared to two commonly used tomography techniques, Weighted Back Projection (WBP) and SIRT for the

varying numbers of images given as input. In Fig.3.8, it is shown that the stereo reconstruction network outperforms both tomography techniques in low data margin i.e. when only a few images are available. To our knowledge, stereo method is the only fully-automated stereo reconstruction method for curvilinear structures.

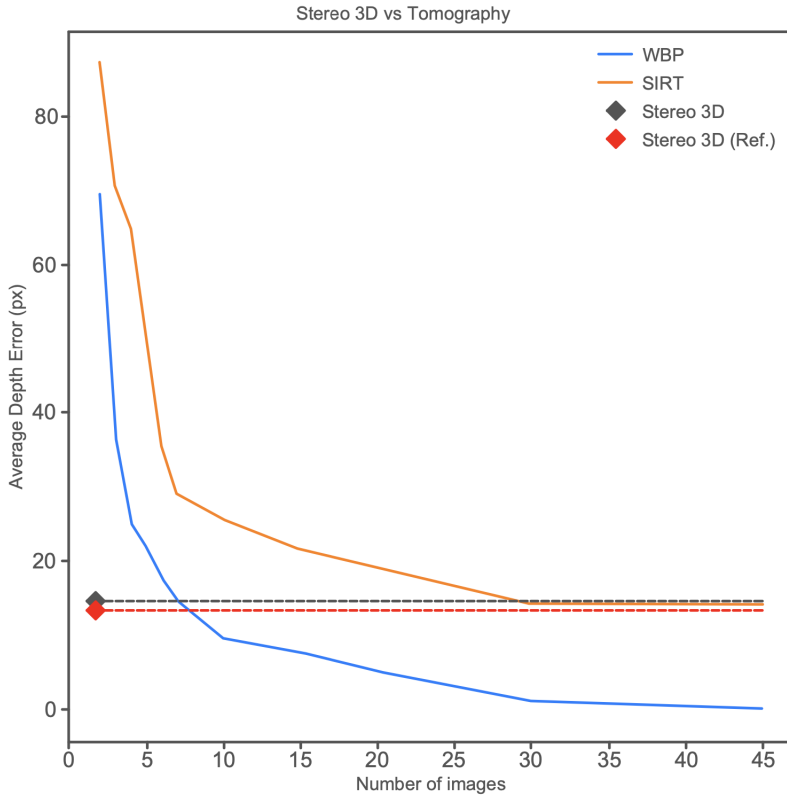


Figure 3.8: Two 3D tomography reconstruction techniques across an increasing number of images given as input compared to the stereo method using two images as input. Images are sampled regularly for each case of tomographic reconstruction from the sequence with 45 images spanning angular range  $(-48^\circ, 50^\circ)$ .

**3.8.3 3D CNN’s precision evaluation**

Human-generated annotations are used as ground-truth in order to compute depth and disparity errors of different configurations. End-Point-Error (EPE) was utilized - the average Euclidean distance between estimated and ground-truth points and the percentage of curvilinear pixels with disparity errors greater than 1, 3, and 5 pixels.

To investigate the effect of stereo setup on reconstruction accuracy, stereo pairs that have 2, 4, 6, 8, 10, and 12 degrees between images are used in the reconstruction process, and corresponding reconstruction errors are shown in Table 3.1. Reconstruction with small angles results in high-depth errors due to heavy discretization although they have a low matching error in pair. On the other hand, when the angle between images is large, the matching task

	2°	4°	6°	8°	10°	12°
Raw 3D	18.3	21.5	15.0	14.6	22.2	28.4
Refined 3D	18.0	20.1	14.7	<b>13.2</b>	21.8	29.9

Table 3.1: Depth estimation errors (in pixels) for stereo setups with different angle separations. For all experiments, the network is trained using the loss function that combines all three loss terms. Results presented without the refinement stage of section 3.5 and with it.

becomes harder and its error starts dominating the total depth error. The reconstruction with STEM images having 8° of stereo-angle demonstrated the most efficient error values. Moreover, an increase in the measured depth error was observed when the angular separation between images increased from 2° to 4°. It is attributed to heavily discretized depth values in reconstructions with extremely narrow angles as 2°. In this regime, depth is encoded into a narrow pixel range on images which renders the matching task effortless since large depth changes are mapped to small horizontal shifts. After passing this regime, an error increase in disparity estimation can be compensated by performance gains resulting from geometry.

The stereo-matching network was trained using different combinations of the loss terms introduced in the section 3.4 to tease out their respective contributions. Table 3.2 shows EPE and percentage of dislocations pixels with errors higher than 1, 3, and 5 pixels for different loss term combinations. It may be seen that a network trained with unsupervised warp loss alone performs poorly on the localization of matching points. While the network may be successfully trained with supervised disparity loss, its accuracy increases notably when combined with novel variance loss introduced in this work. The best results were obtained when all three loss components were combined.

### 3.9 Additional network training with GAN-SPADE

In the domain of Computer Vision in order to train deep learning convolutional neural networks large labeled datasets are conventionally used, which contain typically thousands of images. In the field of TEM acquiring such large datasets and then labeling the images is a cumbersome task, especially in our approach where stereo-pairs should be created by tilting the specimen and labeling of images is done pair-wise. This task could be optimized by creating synthetic training dislocation dataset, however, available dislocation contrast simulation software at the moment allows only obtaining synthetic images of straight dislocations. Synthetic images of dislocations for successful training of the deep learning networks should reveal more complicated shapes and structures corresponding to the real electron microscopy data. Enlargement of the training dataset became possible by utilizing pre-trained GAN-SPADE (Generative Adversarial Network with Spatially-Adaptive Dropout Encoding) [65].



Loss function	1px %	3px %	5px %	EPE px
GaN				
<b>Disp+Warp+Var</b>	<b>40.1</b>	<b>8.3</b>	<b>3.5</b>	<b>1.112</b>
<b>Disp+Var</b>	40.3	8.5	<b>3.5</b>	1.120
Disp+Warp	41	8.6	3.8	1.238
Disp	52.1	9.4	4.4	1.852
Warp	81.6	55.3	30.2	5.034
TiAl				
<b>Disp+Warp+Var</b>	41	<b>9.6</b>	<b>4.1</b>	<b>1.411</b>
Disp+Var	<b>40.7</b>	9.7	4.2	1.418
Disp+Warp	41.6	9.7	4.2	1.415
Disp	54.9	14.2	5.8	1.755
Warp	84.8	57.9	38.3	5.879
Cantor Alloy				
<b>Disp+Warp+Var</b>	<b>38.2</b>	<b>8.0</b>	<b>3.1</b>	<b>0.982</b>
Disp+Var	40.5	8.4	3.3	1.101
Disp+Warp	41.3	8.7	3.6	1.322
Disp	49.8	9.0	4.3	1.523
Warp	80.4	52.4	28.5	5.011

Table 3.2: Comparison of disparity estimation with different combinations of loss terms. Results are presented for three subsets of test data. Stereo pairs with 8° angular range are used for the experiments.

### 3.9.1 GAN-SPADE network's principle

GAN-SPADE is a generative neural network that is used for image synthesis tasks, which architecture consists of two main components: a generator network and a discriminator network. GAN-SPADE learns statistics from the training dataset and generates new images with the same statistics that look authentic and realistic to the human.

The generator network takes as input a semantic layout, which specifies the spatial arrangement of objects in an image, then a series of network layers transforms an input and produces a realistic-looking image. Each layer in the generator network takes the feature map from the previous layer as input and applies a set of convolutional and upsampling operations to generate a higher-resolution feature map.

The discriminator network tries to distinguish between real and synthetic images. It takes as input an image and produces a scalar value indicating whether the image is real or not. The discriminator network consists of a series of convolutional layers that progressively downsample the input image to produce a feature map, which is then used to make a final decision about the authenticity of the image.

During training, the generator network is trained to produce images that mislead the discriminator network into thinking they are real. The discriminator network is trained to correctly identify which images are real and which are synthetically generated. This adversarial training process helps to improve the quality of the generated images.

One of the key innovations of GAN-SPADE is the use of spatially-adaptive normalization. Previous methods directly input the semantic layout to the deep network, but this operation removes the semantic information. The GAN-SPADE method utilizes the input semantic layout while performing the affine transformation in the normalization layers, which helps to prevent overfitting and improve the generalization performance of the network. GAN-SPADE is a powerful approach for generating high-quality realistic images from semantic layouts and has been used for a variety of applications in computer vision and graphics.

### 3.9.2 Synthetic dataset generation

In order to train the GAN-SPADE deep neural network to be able to generate synthetic realistic-looking STEM images of dislocations from semantic layouts, a previously manually labeled dislocation dataset was used, then this pre-train network was utilized to create a large synthetic dataset to train 3D CNN neural network.

To obtain a large dataset to train a 3D CNN network synthetic stereo-pairs need to be created. Stereo-pairs of semantic layouts were generated from real 3D reconstruction results from the training dataset. 3D reconstructions from 49 real skeletonized dislocation sets were projected into 2D randomly by applying various degrees of rotation, focal lengths, and amount of dislocation structures. This operation allowed to generate a 1000 stereo-pairs of semantic

layouts, which later are given to GAN-SPADE as inputs to generate realistic-looking STEM stereo-pairs of dislocations. Fig. 3.9 represents the pipeline for synthetic dislocation dataset generation using GAN-SPADE.

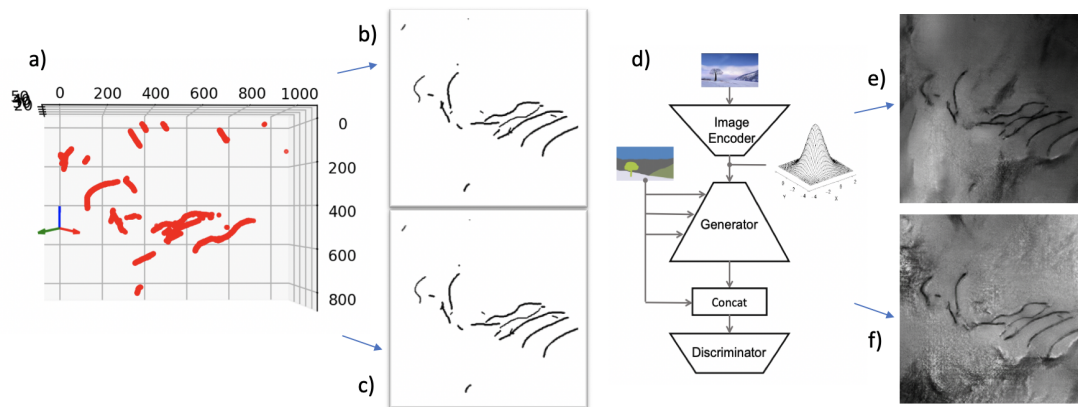


Figure 3.9: Synthetic dislocation dataset generation pipeline using GAN-SPADE deep learning neural network: (a) Skeletonized 3D reconstruction from the manually labeled training dataset, (b), (c) 2D projections of (a) given as an input to pre-trained (d) GAN-SPADE, (e), (f) Synthetically generated dislocations from semantic layouts (b) and (c).

An additional 1000 stereo-pairs generated by GAN-SPADE reveal a very similar contrast of the dislocations and the background that is observed in real experimental STEM images. Examples of the synthetic dislocation images can be seen in Fig. 3.10.

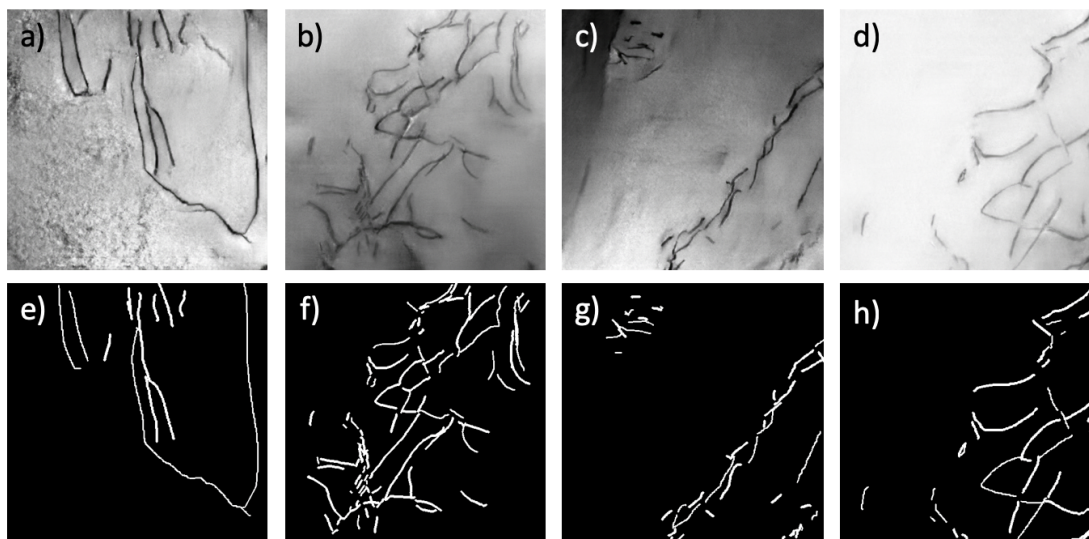


Figure 3.10: (a), (b), (c), (d) Synthetically generated dislocation images by GAN-SPADE network and (e), (f), (g), (h) corresponding semantic layout that was given to the network as an input.

Additional artificial datasets in combination with real STEM dislocation images manually

labeled were used to train 3D CNN. Enlargement of the training dataset increased the precision of the 3D reconstruction. Depth error estimation demonstrated that the synthetic dataset improved 1px error by 5%.

### 3.10 Concluding remarks

As shown in this chapter of the thesis, stereo reconstruction of curvilinear structures can be automatized and deliver an accuracy comparable to its established multi-view alternative, tomography. One of the advantages of this approach is that a learning-based detection pipeline eliminates the need for manual thresholding of final reconstruction results, unlike tomography, while it also enables us to apply structure-aware matching. It is evident that stereo matching of curvilinear structures may be learned from human-labeled data by deep convolutional neural networks leveraging visual similarities between structures in stereo. Although relying on visual appearances yields accurate matches, it also limits the tilt range of operation since the visual similarity of curvilinear structures rapidly degrades with increasing tilt angle. In these experiments, it was shown that good performance may be acquired with stereo-pairs having  $8^\circ$  of stereo-angle.

It has been demonstrated that training dataset size can be increased noticeably by using modern deep neural networks for image generation, like GAN-SPADE. It is especially important in the field of electron microscopy imaging due to the fact that obtaining a vast quantity of TEM images that is necessary for deep network training requires a significant investment of time. Enlargement of the training dataset allowed to increase the performance of the matching network.

In conclusion, stereo-vision remains to be an acceptable alternative 3D reconstruction approach for curvilinear structures, especially when acquiring a large number of images is costly in terms of time and manual effort. Moreover, thanks to the recent advancements in deep neural networks, detection, and matching tasks now may be combined in one neural network architecture and learned jointly. Therefore proposed network architecture is designed for matching curvilinear structures that deliver good performance in a wide variety of microscopy images while automatizing the process.



## 4 Tilt-less 3D imaging and reconstruction of dislocations

As demonstrated before, STEM is a powerful technique for imaging dislocations due to the absence of dynamic effects that significantly influence the contrast of dislocations and the micrograph's background contrast. Also, STEM is the base of the tilt-less 3D imaging technique, recently developed by Dr. Emad Oveisi at EPFL [32].

The recent development of fast segmented and pixelated STEM detectors opens up new opportunities for analyzing materials and their properties in the field of material science. It found many interesting applications in the imaging of electromagnetic fields and high-resolution imaging of beam-sensitive materials. In particular, the utilization of segmented detectors allowed to perform differential phase contrast (DPC) imaging by recording directly the electron beam deflection [66], [67], to obtain magnetic domain structures in thin foils [68], to perform ultra-high contrast STEM imaging with low-dose at atomic scale [69]. Pixelated detectors demonstrated high performance in terms of detector quantum efficiency (DQE) and lower noise values even in the low-dose exposures [70], allowed to improve further the efficiency of the magnetic imaging in STEM [71].

The combination of the tilt-less 3D imaging technique with modern STEM detectors can significantly reduce the time of the experiment and improve the image quality for the following 3D reconstruction. This approach also allows to increase the number of views on the sample.

In order to improve the tilt-less 3D imaging a series of experiments on a Cs-corrected microscope were performed. Cs-correction allows to obtain a large convergence angle of the probe with fewer aberrations, compared to non-corrected microscopes, and hence to increase the stereo angle between two images from  $1.4^\circ$  to  $3.2^\circ$ .

The advantages and application of these techniques will be discussed in this section of the thesis on the example of dislocation images from TiAl alloy. Following 3D reconstruction will be performed with our novel stereo approach utilizing deep learning neural networks that allow obtaining the automatic 3D distribution of the dislocations within seconds on a normal CPU.

## 4.1 Tilt-less 3D imaging principle

Tilt-less 3D imaging technique allows the acquisition of a stereo-pair of images in a single sample tilt using STEM imaging mode. The convergence of the STEM probe can be considered as multiple beams going through the sample under different tilt angles. When the sample is in a two-beam diffraction condition, by choosing two counterparts of the transmitted beam with the same excitation error a stereo-pair can be recorded without the necessity of tilting the sample or the electron beam. This technique brings many advantages in the 3D imaging of crystallographic defects such as the elimination of lateral shifts between two images, constant dislocation contrast on both views with the possibility to maintain the same Bragg diffraction vector, which is not always convenient when acquiring stereo-pair by tilting the sample due to the fact that microscope goniometer tilt-axes is not always perfectly aligned with the diffraction vectors. It also allows to decrease the imaging and sample beam exposure times, which is crucial in the case of beam-sensitive samples. A schematic illustration of the tilt-less 3D imaging technique is shown in Fig. 4.1.

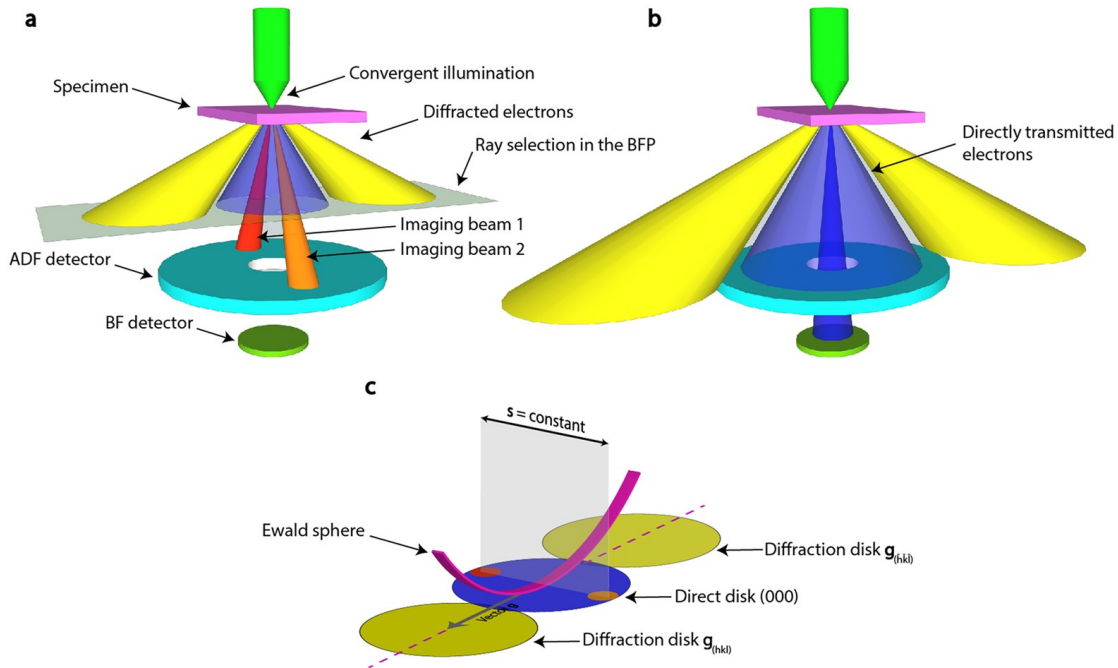


Figure 4.1: Schematic illustration of the tilt-less 3D imaging technique: (a) Imaging with an inclined direct beam (imaging beam 1 and 2), colored in red and orange: an aperture in the back focal plane (BFP) is placed on the edge of the directly transmitted disk, which is collected by an annular detector. (b) Imaging with a conical beam along the optical axis, colored in blue: the BFP aperture is removed, and the on-axis BF detector receives the center of the direct disk. (c) Illustration of the convergent beam electron diffraction (CBED) pattern corresponding to the diffraction condition shown in (a). Orange and red circles indicate the position of the BFP aperture for imaging conditions of beams 1 and 2, respectively. Courtesy of Emad Oveisi [9].

In comparison to the conventional acquisition of a tilt series, in tilt-less 3D STEM imaging, the

electron beam does not need to be refocused to form an image due to the constant height of the sample and the detector's position.

Tilt-less 3D STEM imaging of dislocations in the GaN layer of a heteroepitaxial InAlN/GaN-based membrane has been demonstrated by E. Oveisi on the stereo micrographs obtained with objective aperture displacement with a virtual tilt angle of 27.2 mrad ( $1.56^\circ$ ) [32]. In order to obtain a perception of the 3D shape of dislocations, two color-coded micrographs (chromatically opposite, typically red and cyan, one for each eye) need to be integrated into one stereoscopic image, called anaglyph, and viewed with color-coded glasses. Alternatively, a 3D reconstruction algorithm was proposed that employs computer vision techniques to match contours across the images and deduce their 3D shape [72]. However, the proposed algorithm performs in a semi-automatic way, where the start and end points of dislocation should be pointed manually, which complicates the process in the case of dense dislocation networks and their entanglement.

## 4.2 3D imaging and reconstruction with objective aperture displacement

Tilt-less 3D STEM imaging with TEM objective aperture displacement in the BFP was performed on the dislocations in electropolished TiAl alloy with the following 3D visualization using anaglyph image, Fig. 4.2. Experimental images were acquired on the HAADF detector in the STEM mode on a Tecnai Osiris microscope at 200kV. The sample was tilted to excite the (002) two-beam diffraction condition and  $\mathbf{g}$ -vector was oriented vertically on the fluorescent screen using a special rotation holder in order to have a vertical virtual tilt axis between the two views so that epipolar line and corresponding stereo-shifts are horizontal. This is done to avoid the need for rotating the images. The apparent rotation of the diffraction pattern is  $90^\circ$  with respect to the STEM images. The convergence angle was set to 12 mrad; in order to achieve this value the beam-forming condenser aperture with size  $70 \mu\text{m}$  was used. The CBED diffraction pattern was then projected to the HAADF detector using a large camera length, 1100 mm. Stereo-pair of STEM images (b) and (c) with 2048 by 2048 pixels was then recorded sequentially by placing the objective aperture at the top and bottom of the BF disc (a) along with the Kikuchi line where the excitation error is constant, stereo-angle is  $1.4^\circ$ . The resulting red-cyan anaglyph can be seen in Fig. 4.2 (d).

By viewing the anaglyph in Fig. 4.2 (d) with color-coded glasses one can get the perception of the 3D nature of dislocation network distribution, however, it requires practice and can remain not obvious for some viewers.

By applying our deep learning network pipeline a more straightforward and precise 3D visualization can be obtained. Fig. 4.3 shows a stereo-pair of dislocations in BF-STEM images (a) and (b) acquired previously and corresponding segmentation results obtained with pre-trained UNet neural network (c) and (d), followed by 3D reconstruction by 3D CNN (e).



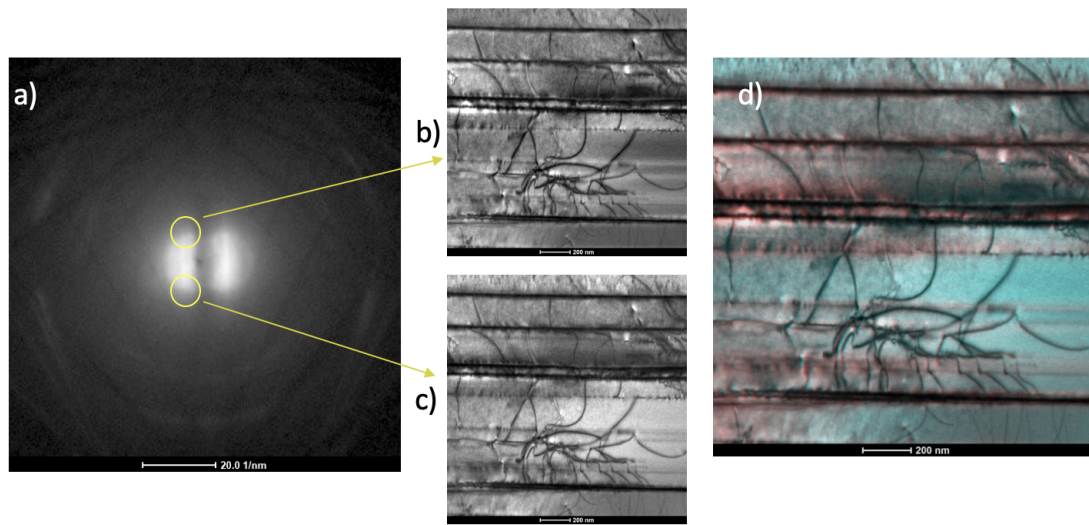


Figure 4.2: Tilt-less 3D imaging workflow with objective aperture displacement: (a) STEM diffraction pattern in two-beam diffraction condition with yellow masks representing objective aperture positions, Stereo-pair of BF-STEM images (b) and (c) recorded from the two positions of the TEM objective aperture in the BFP (a), resulting anaglyph of the dislocations in TiAl alloy (d). Best viewed with red-cyan glasses.

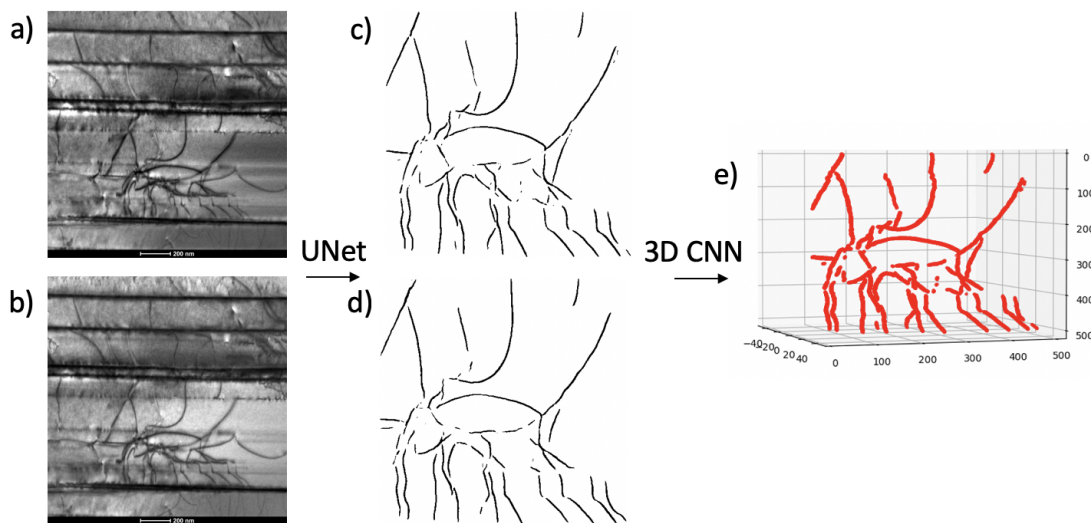


Figure 4.3: 3D reconstruction pipeline from the tilt-less 3D imaging with objective aperture displacement: (a), (b) BF-STEM stereo-pair with  $1.4^\circ$  of stereo-angle, (c), (d) Corresponding segmentation by UNet neural network, (e) Final 3D reconstruction by 3D CNN.

For the reconstruction purposes in Fig. 4.3 original stereo-pair of images (a) and (b) was cropped, so that only the region of interest with dense dislocation network in the middle was used for the contour detection, and matching by deep learning neural networks.

### 4.3 One-shot 3D imaging using segmented detector

Further improvements in the field of tilt-less 3D imaging and 3D reconstruction arise from the utilization of an annular segmented detector where four images can be acquired simultaneously from the four quadrants: A, B, C, and D, see Fig. 4.4. This imaging technique significantly reduces the time required for the acquisition of a stereo-pair as well as eliminates the necessity of manual adjustments of the objective aperture during the stereo-pair acquisition, since the objective aperture is not used in this case.

An additional advantage comes from the fact that the segmented detector is installed on the Cs-corrected Titan Themis microscope available at CIME, EPFL. Cs-correction allows using larger convergence angles compared to the previous generation of microscopes without probe correction while still maintaining the phase of the beam almost flat (i.e. fewer aberrations in the images acquired from the rim of the BF disk). This allows for obtaining larger virtual tilts between the two images from the opposite segments of the detector. By using the  $70\mu\text{m}$  probe forming condenser aperture it is possible to achieve a 28 mrad convergence semi-angle, so the value of the stereo-angle is  $3.2^\circ$ .

The sample and its diffraction pattern during the tilt-less 3D imaging with a segmented detector need to be carefully adjusted relative to its quadrants since they are fixed in their position. This is necessary for reconstruction purposes, to maintain the same contrast level and dislocation visibility for STEM stereo-pair from the two opposite segments of the detector: B and D at Fig. 4.4. For this purpose, it is required to use a dedicated rotation holder or adjust the current in the projector lens system, which will allow to rotate the diffraction pattern and cover the opposite segments of the detector with the transmitted disc along with the same values of the excitation error, see Fig. 4.5(a). However, the latter can induce a change in the value of the convergence angle, i.e. the stereo-angle between the two views. Tilt-less 3D imaging with a segmented detector with four quadrants allows acquiring only two images that can be used for the 3D reconstruction due to the constrain from the diffraction contrast phenomena. Images A and C in Fig. 4.4 have a contribution from different values of the excitation error, and as a result, exhibit distinct differences in the contrast of dislocations and the background of the image, therefore, they can't be used for reconstruction purposes.

Another challenge of tilt-less stereo-pair acquisition with a segmented detector is to choose the optimum value of the detector collection angle by changing the camera length (CL) parameter of the microscope. When CL is set too low, the angle between the two views is at its maximum, however, the signal-to-noise ratio of the images is low too, and the opposite. This occurs because, at low values of CL, the transmitted beam projected onto the segmented detector covers only a small portion of it, with the central middle section often falling within the inner hole of the detector. The next chapter of the thesis will be dedicated to the quantification of the various experimental parameters related to the 3D imaging with the segmented detector and to the selection of the optimum ones that deliver larger stereo-angle while maintaining a good quality of the dislocation images, and therefore work the best with our 3D reconstruction

pipeline.

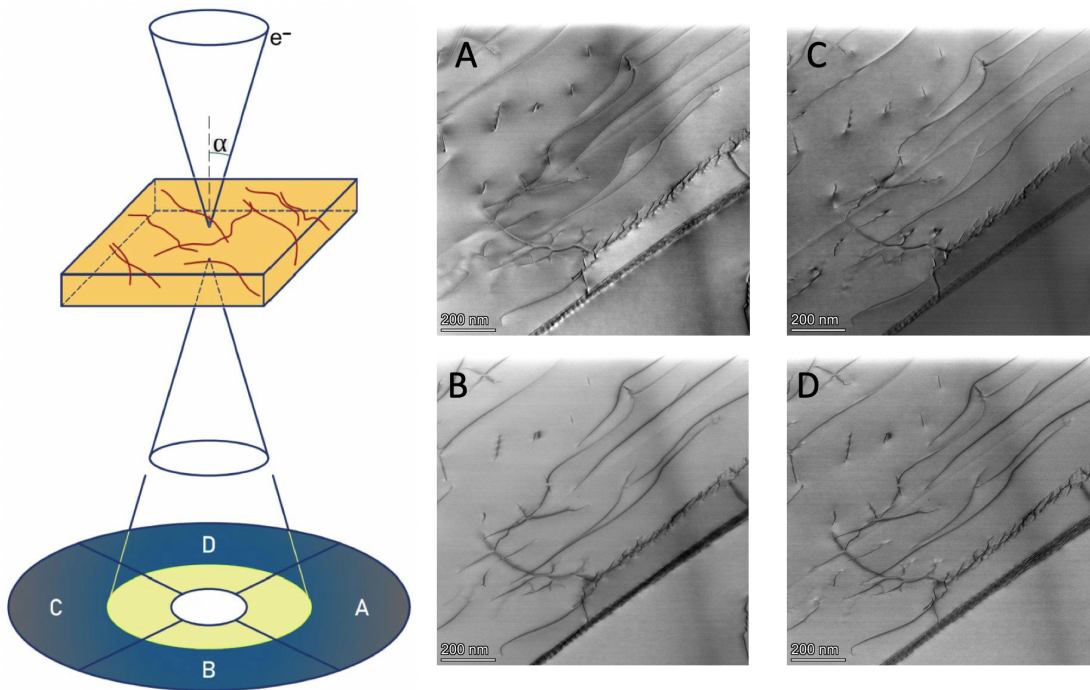


Figure 4.4: Single-shot 3D imaging scheme with segmented detector: electron probe with convergence angle  $\alpha$  is scanning pixel by pixel the sample with dislocations, transmitted beam is recorded in the segmented detector with four quadrants: A, B, C, and D, allowing to acquire four STEM images simultaneously.

Figure 4.5 represents the workflow for the tilt-less 3D imaging with the following 3D reconstruction using the segmented detector with four quadrants and deep learning neural network approach. The convergence semi-angle of the probe projected on the detector is 28 mrad with two parts of the transmitted beam (BF disc) at the segments B and D. To form the stereo-pair for the following 3D reconstruction two images were selected from the opposite segments where the excitation error is the same for both views. Then our automatic approach was applied to perform the 3D reconstruction. The first step is dislocation detection using a pre-trained UNet neural network, the second step is the stereo-matching of the corresponding points along the epipolar line using 3D CNN to obtain the final 3D reconstruction. The stereo-angle is approximately  $3^\circ$ .

In the previous chapter of the thesis which was dedicated to the deep learning algorithm for performing automatic 3D reconstruction it was mentioned that the optimal value of the stereo-angle is  $8^\circ$ , this value allowed to obtain high-quality 3D visualization of dislocations with the smallest depth errors. In order to further increase the stereo-angle for tilt-less 3D imaging one need to use a larger probe forming condenser aperture. The Titan Themis microscope is equipped with a  $150\mu\text{m}$  condenser aperture, which permits to receive the electron probe with 60 mrad of convergence semi-angle, which corresponds to an angle of  $6.8^\circ$  between the

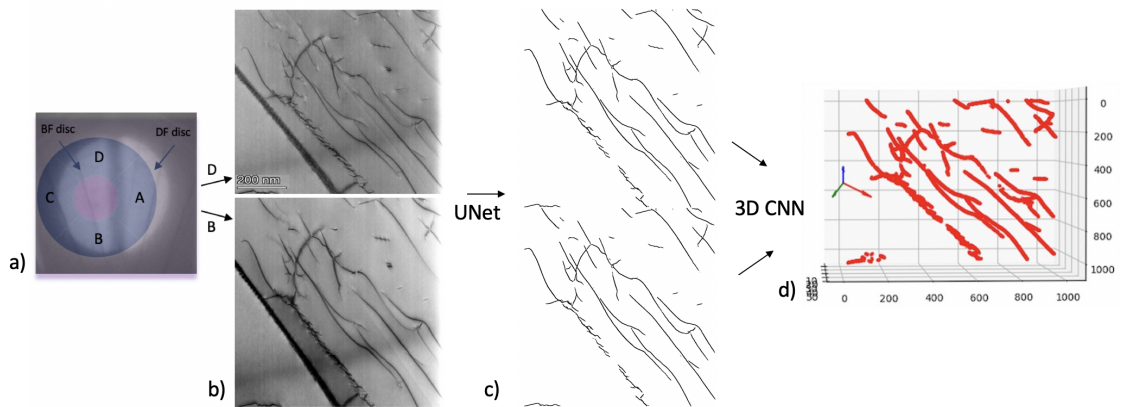


Figure 4.5: Tilt-less 3D imaging and reconstruction of dislocations workflow using a segmented detector with four quadrants: (a) Segmented detector's scheme superimposed with the STEM diffraction pattern in two-beam diffraction condition, where two opposite sides of the BF disc with the same excitation error cover two opposite segments B and D of the segmented detector, (b) Stereo-pair STEM images of dislocations in TiAl alloy acquired from the segments B and D, (c) Corresponding segmentation results by pre-trained UNet network, (d) Final 3D reconstruction of dislocations performed by 3D CNN in the crystallographic coordinate system.

images in a stereo-pair.

However, the tilt-less 3D imaging with a segmented detector using the electron beam with a 60 mrad convergence angle did not provide satisfactory results, and the following detection and matching with neural networks were not possible due to distortions and high noise levels of the images. Fig. 4.6 illustrates a stereo-pair of STEM images of dislocations acquired using the  $150\mu\text{m}$  condenser aperture with the segmented detector and corresponding segmentation results by UNet. This figure displays a poor level of dislocation lines detection, especially in the regions affected the most by the high-order aberrations of the electron beam. Additional training with few images from this dataset was performed in order to improve the performance of the neural networks for this particular imaging condition, though the size of the dataset was not sufficient to improve the results.

Distortions in the images at large values of the convergence angles come from high-order aberrations in the electromagnetic lens system, which can be seen at the virtual phase plate from the probe corrector software in Fig. 4.6 (a). When the convergence angle is larger than 23 mrad, the shape of the probe becomes increasingly distorted, leading to reduced imaging resolution. When performing 3D imaging using  $150\mu\text{m}$  condenser aperture, the signal on the segmented detector degrades because of the deformations of the probe at the higher convergence angles, especially due to the size and shape of the segments, that integrates intensity over even larger regions of CBED pattern, so including more distorted regions.

Also, integration over large regions of CBED pattern with a segmented detector comes with



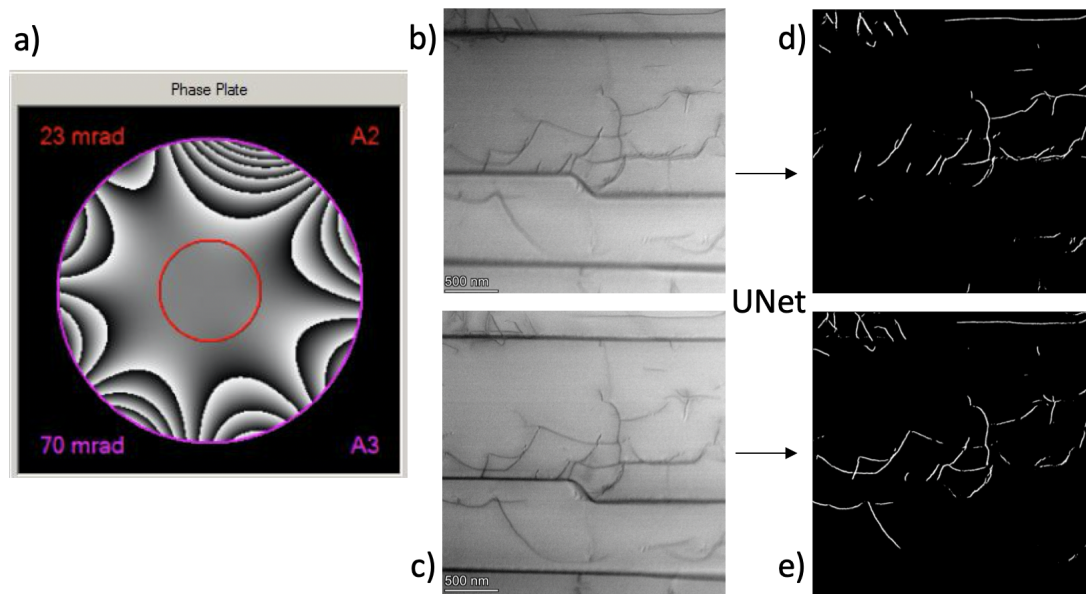


Figure 4.6: Tilt-less 3D imaging of dislocations in TiAl alloy using  $150\mu\text{m}$  condenser aperture with segmented detector: (a) Virtual phase plate of the electron beam from the probe corrector software acquired with the  $70\mu\text{m}$  condenser aperture, (b), (c) Stereo-pair STEM images of dislocations in TiAl alloy acquired with  $60\text{ mrad}$  convergence angle from the segments B and D, (d), (e) Corresponding segmentation results by pre-trained UNet network.

a challenge to estimate precisely the tilt angle between two images, which is important for performing triangulation and obtaining an accurate 3D reconstruction.

#### 4.3.1 Crystallographic coordinate system for 3D reconstruction

Our 3D reconstruction method was updated by introducing the fractional coordinate system of a crystal which gives more insights into the dislocation structure within the new reference system. Now crystal vectors (**a**, **b**, **c**) are integrated into the final 3D reconstruction by 3D CNN neural network, those vectors colored in red, green, and blue respectively in Fig. 4.5 (d). To introduce a crystallographic frame of reference to the 3D reconstruction, the unit cell parameters of the material, and the diffraction condition used for imaging (zone axis  $[u, v, w]$ , diffraction vector  $(h, k, l)$ , as well as the tilt angle to that particular zone axis) need to be given as an input to the graphical interface of the software for 3D reconstruction.

### 4.4 Tilt-less 3D imaging and reconstruction using pixelated detector

As discussed in the introduction of the thesis, instrument advancements in the field of STEM detectors, for example, new direct electron detectors (DED), in particular, pixelated detectors improved dramatically the imaging of materials and opened new perspectives. Detector quantum efficiency (DQE), and signal-to-noise Ratio (SNR) of modern pixelated detectors

improved a lot in comparison to that of segmented detectors from the previous generation.

The use of pixelated STEM detectors allows to perform 4D-STEM (Four-Dimensional Scanning Transmission Electron Microscopy) experiments. Conventional STEM imaging allows obtaining only spatial information of the sample, but 4D-STEM surpasses this by also collecting the angular distribution of electrons pixel by pixel. By recording the diffraction pattern produced by the scattered electrons at each position of the electron probe, a 4D dataset is generated, see Fig. 4.7 (a) for the schematic representation of the 4D-STEM imaging technique. The angular-resolved electron scattering information in the back focal plane of the sample is then used in the formation of STEM images, offering a broad spectrum of helpful data about the sample. 4D-STEM diffraction imaging provides the opportunity to use "virtual" detectors and transform them by collecting various subsets of pixels in the diffraction plane at each probe position. This is not possible with conventional STEM detectors when a number of BF and ADF detectors are fixed relative to each other and cannot be changed during the experiments so that electrons cannot be further segregated by scattering angle.

A combination of the tilt-less 3D imaging technique with pixelated STEM detectors allows, therefore, the acquisition of only one 4D-STEM dataset with a large value of convergence angle at a single sample tilt and then obtaining numerous stereo-pairs during the post-processing using various sizes and positions of the "virtual" detectors in the diffraction plane, which was not possible when working with the segmented detectors. Another advantage of using a pixelated detector is the ability to have more control over the value of the tilt angle between the two views on the sample, and the power of defining it more precisely than with the segmented detector.

#### 4.4.1 4D-STEM experimental procedure

Acquisition of the 4D-STEM dataset was performed on the Titan Themis Cs-corrected microscope equipped with the MerlinEM pixelated detector with an array of (256, 256) pixels. After alignment of the microscope, the sample was tilted to a two-beam diffraction condition with  $\mathbf{g}=(002)$  as the excited reflection. When the region in the sample with dislocations visible was chosen for the 4D-STEM experiment, the number of pixels and pixel size in real space was determined. For the dataset in Fig. 4.7, (256, 256) pixels were selected for scanning in real space with a one-pixel size equal to 4.32 nm, and frame time was set to 8  $\mu\text{s}$ . So the size of the final 4D dataset is (256, 256, 256, 256). The MerlinEM pixelated detector has various counting options, in this experiment, 2x12Bit mode was chosen which allows to acquire up to 2000 fps. The camera length value was adjusted in order to fit the diffraction pattern projection on a pixelated detector, here with a convergence semi-angle 60 mrad, it was set to CL=37mm. Des-can option was used when needed to avoid horizontal movements of the diffraction pattern during the process of scanning the sample. Finally, another 4D-STEM was acquired without any sample, which allowed to perform imaging and marking of the position of the condenser aperture, in order to perform the calibration of the diffraction pattern, see Fig. 4.7 (c).

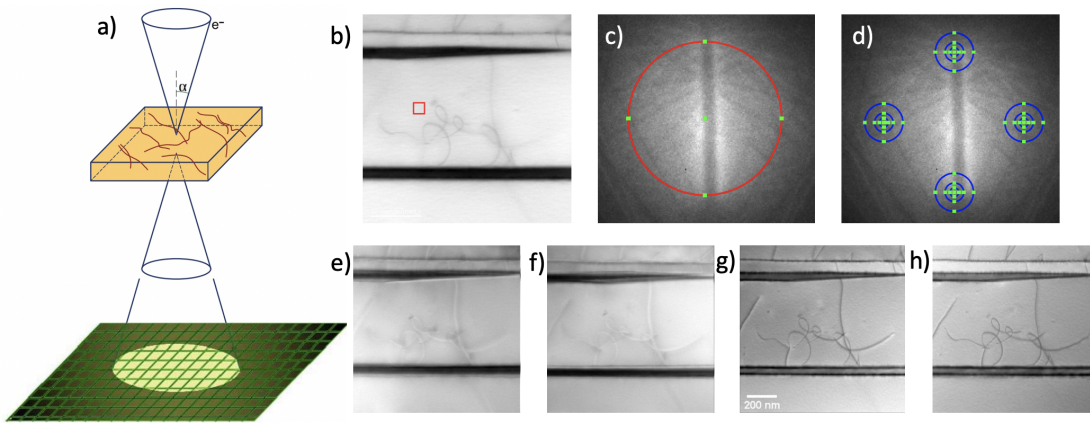


Figure 4.7: 4D-STEM imaging workflow with pixelated detector: (a) Schematic illustration of 4D STEM imaging on a pixelated detector with (256, 256) pixels, (b) Averaged scan region in a real space, (c) Calibrated diffraction pattern in a reciprocal space integrated from the red rectangular at (b), (d) Four "virtual" detector positions on the diffraction pattern, (e) and (f) - Virtual BF-STEM images from left and right detector positions, (g) and (h) - Virtual BF-STEM images from top and bottom detector positions along the Kikuchi line at the (d). Stereo-angle between each pair of images is 6.88 degrees.

To obtain STEM stereo-pairs of dislocations after the acquisition of the 4D-STEM dataset dedicated Python packages were used and implemented in Jupyter Notebook [73]. First, the open-source 4D-STEM analysis toolbox Pyxem was used to open and read the MerlinEM format of the dataset, as well as to perform virtual BF imaging [74]. Second, custom scripts were added to the Jupyter Notebook to obtain stereo-pairs of dislocation images. The full pipeline of the 4D dataset treatment is represented in Fig. 4.7. As one can see now it is possible to generate multiple views of the sample in the post-processing of the 4D-STEM dataset, stereo-pair from images (g) and (h) can be further used for 3D reconstruction by deep learning neural networks, since they reveal similar contrast due to same value of excitation error. Because of the calibration of the diffraction pattern (red circle in Fig. 4.7 (c)) with the 4D-STEM dataset acquired in a vacuum, one can not only define more precisely the positions for the "virtual" detectors (blue circles in Fig. 4.7 (d)) but also perform an accurate calculation of the stereo-angle, which is done automatically in the Jupyter notebook.

#### 4.4.2 3D reconstruction by deep learning neural networks

By applying tilt-less 3D imaging on a fast pixelated STEM detector and using our deep learning algorithm, the 3D reconstruction of dislocations from virtual stereo-images extracted from the 4D STEM dataset is generated. Fig. 4.8 depicts the 3D reconstruction procedure from the 4D STEM dataset using a convergence semi-angle of 60 mrad, with a stereo-angle between the images of  $6.54^\circ$ . Pairs of virtual stereo STEM images are formed by selecting the two counterpart regions of the direct disc on the diffraction pattern with the same value of excitation error. The

images are then treated by CNNs to provide dislocation detection and 3D reconstruction. This approach offers the possibility to obtain a larger stereo-angle between the views compared to the segmented detector while improving the angular resolution, as well as delivers the possibility to increase the number of views on the sample which can improve the precision of the 3D reconstruction. Furthermore, the parameters for SNR and angular resolution can be optimized due to the specific size of the "virtual" detectors for the intensity integration during the post-processing.

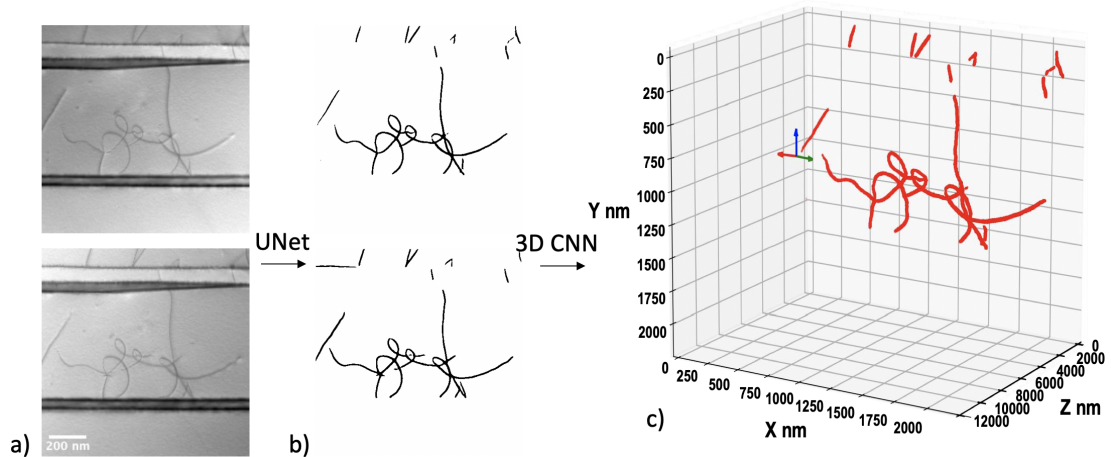


Figure 4.8: 3D reconstruction pipeline from images acquired with pixelated detector: (a) Stereo-pair of dislocations in TiAl alloy created from 4D-STEM dataset, (b) Segmentations of stereo-pair in (a) by UNet neural network with detected dislocation lines, (c) 3D reconstruction from detected dislocations in (b) by 3D CNN in the crystallographic frame of reference. Stereo-angle is  $6.54^\circ$ .

#### 4.4.3 Network training with 4D STEM images

Another advantage of using a pixelated detector is the ability to produce a larger training dataset with various noise levels of the images while labeling only a few of them. It is made possible by generating multiple virtual STEM images of dislocations from the "virtual" detectors with different radii, but the same coordinates of its center can be seen in Fig. 4.9 a). This allows to produce the STEM images with the same viewing angle or virtual tilt, and by changing the radius of the virtual detector, allows to vary noise levels in the images, see Fig. 4.9 c)-h). Following the fact that all these images represent identical distributions of dislocations, labeling can be performed only once and used on all sequences.

Labeling dislocations in STEM images is a tedious process that requires human labor and time. Training dataset creation from 4D-STEM datasets allows to decrease the number of STEM images for dislocation labeling and to train the model with various levels of noise. After performing the additional training of CNNs it was possible to obtain a more adaptable neural network model that was robust to the noisy STEM images.



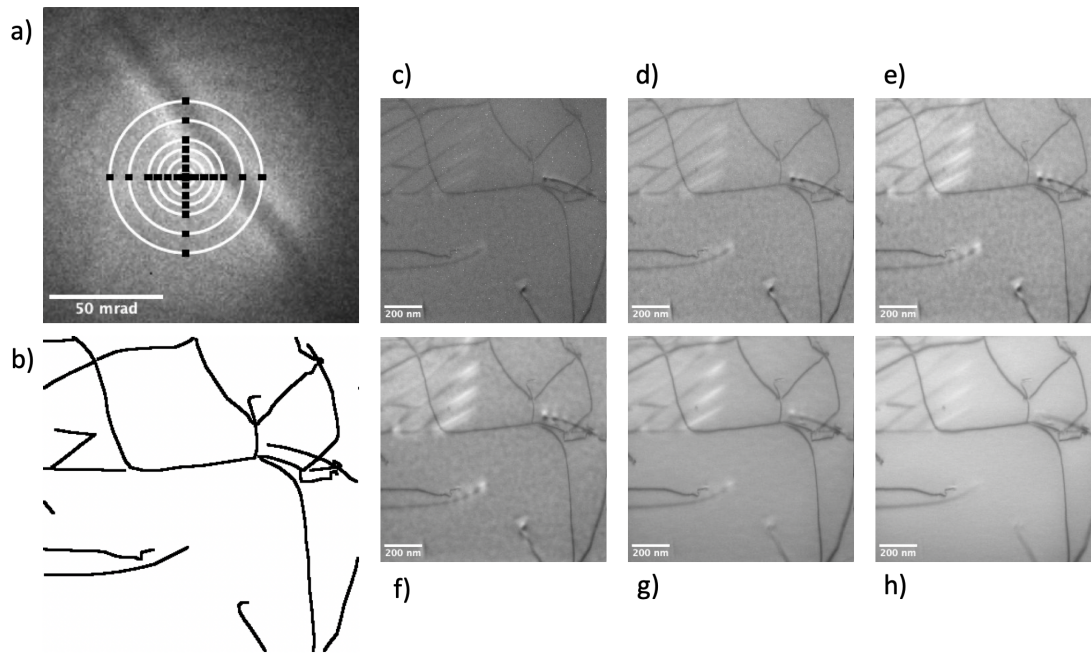


Figure 4.9: Training dataset creation from 4D-STEM dataset: (a) Diffraction pattern in two-beam condition projected on the pixelated detector with circles representing "virtual" detectors with various radii and same coordinates of the circles' center, (b) Labeled virtual BF-STEM image of dislocations in TiAl, (c)-(h) Virtual BF-STEM images created from circles in (a) with radii 5, 10, 15, 20, 30, 40 pixels correspondingly.

This procedure also allows to minimize so-called *domain gap*. Domain gap in the field of Computer Vision refers to the discrepancy between the distribution of data in the training set and the distribution of data in the real-world scenario where the model is deployed. Since our CNNs were trained with STEM images acquired on a BF and annular ADF detectors, application of the model to the images from the 4D-STEM dataset obtained with pixelated detector may cause CNNs' performance degradation due to the differences between the two types of dataset. The addition of the labeled training subset from the pixelated detector can improve the performance of the CNNs on the 4D-STEM dataset and reduce the domain gap.

#### 4.4.4 Convergence angle maximum

The Titan Themis microscope allows to obtain the convergence semi-angle of 60 mrad with the largest condenser aperture of  $150\mu\text{m}$ , this corresponds to  $6.8^\circ$  for the stereo-angle. However, as reported in Chapter 3, stereo-pairs of STEM images of dislocations with  $8^\circ$  of tilt between them deliver the lowest depth errors in the 3D reconstruction. To obtain an identical value of the virtual tilt for the tilt-less 3D imaging the convergence semi-angle needed to be further increased. In order to increase its value there is a possibility to adjust the current in C2 and C3 condenser lenses. This allowed to obtain precisely 70 mrad of the convergence semi-angle, i.e.  $8^\circ$  of the stereo-angle between the STEM images and to perform 3D reconstruction.

In this section of the thesis, an investigation of the maximum value of the convergence semi-angle was performed for the Titan Themis microscope. The highest convergence semi-angle feasible for this microscope was derived by tuning the current in C2 and C3 lenses and a 91 mrad value was obtained. This gives microscopy users the ability to increase the stereo-angle up to  $10^\circ$  without the necessity of tilting the specimen.

Due to the fact that integration of a signal in the diffraction plane can be done very locally by using "virtual" detectors with a small radius, the virtual STEM images can have very little influence on aberrations even with such large convergence semi-angles.

Acquisition of the 4D-STEM dataset with convergence semi-angle 91 mrad was performed in 2x12Bit-mode with  $8\mu\text{s}$  frame time and pixel size 4.320 nm. The total 4D dataset size is (256, 256, 256, 256). Virtual BF-STEM images were formed from the two counterparts of the BF disc by placing "virtual" detectors with 25-pixel radii, which corresponds to 20 mrad. Virtual BF-STEM images from the pixelated detector with stereo-angle of  $9.32^\circ$  and corresponding CNNs results can be seen in Fig. 4.10.

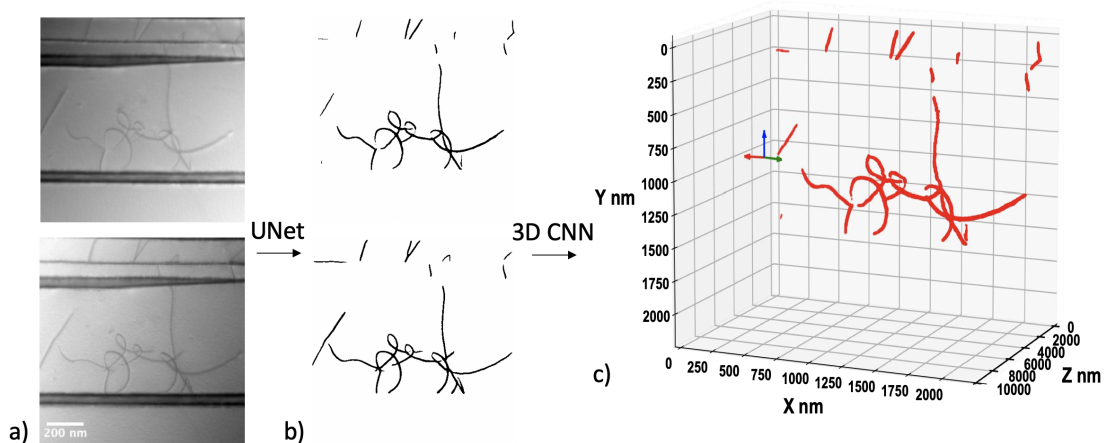


Figure 4.10: Automatic 3D reconstruction from STEM images acquired with pixelated detector: (a) Virtual BF-STEM stereo-pair of dislocations in TiAl alloy, (b) Detected from (a) dislocations by UNet neural network, (c) 3D reconstruction by 3D CNN in the crystallographic frame of reference and nm-scale. Stereo-angle between the images is  $9.32^\circ$ .

UNet neural network and following 3D CNN's results demonstrate a high level of performance, despite the fact that the STEM images are slightly blurred because of the high-order aberrations. As can be observed in Fig. 4.10 (b) and (c) there are only minor parts of dislocation lines weren't detected by UNet and, as a result, not reconstructed in the 3D volume. However, this does not hinder the overall perception of the final 3D reconstruction.

During the post-processing from the 4D-STEM dataset acquired in Fig. 4.10 it is possible to extract multiple stereo-pairs of dislocation BF-STEM images with various stereo-angles, in particular, with an optimal value of  $8^\circ$  for the following 3D reconstruction with CNNs.

## 4.5 Concluding remarks

As demonstrated in this chapter of the thesis, the tilt-less 3D imaging technique is an innovative valuable approach for 3D reconstruction and visualization of dislocations. It brings to the field a simplified acquisition of the stereo-pair without the necessity of tilting the sample, in comparison to electron tomography and stereo imaging with mechanical tilt.

Tilt-less 3D electron imaging with a segmented detector permits to perform 3D imaging via single-shot and to obtain the most rapid 3D distribution of the dislocations in combination with 3D CNNs. This approach also opens new applications for real-time 3D electron imaging of dynamic processes. However, the shape and the quality of the segmented detector available on the Titan Themis microscope do not allow to obtain stereo-pair of dislocations with large values of convergence angles, i.e. virtual stereo-angle, due to the prevailing aberrations. Also, the precise definition of the stereo-angle is not available, which can cause degradation of the triangulation procedure for 3D reconstruction.

Novel pixelated detectors are a game-changing approach to 3D imaging. For the first time, it was possible to create stereo-pairs of dislocations' STEM images with a virtual tilt of  $9.32^\circ$ . The high-quality 4D-STEM dataset was acquired at a single sample tilt. During the post-processing of the dataset, multiple stereo-pairs can be generated and utilized for 3D reconstruction and for neural network training. With the help of additional training procedures with virtual images from the 4D dataset, it was possible to reduce the domain gap between previous detectors and pixelated detectors and to improve the performance of the neural networks. In combination with our automatic 3D reconstruction pipeline, this method changes the whole field of 3D imaging.

The deep learning approach developed in collaboration with CVLab at EPFL, applied to the STEM images acquired via tilt-less 3D imaging technique enabled to considerably decrease the time required for 3D imaging and reconstruction, allowing to treat large amounts of data, which gives the microscopists the opportunity to study and analyze greater volumes of materials in a given period of time.

# 5 Quantification of 3D reconstruction

STEM imaging of dislocations is not a trivial procedure since their contrast and visibility strongly depend on many microscope parameters and crystallographic orientations of the specimen in the microscope. The quality of segmentation by detection network may also vary for different imaging conditions. For optimum detection and following 3D reconstruction of dislocations, one needs to choose imaging conditions that are the most suitable for deep learning neural networks, which might differ from the one an operator of the microscope would choose. It is therefore crucial to have a quantitative assessment of the quality of the segmentation and ultimately of the 3D reconstruction for different imaging parameters. In this chapter, a Topological Data Analysis (TDA) tool developed in UPHESS Lab at EPFL will be presented that allows analyzing the quality of the outputs from neural networks by comparing them to a manually annotated set of images (ground-truth).

## 5.1 Introduction

TDA uses algebraic topology tools to study and access topological and geometric information on the shape of the data [75]. It combines topology, the study of geometric properties that remain unchanged under continuous transformations, with data analysis to extract insights and patterns from complex data sets. TDA provides a way to study the shape and structure of data sets, regardless of the specific metrics used to measure similarity or distance between data points. These techniques are especially useful for data sets that have high dimensionality or are otherwise difficult to analyze using traditional statistical or machine learning methods. TDA methods in image processing help to provide a global view of images, which considers the intrinsic geometrical and topological properties of the images and complements them very well with standard methods. The topological descriptors are used to build topological distances between the neural network outputs with different imaging conditions and the ground-truth and choose the settings with the highest topological correctness [76]. In this work, particularly, the persistent homology tool from TDA is used [77], which allows extracting features representing the number of connected components, cycles, and voids together with their birth and death during an iterative process called a *filtration*. Each of those features is

then summarized as a point in a *persistence diagram*. The persistence diagram is a way to summarize the persistent homology information obtained from analyzing the data set. It is a graphical representation of the topological features of the data set and their persistence, which refers to the length of time that a feature exists as a function of a chosen scale or parameter. The persistence diagram is a scatter plot where each point represents a topological feature in the data set. The horizontal axis represents the birth of the feature, which corresponds to the scale or parameter value at which the feature first appears, while the vertical axis represents the death of the feature, which corresponds to the scale or parameter value at which the feature disappears or merges with another feature. The diagonal line through the center of the plot represents features that are born and die at the same scale or parameter value. The persistence diagram provides a compact and informative summary of the topological features present in a data set, allowing to easily identify and analyze the most persistent features, which are typically the most significant or meaningful from a topological perspective. Persistent homology is most used on point clouds, however, considering the voxel structure of images can be applied to the latter as well. It has been already applied to image classification tasks in [78]–[80], defining filtration based on techniques from image processing, like dilation or erosion, and generating intuitive features.

The output of the UNet neural network and a manually labeled ground-truth for the quantification procedure are binary images that represent segmentations of dislocations. A few types of filtration are used directly on these binary images in order to obtain persistence diagrams: dilation, height filtration, density, and radial filtration. Then persistence diagram from the ground-truth image was compared to the persistence diagrams of the outputs from the UNet neural network obtained from the STEM images under different imaging conditions, and the final topological score was acquired.

Fig. 5.1 demonstrates different types of filtration used in this work on the example of a binary image (a).

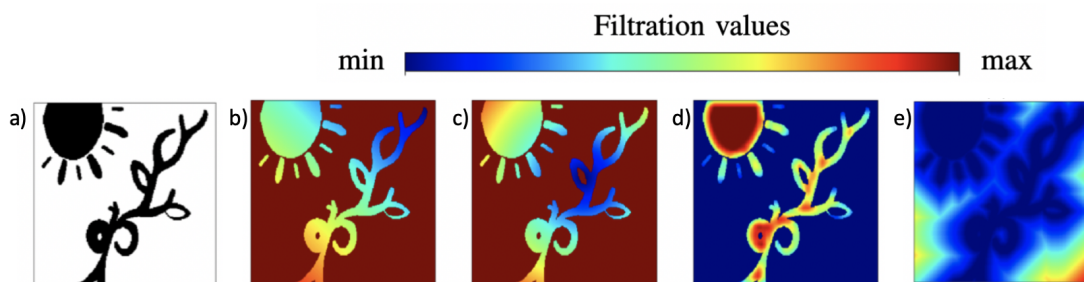


Figure 5.1: Grayscale images obtained from different types of filtrations. For visibility reasons, a colored map was chosen to represent grayscale values. The original binary image (a) was used to illustrate filtrations: (b) height filtration with vector  $(-1,-1)$ , (c) the radial filtration with the center in the blue leaf, (d) density filtration, (e) dilation filtration. Courtesy of Adélie Garin, [76].

Description of each filtration technique implemented in this work on the UNet segmentations

of the dislocation STEM images and the manually labeled ground-truth image are listed below:

*Height filtration.* In topology, height filtration is a way of assigning a real number (called the height) to each point in a topological space, in such a way that the points can be arranged in a sequence based on their heights. The height function can be used to create a filtration of the space, which is a sequence of subspaces obtained by gradually restricting the height values. In TDA the height function is defined based on a vector field [81]. The vector field assigns a vector to each point in the space, and the height function is defined as the projection of the vector in a fixed direction. By varying the direction of the projection, one can obtain different height filtrations, each of which captures different aspects of the topology of the space. In the context of image analysis, one could define height filtration with various vectors and directions on a grayscale image by using the image gradient as the vector field and projecting it in different directions. This would result in a sequence of sublevel sets (i.e., sets of points with height values below a certain threshold) that capture the topology of the image at different scales and orientations. The persistence of the homology groups of these sublevel sets can then be computed to extract topological features of the image, such as connected components, holes, and voids, that are robust to noise and deformation.

*Radial filtration.* In topological image analysis, radial filtration is a type of height filtration that assigns a height value to each point in a topological space based on its distance to a fixed center point [79]. The center point is usually chosen to be the centroid or the maximum intensity point of the image, but it can also be user-defined or vary depending on the application. Radial filtration is obtained by gradually increasing the radius around the center point and retaining the points within the radius. At each radius value, the set of retained points forms a sublevel set, which represents the part of the image that is below the corresponding height value. The sequence of sublevel sets obtained by varying the radius forms a filtration of the image, which can be analyzed using persistent homology to extract topological features such as connected components, holes, and voids. Radial filtration is particularly useful for capturing the multiscale structure of images, as it allows the topology of the image to be analyzed at different resolutions. It is also computationally efficient, as it only requires the computation of the Euclidean distance between each point and the center point.

*Density filtration.* The density filtration gives each voxel a value depending on the number of neighbors it has at a certain distance. To construct a density filtration, the image is first sorted based on the intensity values of its pixels or voxels, from the highest to the lowest. Then, a sequence of binary images is generated by thresholding the sorted image at increasing intensity values, from the highest to the lowest. At each threshold level, the binary image represents the connected components or regions of the image that have a pixel or voxel value greater than or equal to the threshold. The resulting sequence of binary images represents the topological features of the image based on the density of its pixel or voxel values, from the densest to the least dense regions.

*Dilation.* Dilation is an operation that expands the boundaries of a binary image or a grayscale

image. It is commonly used to enhance or extract image features, such as edges, lines, and objects. The dilation operation works by sliding a structuring element or a kernel over the image and replacing each pixel or voxel with the maximum value within the neighborhood defined by the kernel. In the case of a binary image, the result of dilation is a thickening or expansion of the object boundaries, while in the case of a grayscale image, the result is a smoothing or blurring effect. The size and shape of the structuring element or kernel used for dilation can be adjusted to control the degree of expansion or smoothing in the image. A larger structuring element will produce a more significant dilation effect, while a smaller one will produce a more subtle effect. To construct a dilation filtration, the image is first binarized by thresholding it to obtain a binary image. Then, a sequence of binary images is generated by applying a dilation operation to the binary image using structuring elements of increasing size. At each dilation level, the binary image represents the connected components or regions of the image that can be reached from the original foreground pixels or voxels by expanding them with the structuring element. The resulting sequence of binary images represents the topological features of the image based on the size and connectivity of its regions after dilation.

Example of the dilation filtration on the dislocations STEM images can be seen in Fig. 5.2 with corresponding persistence diagrams of the manually labeled ground-truth binary image (a) and of the UNet segmentation of the experimentally acquired STEM image of dislocations in TiAl alloy (b).

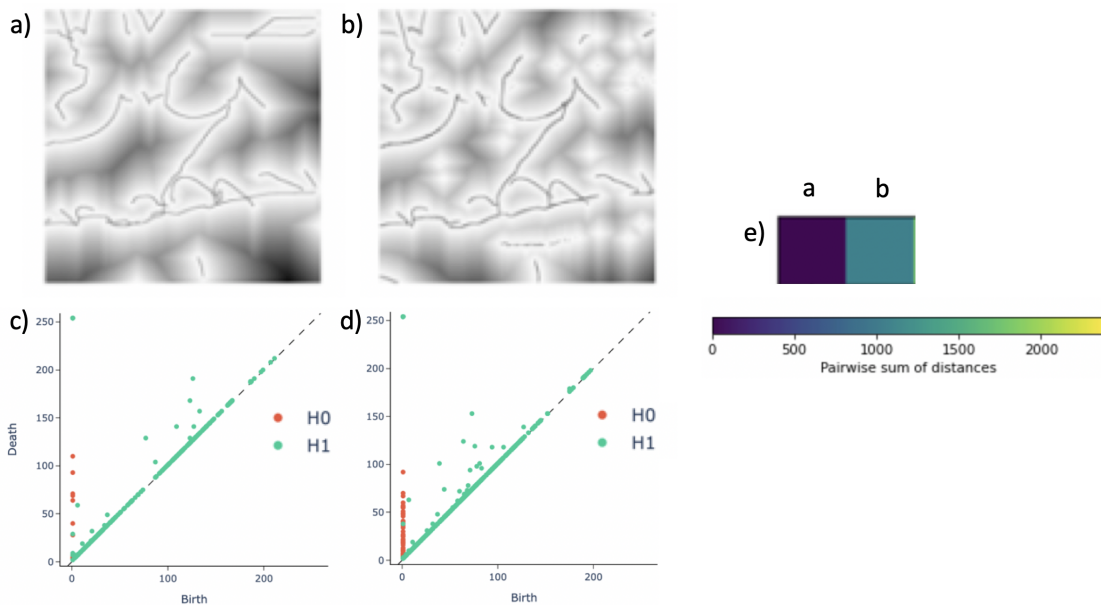


Figure 5.2: Dilation filtration example: (a) on a manually labeled ground-truth image and (b) on a UNet segmentation of experimentally acquired STEM image of dislocations in TiAl alloy, (c) and (d) corresponding persistence diagrams, (e) topological score of the ground-truth image (a) and UNet segmentation of experimental STEM image (b) for the dilation filtration.

Numbers H0 and H1 in persistence diagrams (c) and (d) in Fig. 5.2 represent the number of connected components and independent one-dimensional loops and holes in a topological

space respectively. The persistence diagram for H0 and H1 demonstrates the birth and death times of these components, with each point in the diagram corresponding to a component that appears and disappears at different time intervals. By calculating persistence diagrams for segmented images acquired under various conditions and comparing them to the ground-truth one can get a perspective of how "far" topologically this image is from the ground-truth (e). Evidently, for the ground-truth image (a) the topological score is zero since it is being compared to itself, however, the segmentation from UNet neural network (b) is topologically further from the ground-truth, because of the additional noise present in the image, and disconnections in the dislocation lines.

After performing the calculation of the topological scores for each filtration from the persistent diagrams from segmented dislocation images and the ground-truth, the final topological score of the dataset can be obtained. The final topological score for the dataset is acquired by the summation of the corresponding scores from all the filtrations that are used. In order to sum those scores machine learning (ML) optimization algorithm is utilized, which assigns to each filtration's score a particular weight or coefficient before summarizing them into the total topological score. ML algorithm chooses the weights for each particular filtration that are minimizing the error between the image and the ground-truth.

Utilization of TDA tools allowed to quantitatively estimate the quality of the segmentation outputs by the UNet neural network under different STEM imaging conditions, in order to be able to choose the ones which are working the best with the deep learning reconstruction approach and give the most precise results.

Two main criteria were chosen for the quantification of the UNet outputs and to calculate the final score:

- Connectivity of the dislocation lines on segmentation images.
- Noise level and presence of additional signals that do not exist in a ground-truth image.

## 5.2 Quantification of various STEM imaging conditions

In this section, along with the examination of various detector's collections angles  $\beta$  and excitation error  $s_g$ , the estimation of the dependence of the pixel size and dwell time on the segmentation and reconstruction results were performed. These experiments were done in STEM configuration on the Tecnai-Osiris S/TEM microscope at 200kV using the 70  $\mu\text{m}$  condenser aperture with corresponding 12.8 mrad convergence semi-angle of the electron beam, leading to a virtual tilt angle of 1.46 degrees.



### 5.2.1 Excitation error ( $s_g$ )

STEM dislocation contrast, among other parameters, is influenced by the crystallographic orientation of the specimen in the microscope. It can be adjusted by tilting the sample with respect to the electron beam direction. This procedure allows to fulfill the Bragg condition, exciting only one  $\mathbf{g}$ -vector, so-called two-beam diffraction condition. However, some deviations appear from the exact Bragg condition for a certain reflection  $\mathbf{g}$ . This deviation is called "excitation error" expressed as  $s_g$ . Fig. 5.3 shows a schematic representation of the positive excitation error in a two-beam diffraction condition, where the incident beam on the sample is at a larger angle than the ideal Bragg angle.

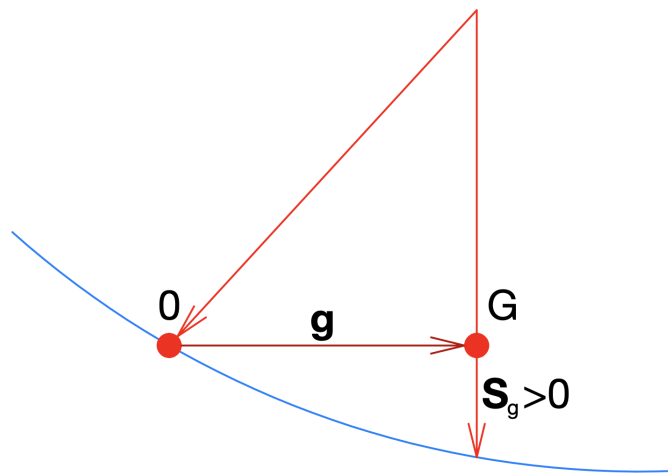


Figure 5.3: Schematic representation of the positive excitation error  $s_g$  in two-beam diffraction condition.

Conventionally, it is considered that for defect imaging and analysis, STEM images with a slightly positive excitation error are more advantageous than in exact two-beam diffraction conditions. The distortions due to the crystallographic defects are bending the planes of the crystal around them from the exact diffraction condition. Having a positive excitation error allows to bring the planes around the dislocation line back to the Bragg-diffraction condition, and to localize defects on the image more precisely than when using condition with  $s_g=0$ . This type of imaging allows to increase the sharpness of the dislocation line contrast on the STEM image.

However, for the dislocation detection by CNNs, there are other criteria for the quality of the image, which are hard to predict for microscopy users.

To quantify different diffraction conditions and be able to choose the ones preferable for the UNet detection network, a series of experiments were performed with various values for the excitation  $s_g$ -errors on the same dislocation network in TiAl alloy. The sample was oriented to a two-beam diffraction condition with excited diffraction vector  $\mathbf{g}=(002)$  using a double tilt rotation holder from Gatan Inc., model 925. By applying tilt in  $\alpha$ -direction it was possible to

vary the value of  $s_g$ . Fig. 5.4 depicts the aligned STEM images of dislocations acquired with different values of the excitation error (a) and corresponding segmentation results from the pre-trained UNet neural network (b). By comparing the segmentations to the manually labeled ground-truth image (c) it was possible to compute the "topological" distances for connected components (H0) and independent cycles (H1) for each filtration applied (d). The first two rows in the matrices (d) represent topological distances for dilation and density filtrations correspondingly, the next four rows are the height filtration with various vectors' directions with norm=1, last nine rows are the results of a radial filtration with different centers' position and radii of the circles.

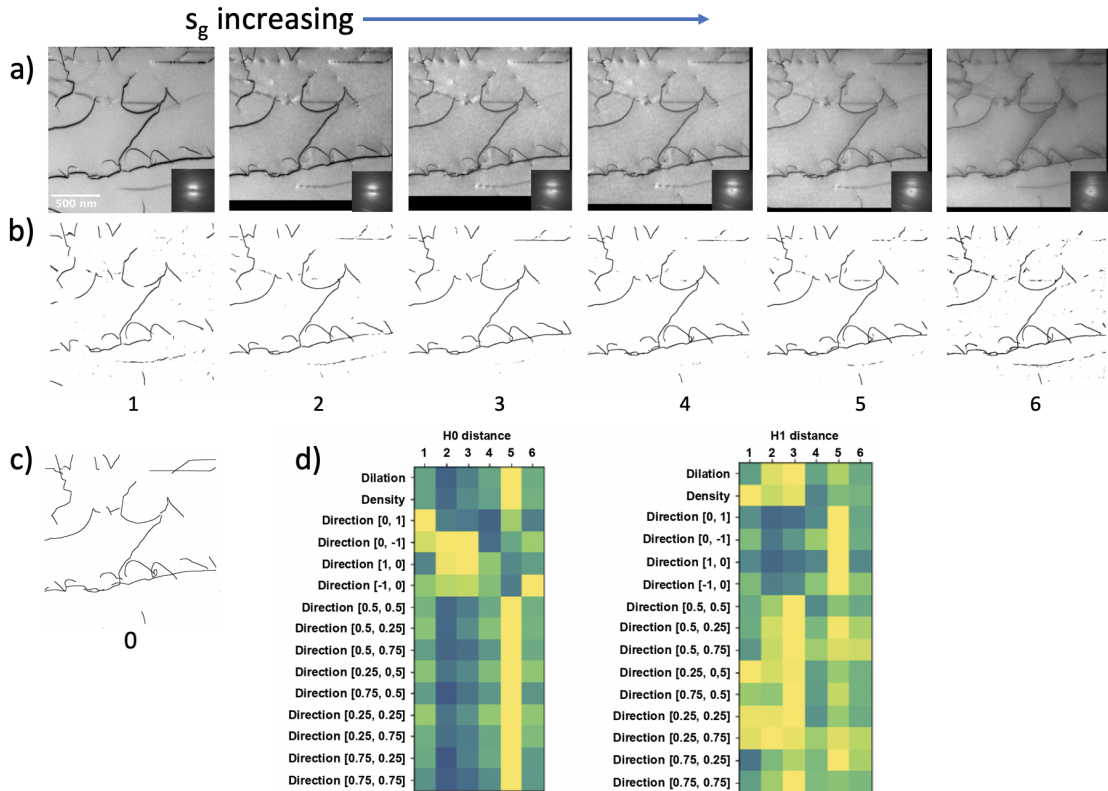


Figure 5.4: Quantification procedure of various  $s_g$ : (a) Aligned STEM images of dislocations in TiAl alloy acquired with different values of  $s_g$  and their corresponding diffraction patterns in two-beam diffraction condition, (b) Segmentation results from the pre-trained UNet neural network, (c) Manually annotated ground-truth, (d) TDA results representing "topological" distance for H0 and H1 for each filtration utilized.

To obtain the final topological score of the dataset and to define the diffraction condition with the highest topological correctness it is necessary to sum up all the scores for each filtration from Fig. 5.4 (d) separately for H0 and H1. ML algorithm assigned for each filtration particular weight or coefficient for the summation, so the error would be minimized compared to the ground-truth image. Fig. 5.5 demonstrates two matrices for H0 (a) and H1 (b) representing the scores for each filtration and corresponding weights and minimized errors obtained from

the ML algorithm. After summation of each score, it was possible to obtain a final topological score for the dataset acquired with various  $s_g$ . Image N.2 (highlighted with a red circle in (c)) in Fig. 5.5 with slightly positive  $s_g$  (with  $0.14^\circ$  of tilt from the exact Bragg two-beam diffraction condition) demonstrated the lowest value of the topological distance from the ground-truth, so the highest score.

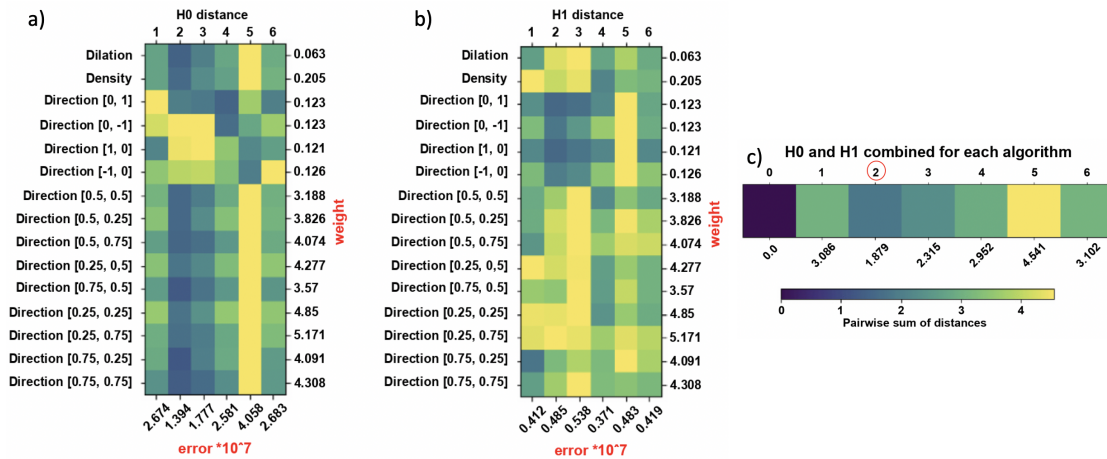


Figure 5.5: Final topological score calculation: (a) and (b) TDA results representing “topological” distance for H0 and H1 respectively for each filtration utilized with assigned weights and minimized errors, (c) Final scores with Image N.2 highlighted as the topologically closest to the ground-truth.

Topological scores obtained in Fig. 5.5 confirmed that for deep learning neural networks, as for the microscope user, the STEM images acquired with slightly positive  $s_g$  are the most preferred. However, one needs to be careful when applying a larger tilt from the exact Bragg diffraction condition. Results from topology analysis demonstrate that tilting the specimen for more than  $0.5^\circ$  from the exact Bragg diffraction condition causes the degradation of the quality of the STEM images and consequently, faults in the segmentations by the UNet network.

It is worth mentioning, that diffraction vector  $\mathbf{g}=(002)$  was chosen for STEM dislocation imaging of this material due to its shorter length compared to other  $\mathbf{g}$ -vectors. When imaging dislocations in STEM, a shorter  $\mathbf{g}$ -vector (i.e., a smaller scattering angle) is typically better because it allows for higher spatial resolution and better contrast. This is because the shorter  $\mathbf{g}$ -vector provides a larger scattering cross-section (i.e. the measure of the probability that electrons will scatter or interact with the sample), as a result, the scattered electrons have a larger probability of interacting with the atoms in the sample. This makes it easier to distinguish between the dislocation and the surrounding material. The shorter  $\mathbf{g}$ -vector also reduces the depth of field in the image, which means that the image will be more focused on the dislocation and less on the surrounding material. This can help to improve the contrast between the dislocation and the background, making it easier to identify and analyze it.

### 5.2.2 Detectors' collection semi-angle $\beta$

To obtain STEM imaging conditions that demonstrate uniform background and clean contrasts of dislocations and will be the most suitable for the following detection by UNet a series of experiments were performed varying the camera length (CL) of the microscope (the collection semi-angles  $\beta$  of the detectors as the function of CL is shown in Table 5.1). All BF-STEM images of dislocations were acquired with the same value of the convergence semi-angle, in particular, 12.8 mrad. When the value of CL is low, the signal from the transmitted disc is projected on a circular BF detector. When increasing the CL to a higher value, the transmitted disc starts to cover the annular HAADF detector, however, the center of the disc is not detected, due to the detector's ring shape. Fig. 5.6 shows one region of the TiAl alloy sample imaged with increasing values of the CL, corresponding segmentations by UNet are represented below. After some point, in particular, when the CL exceeds the value of 1100 mm the signal in the BF detector becomes too weak, capturing only the central part of the transmitted disc, so dominating detector capturing the signal for these collection angles becomes the annular HAADF detector. As one can observe, STEM images acquired with different CLs demonstrate different contrasts of dislocations and noise levels. The segmentation network correspondingly reveals various qualities of the detection. TDA results demonstrated that for the BF detector, the highest score obtain the image N. 7, and for the annular HAADF detector image N. 14. So, utilization of these images for the following 3D matching and reconstruction procedure by 3D CNN will demonstrate a more precise and clear results.

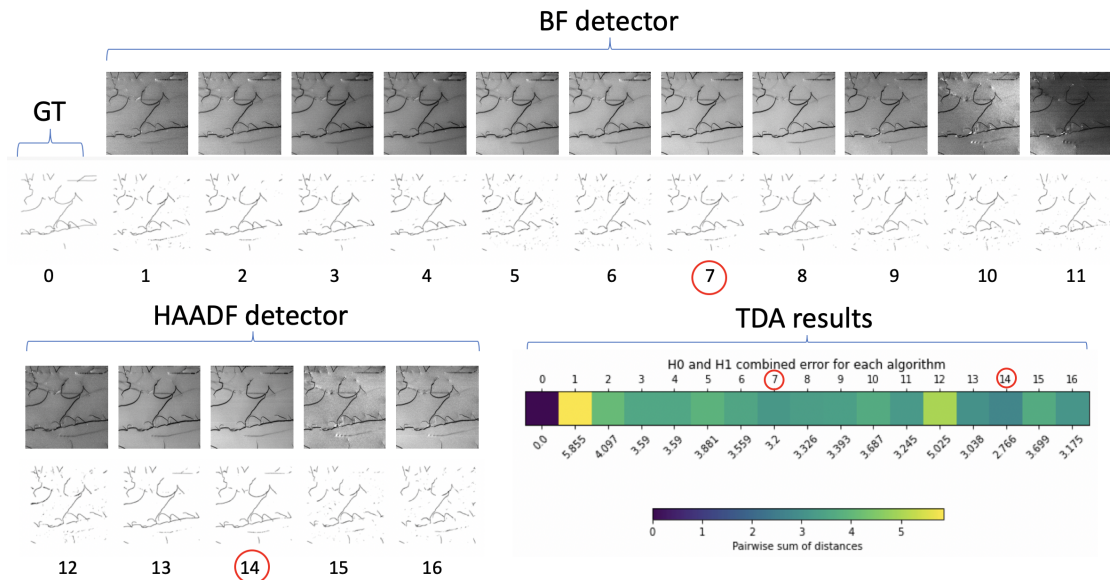


Figure 5.6: Quantification of the various detector's collections angles  $\beta$ , as a function of CL: Image N.0 - manually labeled ground-truth (GT), BF-STEM images of dislocations N.1-11 acquired on the BF detector, BF-STEM images of dislocations N.12-16 acquired on the HAADF detector, and corresponding detected dislocations from UNet neural network with TDA quantification results.

Detector	BF		HAADF		Image N.
Camera length, mm	$\beta_{in}$	$\beta_{out}$	$\beta_{in}$	$\beta_{out}$	
34	0	119			1
43	0	94.1			2
54	0	75.0			3
75	0	54.0			4
87	0	46.5			5
115	0	35.2			6
220	0	18.4			7
330	0	12.3			8
550	0	7.36			9
770	0	5.25			10
1100	0	3.7			11
1100			6.8	41.7	12
2100			3.4	20.8	13
3300			2.3	13.9	14
4300			1.7	10.6	15
5000			1.5	9.2	16

Table 5.1: BF and HAADF STEM detectors collection semi-angles  $\beta$  (in mrad) as a function of camera length for the sequence of images acquired in Fig. 5.6.

The highest topological score in Fig. 5.6 was obtained by the STEM images of dislocations acquired on a HAADF detector, in particular, with the values of CLs of 2100 and 3300 mm. In this case, the transmitted beam with 12.8 mrad convergence angle covers the HAADF detector (see values of the collection semi-angles of the HAADF detector  $\beta_{in}$  and  $\beta_{out}$  in Table 5.1), while the inner radius of the detector's hole is still small, the area where the signal is dropping out.

Overall, STEM images acquired on a HAADF detector obtained a higher topological score than the BF detector's images. One of the reasons for this may be the difference in the detectors' technology. HAADF detector (from Fischione Instruments) is a scintillator-type detector that

incorporates a single crystal yttrium aluminum perovskite (YAP) optically coupled to a photomultiplier tube. When high-energy electrons strike the scintillator material, they excite the atoms within the material, causing them to emit photons through a process called scintillation. The emitted photons are then detected by a photomultiplier tube, which produces an electrical signal proportional to the number of photons detected. This signal is then processed to form an image of the sample being imaged. The BF detector is a solid-state detector (from ThermoFisher). Solid-state STEM detectors work by utilizing semiconducting materials such as silicon, which can detect incident electrons and generate electrical signals in response. When an electron strikes the detector, it creates an electron-hole pair in the semiconductor material. This generates a current that can be measured and used to form an image. While the choice between a scintillator or a solid-state detector depends on the specific application and imaging requirements, scintillator detectors are typically more sensitive and have a higher dynamic range compared to solid-state detectors. Due to this BF-STEM images acquired on a HAADF detector at larger values of CL gained a higher topological score in comparison to the BF-STEM images acquired on a BF detector with lower CLs, even if the signal from the center of the transmitted disc is dropped out when imaging dislocations on a HAADF detector.

When performing experiments with various values of the CLs, STEM images were acquired with other detectors being retracted. It is a necessary condition in order to avoid the shadowing of the signal.

### 5.2.3 Pixel size and time

UNet segmentation results also were quantified relative to the STEM images' pixel sizes and dwell times. These parameters play an important role in the procedure of STEM imaging of dislocations.

Pixel size determines the spatial resolution of the image. The smaller the pixel size, the higher the spatial resolution and it allows for better visualization of the dislocation structure. However, utilization of a too-small pixel size can lead to a decrease in the signal-to-noise ratio and more noise in the image. This can make it difficult to distinguish between the dislocation contrast and the background noise, which can cause inaccurate measurements and a high noise level in the outputs of the segmentation UNet network. Another limitation of using a small pixel size is that it increases the acquisition time required to acquire a STEM image. Therefore, while a small pixel size is necessary to achieve high spatial resolution and accurately measure the properties of dislocations, it is important to find a balance between the spatial resolution, signal-to-noise ratio, acquisition time, and signal level to optimize the quality of the STEM image.

When it comes to the selection of the dwell time for the STEM image acquisition, microscope users need to make a decision based on the specific needs of the experiment. Long dwell times come with advantages such as higher quality of the STEM images and improved signal-to-noise ratio. However, it can cause beam damage to the sample during a long acquisition



time and also increases the likelihood of drift and vibrations during image acquisition, which can result in blurry or distorted images.

To choose optimal parameters for the UNet neural network segmentation various values of the pixel size and dwell time were tested. STEM images of dislocations were acquired from the same region in the TiAl alloy on a BF detector with convergence semi-angle  $\alpha=12.8$  mrad and with CL=220mm which corresponds to the collection semi-angle  $\beta=18.4$  mrad.

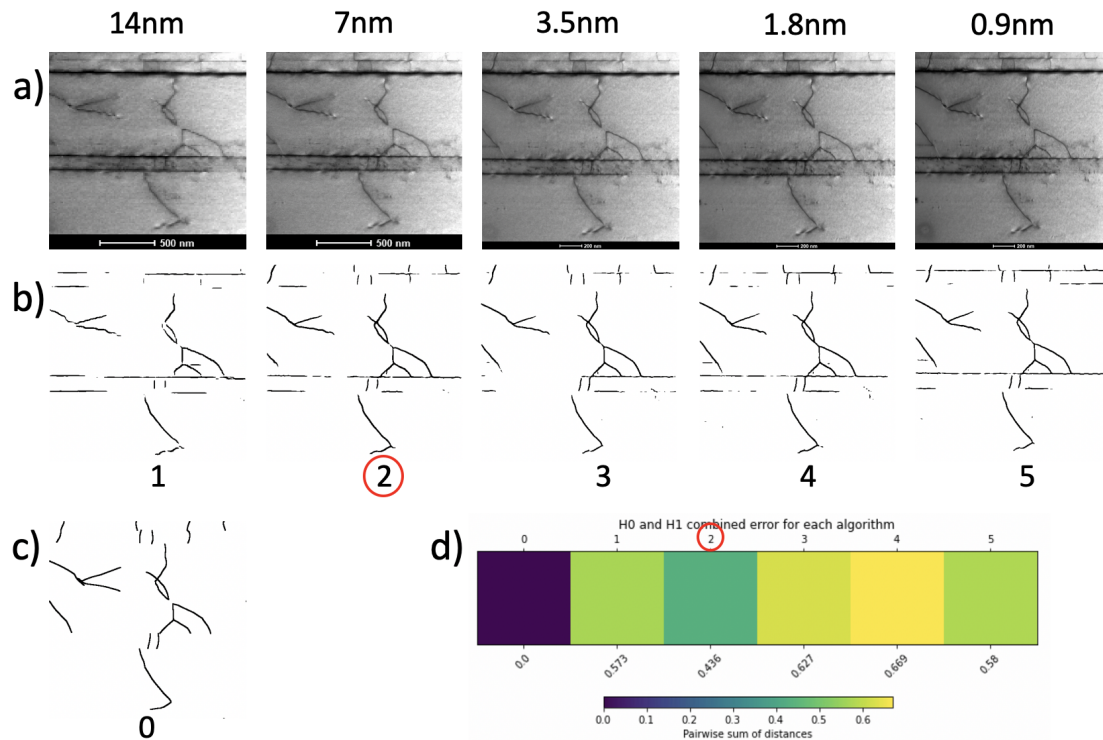


Figure 5.7: Quantification procedure of the STEM image's pixel size: (a) BF-STEM images of dislocations in TiAl alloy acquired with different values of the pixel size, (b) corresponding segmentations from UNet neural network, (c) manually labeled ground-truth, (d) TDA quantification results.

Fig. 5.7 shows the STEM images acquired on a BF detector with five different values of the pixel size (a), corresponding segmentations by UNet (b), and manually labeled ground-truth (c). All STEM images in Fig. 5.7 (a) were acquired with the same value of the dwell time  $4\mu\text{s}$ . TDA analysis results (d) show that the image with a pixel size of 7 nm obtained the highest topological score (i.e. the lowest topological distance to the ground-truth image). Image resolution was changed by gradually applying a binning to the  $2048 \times 2048$  resolution image (N.5 in Fig. 5.7) while preserving the constant magnification.

STEM images with various pixel sizes were acquired on a microscope without aberration correction. In a non-corrected STEM, the spatial resolution is typically limited by the spherical aberration of the probe-forming optics. As mentioned before, the choice of pixel size can

affect the signal-to-noise ratio of the image. Therefore, a reasonable choice of pixel size for imaging in a non-corrected STEM might be in the range of larger nm per pixel values. This condition explains the high topological score for the STEM image with a 7 nm pixel size.

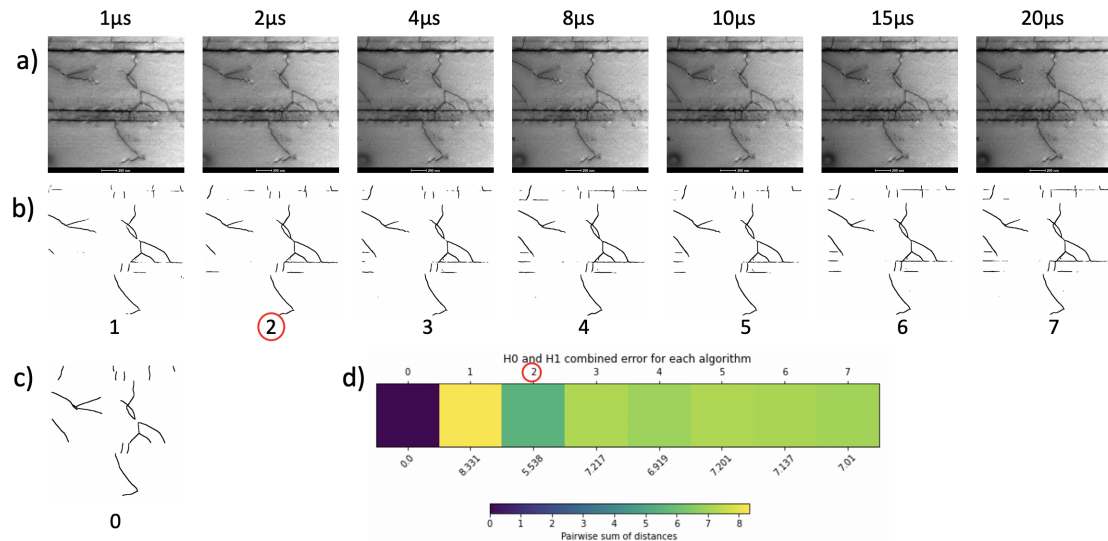


Figure 5.8: Quantification procedure of the STEM image's dwell time: (a) BF-STEM images of dislocations in TiAl alloy acquired with different values of the dwell times, (b) corresponding segmentations from UNet neural network, (c) manually labeled ground-truth, (d) TDA quantification results.

Fig. 5.8 represents the quantification procedure of the UNet outputs (b) from BF-STEM images acquired with five different dwell times (a) while preserving the constant pixel size of 3.5 nm. By comparing the segmentations (b) to manually labeled ground-truth image (c) utilizing the TDA technique, it was possible to select the optimal value of dwell time for these experiments (e). Image with  $2\mu\text{s}$  dwell time demonstrated the highest proximity to the ground-truth. However, all sequences of the STEM images acquired with a dwell time of  $2\mu\text{s}$  and more demonstrate a high degree of similarity, and correspondingly, the quality of segmentation by UNet does not vary a lot. This shows the robustness of the neural network to the noise in the STEM images and allows to invest less time in the acquisition process while maintaining good quality of the outputs.

### 5.3 Quantification of the results from segmented detector

In order to select the optimal STEM imaging conditions for single-shot dislocation imaging on a segmented detector, that also demonstrates the highest level of performance for following 3D reconstruction with neural networks, a few STEM imaging parameters were tested: detector inner collection angles as a function of CL, various pixel sizes and times. All experiments were performed on a Titan-Themis Cs-corrected microscope with 28 mrad of convergence semi-angle for the electron probe.



### 5.3.1 $\beta_{in}$

As mentioned in the previous chapter of the thesis dedicated to the tilt-less single-shot 3D imaging with the segmented detector, there is a trade-off between the value of the stereo-angle in STEM images acquired from the opposite segments and signal-to-noise ratio. Due to the annular shape of the segmented detector, the signal from the center of the transmitted disc is not detected, and when the CL is significantly lower than 115mm, the corresponding radius of the inner hole of the detector is increasing, allowing the segments to detect only the thin region around the rim of the transmitted disc, hence the signal-to-noise ratio in the STEM images is decreasing. However, this condition gives the highest value of stereo-angle between the STEM images from two opposite segments. The challenge is the selection of the optimum value of the detector's inner collection semi-angle  $\beta_{in}$  that delivers a larger stereo-angle while maintaining a good quality of the dislocation images, and therefore works the best with our 3D reconstruction pipeline. To choose the optimum value of  $\beta_{in}$  STEM stereo-pairs were acquired with three different values of the camera length. STEM images from segment C were used for the detection of dislocations by the UNet neural network and for the following topological analysis.

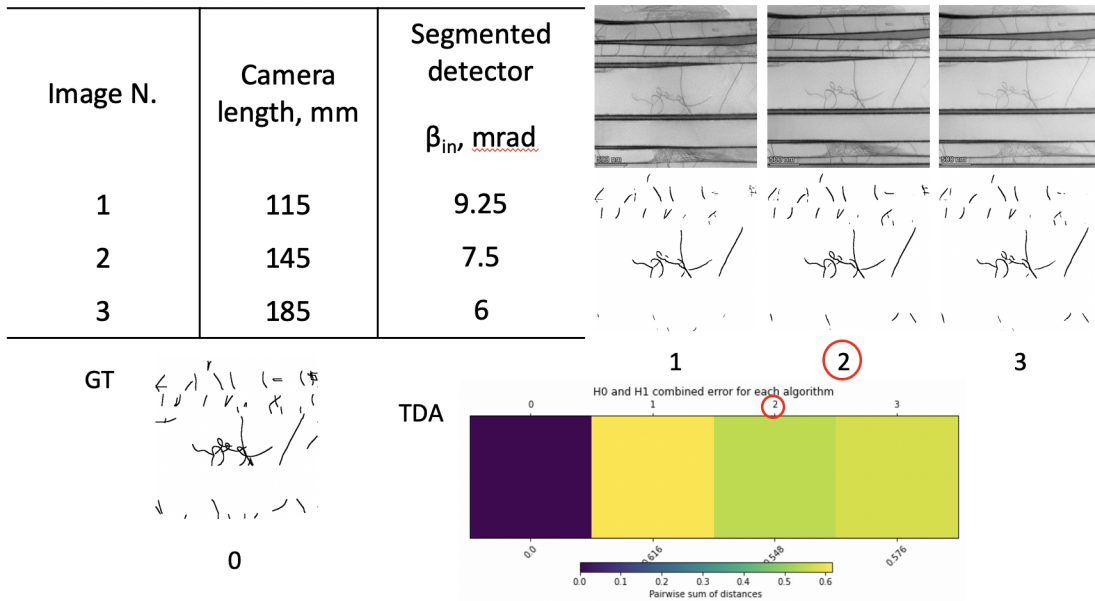


Figure 5.9: Quantification procedure of the BF-STEM images acquired on a segmented detector with three different values of  $\beta_{in}$  as a function of CL: TDA results demonstrate that image N.2 obtained the highest topological score and proximity to the ground-truth (GT) image.

Fig. 5.9 shows aligned STEM images of dislocations in TiAl sample acquired on a segmented detector (segment C) with three different values of CL, corresponding segmentations by pre-trained UNet neural network were compared after to the manually labeled ground-truth. The table in Fig. 5.9 demonstrates the relationship between CL and  $\beta_{in}$  values of the segmented detector. As it can be seen from the TDA results, the STEM image acquired with a CL value

of 145 mm, corresponding to segmented detector's inner radius  $\beta_{in}$  of 7.5 mrad, shows the highest topological score among the others. All STEM images of dislocations in TiAl alloy for this experiment were acquired on the segmented detector with the same value of the pixel's size at 1.3nm and  $10\mu\text{s}$  of dwell time, using convergence semi-angle  $\alpha=28$  mrad.

### 5.3.2 Pixel size and time

To select the optimal values of the dwell time for BF-STEM image acquisition on a segmented detector, the same dislocation network in TiAl alloy was imaged with three different values of dwell time while preserving the same value of a pixel size at 2.7nm, see Fig. 5.10 (a). TDA results (d) demonstrated that the STEM image acquired with  $8\mu\text{s}$  dwell time is the closest to the manually labeled ground-truth image (c).

For the quantification of the STEM images acquired on a segmented detector, one image from the stereo-pair was used, precisely, the STEM image of dislocations from segment C. In this case, longer dwell times are required to obtain STEM image and segmentation with the higher proximity to the ground-truth image, compared to the circular BF detector in section 5.2.3. This is due to the fact that each segment of the detector is recording a small part of the transmitted disc introducing noise that degrades the quality of the image, so longer dwell times are improving the signal-to-noise ratio. When acquiring a stereo-pair on a segmented detector dwell times of  $8\mu\text{s}$  and longer will provide the STEM images of dislocations and their segmentations with higher quality.

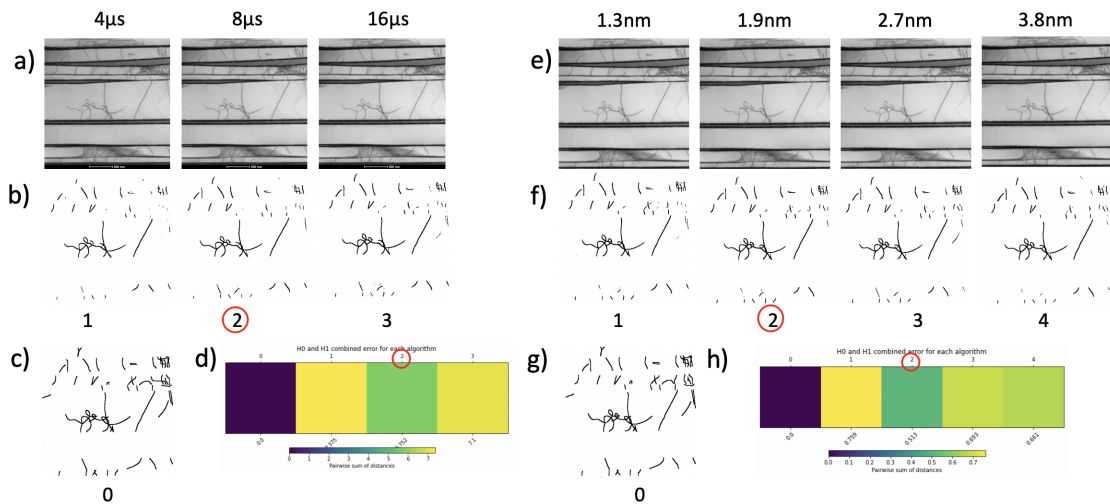


Figure 5.10: Quantification procedure of the BF-STEM images acquired on a segmented detector with different values of dwell time (a) and pixel size (e): after comparison of the corresponding segmentation images from UNet (b) and (f) to the manually labeled ground-truth images (c) and (g), TDA results demonstrated that images with  $8\mu\text{s}$  of dwell time and 1.9nm of pixel size (highlighted by red circles in (d) and (h)) obtained the highest topological score to the ground-truth images.

Quantification of the four different pixel sizes was performed on the same dislocation network with a constant value of  $16\mu\text{s}$  dwell time, in Fig. 5.10 (e). The total topological score for this dataset (h) revealed that the STEM image with  $1.9\text{nm}$  of pixel size is the best for the UNet neural network.

The segmented detector is installed on a Cs-corrected microscope. Aberration correction techniques allow to improve the resolution of a STEM microscope and image quality to sub-angstrom levels. To take full advantage of the improved performance a smaller pixel size can be used while preserving a high signal-to-noise ratio on this type of machine. Due to this fact, STEM images with smaller pixel sizes obtained a higher topological score, in comparison to the images acquired on a non-corrected microscope in section 5.2.3.

## 5.4 Quantification of the results from pixelated detector

The acquisition of a 4D-STEM dataset on a pixelated detector (installed on a Cs-corrected Titan Themis microscope) and the following extraction of the stereo-images is a complex procedure. Imaging conditions of the 4D-STEM dataset can be divided into two categories: the ones, that can be tuned before the acquisition of the dataset by the microscope operator, and the others, that can be adjusted during the post-processing for the virtual BF-STEM stereo-images formation. Quantification of these imaging conditions will be performed correspondingly.

### 5.4.1 Pixel size and time

Before performing the acquisition of the 4D-STEM dataset on a pixelated detector microscope the user can select and adjust the following parameters: magnification (i.e. pixel size in real space), frame time (corresponds to the time required to acquire one frame of the 4D dataset), detector's collection angle as a function of CL and counting mode.

*Camera length.* Selection of the detector's collection angle as a function of CL was performed with the main criteria to obtain the largest size of the transmitted disc's projection on the detector and yet to fit it in the detector's borders. When the convergence semi-angle  $\alpha$  is equal to  $28\text{ mrad}$  (with condenser aperture  $C2=70\ \mu\text{m}$ ) the CL was chosen to be  $91\text{ mm}$ , when  $\alpha=60\text{ mrad}$  (for  $C2=150\ \mu\text{m}$ )  $CL=37\text{ mm}$ . Choosing these values of CL allowed mapping the projected transmitted beam with more pixels of the pixelated detector. This allowed a more precise selection of the "virtual" detector's regions in the post-processing and generation of a stereo-pair. Each pixel's size of the pixelated detector is  $55\ \mu\text{m}$ , and the total number of pixels is  $256\times 256$ .

*Counting mode.* Merlin Medipix3 pixelated detector is a direct electron detector (DED) that provides a few different options for the selection of the counting mode, for example,  $1\times 24\text{Bit}$ ,  $2\times 6\text{Bit}$ , or  $2\times 12\text{Bit}$ . Where the first number represents an option of choosing one or two simultaneous thresholds and the second number is the dynamic range. Overall, the choice

between different counting modes depends on the specific requirements of the experiment and the properties of the sample being studied. For example, the 1x24Bit counting mode provides the highest dynamic range, allowing for the detection of very low-intensity signals, however, it typically has a slower readout speed. On the other hand, the 2x12Bit counting mode provides a compromise between dynamic range and readout speed, allowing for faster data acquisition while still providing reasonable precision and sensitivity. For 4D-STEM imaging of dislocations in TiAl alloy, the 2x12Bit counting mode was the most favorable choice, so all datasets were acquired in this mode.

*Pixel size and time.* While CL and counting mode were fixed, quantification of the pixel size in real space and frame time was performed. Fig. 5.11 represents the results of the TDA analysis of these parameters. All images were acquired with convergence semi-angle  $\alpha=28$  mrad and CL=91mm.

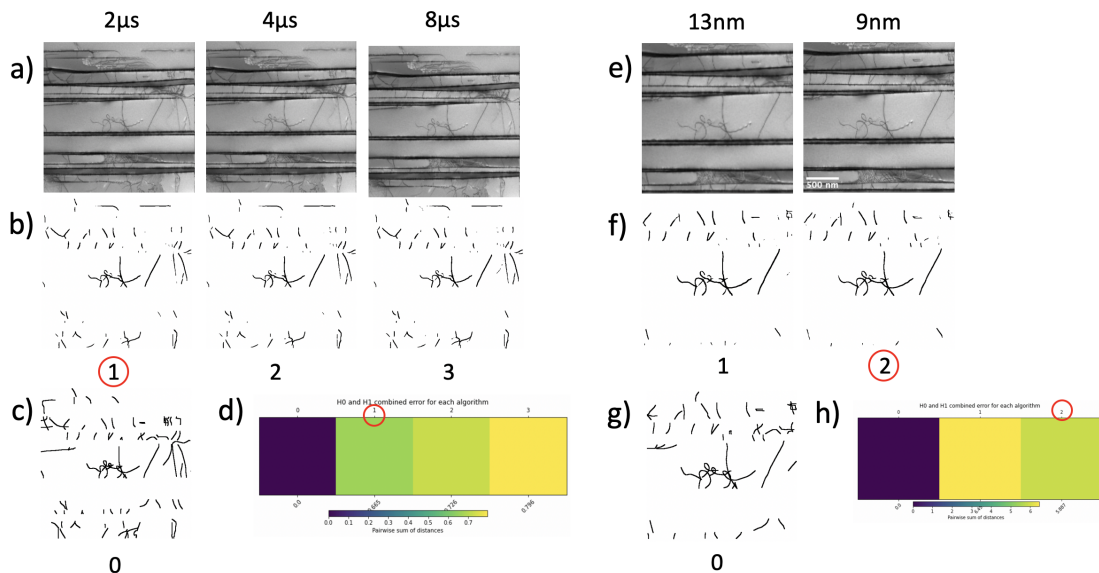


Figure 5.11: Quantification procedure of the virtual BF-STEM images of dislocations acquired on a pixelated detector with different dwell times (a) and pixel sizes (e): (b) and (f) corresponding segmentations from UNet neural network, (c) and (g) manually labeled ground-truth images, (d) and (h) TDA quantification results.

Firstly, virtual BF-STEM images of dislocations in TiAl alloy were acquired with various values of the frame time (a) while the pixel size was fixed to be 13 nm. TDA quantification results demonstrated that an image with  $2\mu\text{s}$  (highlighted with a red circle in (d)) is topologically closest to the manually labeled ground-truth (c). Longer frame time results in a considerably longer time required for the 4D dataset acquisition on a pixelated detector in comparison to conventional STEM detectors. This can cause electron damage and drift of the sample during the acquisition procedure, and finally, degrade the STEM image quality.

Secondly, the acquisition of dislocations virtual BF-STEM images on a pixelated detector was

performed with two different values of the pixel size. There is no binning option available for the acquisition of the 4D-STEM dataset on a pixelated detector, so the same dislocation network was acquired at two different magnifications, resulting in 13 and 9 nm pixel-sized STEM images in (e), with the same  $8\mu\text{s}$  frame time value. In this case, the highest topological proximity to the ground-truth (g) was obtained for the image with a smaller pixel size.

The 4D-STEM dataset acquired on a pixelated detector for these experiments contained  $256 \times 256$  pixels in real space and  $256 \times 256$  pixels in the reciprocal space. This creates a large number of frames in the final 4D dataset, correspondingly requiring a large amount of time to acquire it. To further decrease pixel size for the quantification experiments it is necessary to increase magnification on the sample or introduce a decrease in pixel size by enlarging the number of pixels with a smaller size in the real space. Magnification would change the field of view for topology analysis, so it is preferable to increase the number of pixels. However, the latter will considerably multiply the time required to obtain the 4D dataset. As shown before, it can cause degradation of the final virtual images due to sample drift, and damage induced by convergent electron beam.

#### 5.4.2 Radius of a "virtual" detector

The parameter, that can be tuned and then quantified during the post-processing of the 4D-STEM dataset is the radii of the "virtual" detectors for the formation of the virtual BF-STEM stereo-images. However, there is a trade-off between the signal-to-noise ratio and aberrations included in the formation of the stereo-images. On one side, when the radius of the detector is small, there is less signal for STEM image generation, which can lead to a high level of noise on the image. On the other side, increasing the radius of the "virtual" detector is including more aberrations at higher values of the convergence angles to the image formation. To select an optimum radius of the "virtual" STEM detectors for the creation of a stereo-pair of virtual BF-STEM images from the 4D-STEM dataset of the pixelated detector, various values of radii were quantified using the TDA tool. It is important for the quantification procedure to utilize the STEM images of the dislocation from the same viewing angle, i.e. tilt of the sample. For this purpose, the centers of the "virtual" detectors must be placed in identical locations on a pixelated detector during the STEM image creation in the post-processing.

Fig. 5.12 demonstrates virtual BF-STEM images of dislocations in TiAl alloy obtained from 4D-STEM dataset using different radii of "virtual" detectors (a), corresponding segmentations by pre-trained UNet neural network (b), manually labeled ground-truth (c), and TDA quantification results (d).

This 4D-STEM dataset was acquired using 2x12Bit counting mode,  $8\mu\text{s}$  of the frame time, and 4.32nm pixel size. The convergence semi-angle was set to the highest value available for this Cs-corrected microscope  $\alpha=91$  mrad, in order to test the effect of the aberrations on a virtual STEM image formation at large convergences of the electron beam. All images in Fig. 5.12 were obtained from the "virtual" detectors of various radii, but the same position of its

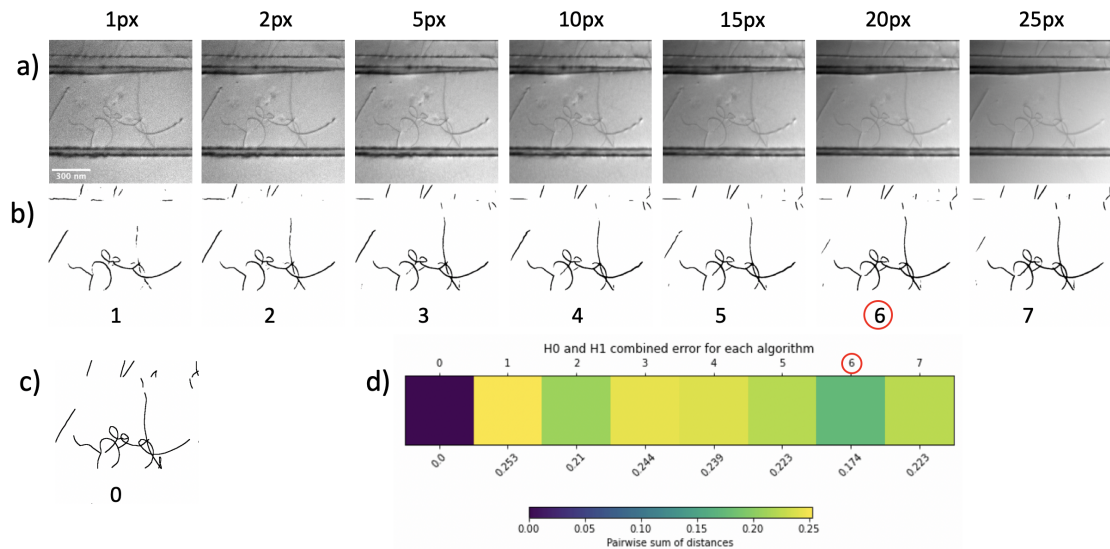


Figure 5.12: Quantification procedure of the virtual BF-STEM images acquired on a pixelated detector with different radii of the "virtual" detectors with centers at  $4.66^\circ$  of virtual tilt: (a) virtual BF-STEM images of dislocations in TiAl alloy obtained with different values of "virtual" detectors' radii, (b) corresponding segmentations from UNet neural network, (c) manually labeled ground-truth, (d) TDA quantification results.

centers, particularly at  $4.66^\circ$  of virtual tilt, from the rim of the transmitted beam disc, where distortions caused by aberrations are at their maximum. The "virtual" detector with a radius of 20 pixels, which corresponds to 15 mrad, obtained the highest topological score among other candidates. At this value, the signal-to-noise ratio is sufficiently high for the detection of dislocations by the neural network, and at the same time, the virtual BF-STEM image is not blurred due to the aberrations of the probe at the largest convergence semi-angle. On the other side, the virtual BF-STEM image formed from the "virtual" detector with 25 pixels in radius (image N.7) is highly distorted due to aberrations, hence dislocations are blurred, and corresponding segmentation is topologically further from the ground-truth image (c).

It is worth mentioning that at such high values of the convergence semi-angle when beam divergence is much larger than the Bragg angle, transmitted and diffracted beams are overlapped to a great extent. In particular, when imaging in two-beam diffraction condition, with diffraction vector  $\mathbf{g}=(002)$ , that is short, BF disc (000) and DF disc (002) are overlapped, so on the pixelated detector we observe the projection of a superposition of these two signals, also called Kossel pattern [82]. It has been demonstrated earlier that Kossel patterns, even with a high resemblance to the Kikuchi patterns, are dominated by elastic contrast [83]. So diffraction contrast from dislocations is preserved and still can be observed very well, despite the disc's overlap at high values of convergence semi-angle.

## 5.5 Concluding remarks

There are numerous STEM imaging parameters tunable by the microscope user that can influence dislocation image contrast. However, when performing following post-processing or 3D reconstruction by deep learning neural networks, it is hard to predict for the user the network's preferences in terms of what imaging conditions to select. In this chapter, a systematic investigation was performed by acquiring STEM images of the same dislocation network under different imaging conditions and systematically addressed the quality of the UNet segmentation by comparing it to a manually annotated set of images (ground-truth). It allowed not only to perform a visual selection of the favorable image conditions but also a quantitative way by utilization of the TDA tool.

Despite the fact, that it relies on the correctness of human annotations, TDA in combination with machine learning is a powerful approach for image classification and optimization of numerous STEM imaging parameters. It was possible to perform a quantification of the UNet neural network outputs obtained from the STEM images of dislocations acquired on BE, HAADF, segmented, and pixelated detectors. The optimal pixel sizes and dwell times were defined for all detectors in the non-corrected and Cs-corrected microscopes, an important parameter for STEM imaging. Derived parameters are close to the microscope user expectations, and utilization of them for the STEM image acquisition allows to obtain higher quality segmentations by UNet and, as a result, more precise 3D reconstructions by 3D CNN.

TDA results also demonstrated that the pre-trained UNet neural network is robust to the noise level on the images, so shorter dwell times can be used for the STEM image acquisition while maintaining a good quality of the segmentation results. This allows to significantly reduce the time required for imaging experiments, which is especially important for 4D-STEM dataset acquisition on a pixelated detector, and for specimens that are sensitive to the electron beam.

## 6 3D distribution of nanoparticles

This chapter is devoted to the analysis of the 3D distribution of nanoparticles in a solution from a single sample tilt in order to obtain information on their interaction potential. The tilt-less 3D imaging technique was applied to perform 3D cryo-STEM imaging of nanoparticles in vitrified ice on segmented and pixelated detectors. A classical computer vision approach was developed in collaboration with the CVLab at EPFL to obtain the 3D reconstruction of the nanoparticles in the sample for the following radial distribution analysis.

The sample was supplied by the SuNMIL laboratory at EPFL, which also provided support for cryo-microscopy.

### 6.1 Introduction

Nanoparticles are increasingly used in medicine due to their unique physical and chemical properties, which make them ideal for drug delivery, imaging, and diagnosis. In particular, gold nanoparticles due to their stability and compatibility with biological tissues have found many potential applications in nanomedicine [84], [85]. Nanoparticles have been extensively studied as a drug delivery system due to their small size, which allows them to penetrate deep into tissues and cells, and their large surface area, which provides a high drug-loading capacity. They can be used to deliver drugs to specific sites in the body, such as tumors while minimizing the side effects associated with conventional drug delivery methods. By functionalizing nanoparticles with specific ligands, the properties and behavior of the nanoparticles can be tailored to specific applications. In the drug delivery example, functionalizing the nanoparticles with targeting ligands that allow them to selectively accumulate at the target site. Nanoparticles also can be used to develop highly sensitive diagnostic assays that detect disease-specific biomarkers in body fluids, and also in medical imaging as contrast agents [86].

It is essential therefore to study the properties of nanoparticles to characterize their behavior and interactions in a colloidal solution. Calculation of radial distribution function (RDF)  $g(r)$



provides information on the spatial distribution of nanoparticles in a solution which can help to determine if they are forming aggregates or if they are well-dispersed. This information can provide insights into the properties of the particles and their potential applications. Additionally, RDF can be used to monitor the stability of nanoparticles over time and to study important thermodynamic properties.

Recently, cryo electron tomography (cryoET) has found many applications in the investigation of the protein's structures and other biological specimens, thanks to the development of direct electron detectors. This technique applied in TEM mode recently received the Nobel prize for its development [87].

CryoET was also applied to a vitrified dispersion of nanoparticles in solvents in a TEM imaging mode to study their thermodynamic properties [88]. It has been demonstrated that from the center-of-mass position of nanoparticles extracted from the tomogram, the  $g(r)$  function and the potential of mean force (PMF)  $U(r)$  between nanoparticles can be calculated directly without any assumption.

However, the acquisition of one tilt-series for tomographic reconstruction requires long imaging and post-processing times. In order to achieve statistical significance the same imaging procedure followed by tomographic reconstruction needs to be repeated many times in different regions of the specimen. In general, a larger sample size will increase the statistical power of the analysis and reduce the margin of error. However, imaging a large number of nanoparticles by means of electron tomography is time-consuming.

Recently STEM imaging was successfully applied to study protein structures in a cryo-condition utilizing the integrated differential phase contrast mode (iDPC-STEM) [89]. It was demonstrated that STEM mode applied to vitrified biological samples allows to resolve structures of molecules at near-atomic resolution.

In this Chapter, tilt-less 3D imaging in STEM mode will be applied to study nanoparticles in a vitrified solution. This novel approach will considerably decrease the time of the experiment compared to electron tomography 3D reconstruction techniques recently utilized in the field and offer the opportunity to perform statistical analysis in a significantly shorter time. This methodology can also pave the way for studying the interaction of the particles in liquid in real time.

## 6.2 Material system and sample preparation

The studied system are gold nanoparticles with a diameter  $< 5\text{nm}$ . Nanoparticles were coated with various types of ligands and their dispersions in solvents are further analyzed in cryo-condition. For detailed information on nanoparticles' synthesis procedure see [88]. Solutions with different levels of dilution are used for cryogenic electron tomography and tilt-less 3D imaging.

Sample preparation for cryo-imaging at  $-170^{\circ}\text{C}$  included the application of the four microliters of dispersion onto a quantifoil grid (200 mesh, EMS). Then the solution was blotted on one side of the grid using a Whatman filter paper (1440-090) and immediately vitrified in liquid ethane with a manual plunge freezing apparatus. The vitrified sample then was transferred to a cryo-specimen holder Gatan 626 (Warrendale, PA, USA) for the following electron imaging.

### 6.3 Cryo-STEM 3D imaging with segmented detector

The tilt-less 3D cryo-STEM imaging was performed using an annular detector with four segments on the Themis Titan microscope operating in STEM mode at 300kV. The convergence semi-angle  $\alpha$  of the electron probe was set to 28 mrad. The transmitted disc was carefully centered around the hole of the detector so that it evenly covers segments A, B, C, and D, see Fig. 6.1 for the schematic illustration of the single-shot tilt-less 3D imaging of nanoparticles in vitrified ice. STEM imaging of the samples in cryo-condition requires careful adjustment of the microscope and imaging parameters due to their sensitivity to electron radiation. Crystallization, the melting of the ice can occur under the high-energy convergent electron beam. In order to select conditions that don't provoke damage in the specimen and provide STEM images with high quality and resolution, different imaging conditions were tested, in particular, dwell time and current value in the electron beam. After examination of various values of the electron current registered on the fluorescent screen, the current was set to 0.1 nA. This value allowed obtaining high-quality STEM images of nanoparticles with a high signal-to-noise ratio while ensuring the stability of the vitrified ice. The nanoparticles in vitrified ice were imaged with 2048x2048 pixels resolution with each pixel 0.4 nm in size, dwell time was set to  $10\mu\text{s}$ . These imaging conditions allowed to acquire simultaneously four BF-STEM images of nanoparticles in one minute with high quality, preventing electron damage to the sample.

Four BF-STEM images acquired on a segmented detector via single-shot from corresponding segments A, B, C, and D can be seen in Fig. 6.1. The stereo-angles between each pair of images (A-C and B-D) are approximately 3 degrees. Due to the absence of the diffraction contrast in this case, all four images reveal comparable background and nanoparticles' contrast and can be used for the following 3D reconstruction and calculation of the nanoparticles' positions in the volume of the sample, i.e. in a vitrified solution.

The STEM images that can be observed in Fig. 6.1 are acquired from the sample with a concentration of 10 mg/ml of nanoparticles, that are distributed evenly in the solution without agglomerate formation.

### 6.4 Detection and 3D reconstruction

In order to perform the 3D reconstruction of the nanoparticles from four BF-STEM images acquired on a segmented detector a classical computer vision approach was used. Classical computer vision (CV) utilizes traditional methods of image processing and analysis, that

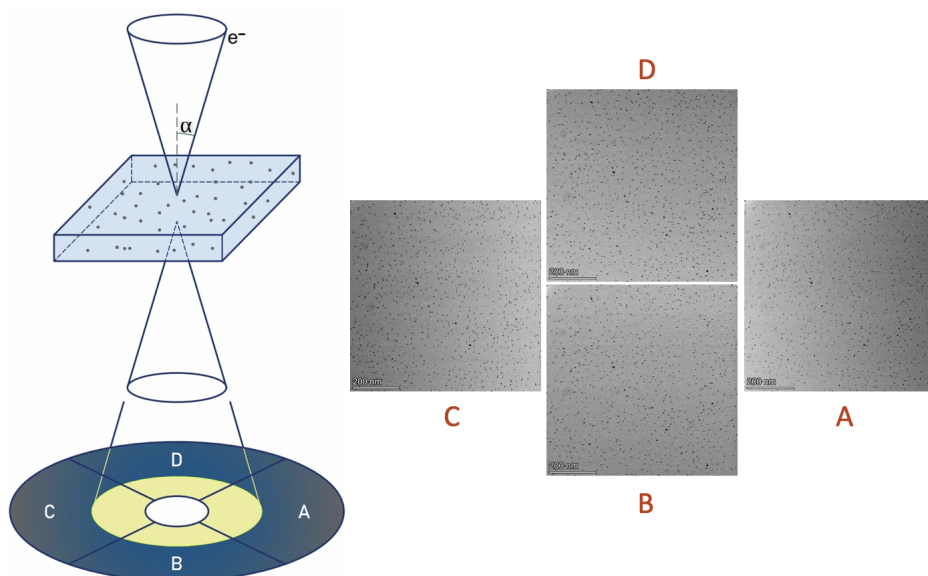


Figure 6.1: Schematic illustration of the single-shot 3D tilt-less imaging of nanoparticles in vitrified ice with the segmented detector with four BF-STEM images acquired simultaneously from segments A, B, C, and D.

include algorithms and mathematical models. These methods often involve pre-processing of images, such as filtering or thresholding, followed by feature extraction using methods like edge detection, corner detection, or texture analysis. On the other hand, modern computer vision relies on deep learning techniques, for example, deep learning CNNs that are used to learn features directly from raw image data. For these experiments, the classical computer vision approach is used due to the simple geometrical form of the reconstructed features, and classical algorithms have proven to be effective. The advantage of the classical technique over deep learning is also that they do not require annotating a large number of images to create training data.

Fig. 6.2 depicts the 3D reconstruction pipeline for measuring the 3D depth of nanoparticles in the sample. Due to the absence of mechanical tilt during the acquisition of different images, there's no necessity to perform an alignment procedure for the STEM images acquired on a segmented detector, so it is possible to directly input them from the microscope to the developed classical CV algorithm.

A description of each post-processing step from our 3D reconstruction pipeline will be given below.

#### 6.4.1 Denoising

In the first step, four raw BF-STEM images are simultaneously denoised using a Gaussian blur filter. This filter is designed to blur the image by averaging the values of neighboring pixels,

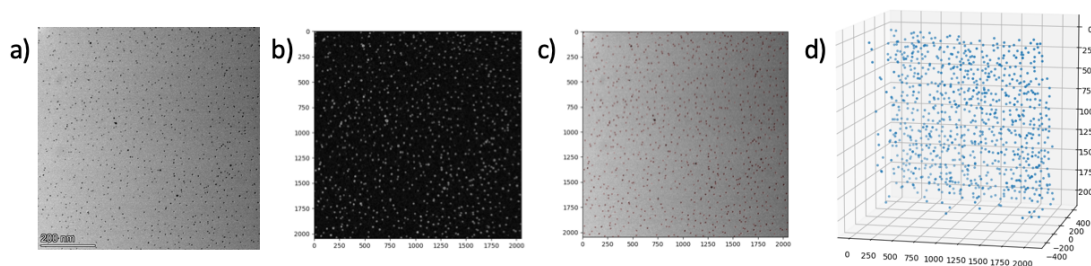


Figure 6.2: 3D reconstruction pipeline of nanoparticles imaged on a segmented detector: (a) An example of BF-STEM image (from the segment A), (b) Result of the edge detection after denoising the image (a), (c) Detected nanoparticles highlighted by red circles, (d) Final 3D reconstruction after application of the steps (b) and (c) on all four images from segments A, B, C, and D (shown in Fig. 6.1).

and the amount of blurring is controlled by adjusting the standard deviation of the Gaussian distribution. High-frequency noise from the segmented detector was occasionally observed on the STEM images of nanoparticles. The Gaussian blur filter was therefore used to reduce the noise in the images while preserving the edges and details.

#### 6.4.2 Detection

Edge detection was performed in order to identify the boundaries between nanoparticles in an image. It is a fundamental step in image processing and computer vision and is used to extract meaningful information from the images while reducing noise and other irrelevant features. The process involves filtering an image to enhance the edges and then detecting the edges by looking for significant changes in brightness. For edge detection in BF-STEM images of nanoparticles a gradient-based method is used, namely the Sobel operator (from the OpenCV library). It works by computing the gradient of an image intensity function, which is a measure of how rapidly the image intensity changes in different directions. The Sobel operator approximates the gradient by computing a convolution of the image with a set of two kernels, one for the x-direction and one for the y-direction. These kernels consist of a small matrix of weights that represent the difference in intensity between neighboring pixels. By convolving the image with these kernels, the Sobel operator estimates the rate of change of the image intensity in the x and y directions. The result can be seen in Fig. 6.2 (b) representing the gradient of image A from the segmented detector, which then was used to identify the edges in the image. This operation is performed on all four STEM images of nanoparticles from the segmented detector.

After performing edge detection on four denoised STEM images the edge maps were obtained for each image. The edge map is then used to find the edge points, which are used as input to the Hough transform. It is a feature extraction technique in image analysis that is used to identify geometrical shapes, such as lines, circles, and ellipses. In order to detect the

projections of spherical nanoparticles on the STEM images the Hough transform is applied to find the parameters of the circles. Each edge point of the image is mapped to a parameter space, in which the x and y coordinates of the center of the circle are represented as two dimensions, while the radius of the circle is represented as a third dimension. The algorithm then searches for the maximum number of points in the parameter space that lie along the same circle. This is done by using a voting process, in which a vote is submitted for every possible circle that could pass through each edge point. The circle with the most votes is then identified as the most likely circle in the image. Finally, a threshold value is applied to filter out circles with fewer votes than the threshold. The remaining circles are then returned as the detected circles in the image. Fig. 6.2 (c) represents the detected circles (in red color) drawn on the original STEM image from segment A of nanoparticles.

### 6.4.3 3D reconstruction

After performing the Hough circle detection on all four STEM images acquired respectively from segments A, B, C, and D of the detector, nanoparticles were reconstructed in the 3D volume of the sample. 3D reconstruction was performed by using the modified version of the stereo matching procedure taking into account the particularities of the detector's geometry and the number of images.

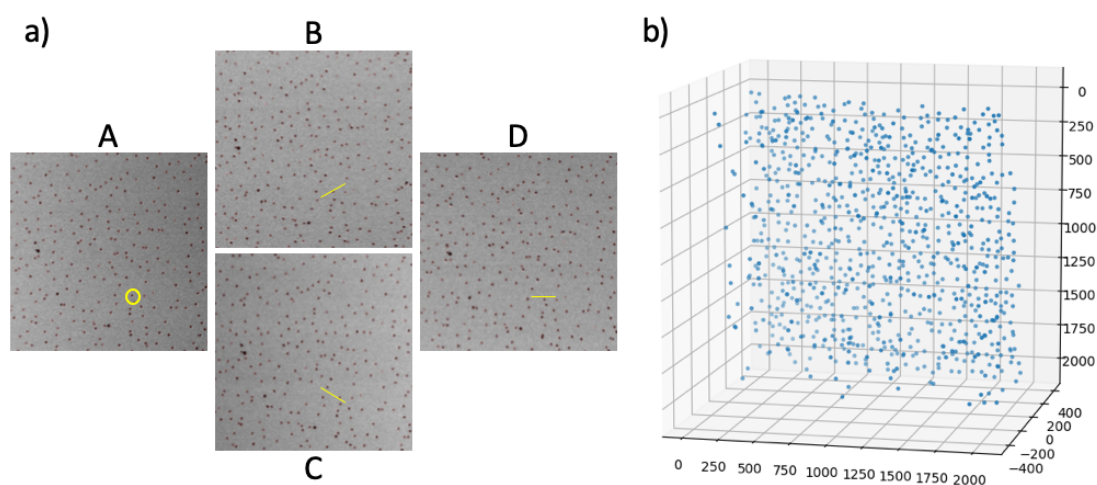


Figure 6.3: 3D reconstruction of nanoparticles in vitrified ice: (a) STEM images from A, B, C, and D regions of the segmented detector (shown clockwise) with detected particles shown in red circles. For a chosen particle in region A (depicted in a yellow circle), correspondences are searched on line segments shown as yellow lines in B, C, and D images. (b) If consistent detections are found in all 4 images, a suitable depth value is assigned to the particle.

Fig. 6.3 demonstrates the 3D reconstruction pipeline from detected nanoparticles (highlighted with red circles in (a)). For a selected nanoparticle in image A (spotlighted by a yellow circle), the algorithm is searching for a corresponding nanoparticle on line segments shown as yellow

lines in images B, C, and D. Due to the detector's geometry line segments on images B and C are  $45^\circ$  inclined with respect to the line segments on the images acquired from segments A and D. When the search algorithm finds consistent detections in all four images the value of a stereo-shifts on the lines are calculated, it is assigned then to the nanoparticle as its depth. To obtain the final 3D reconstruction of the detected nanoparticles triangulation was conducted with the corresponding depth value for each nanoparticle and with  $3^\circ$  of stereo-angle, see Fig. 6.3 (b).

The proposed method for defining the 3D distribution of nanoparticles in a vitrified solution delivered promising results. After visual analysis of the circle detection results, it was determined that only a few nanoparticles were not present, and the total number of detected nanoparticles in the STEM image from segment A was 1324. Only when the search algorithm finds correspondences in the other three images for a reference nanoparticle in the image from segment A, it can be reconstructed in 3D. The final 3D reconstruction contained 1304 nanoparticles, so only 20 nanoparticles did not have corresponding candidates for stereo matching, causing it to be less than 2% of missing nanoparticles.

## 6.5 Radial distribution analysis

As mentioned in the introduction to this chapter, it is important to understand the nanoparticles' behavior and interactions. Calculation of the radial distribution function  $g(r)$  is crucial in comprehending the structural properties of nanoparticles in a solution. It involves measuring the distribution of distances between particles as a function of their separation distance from a central point.

To calculate  $g(r)$  a Python code from [90] was used. As input the 3D coordinate of each nanoparticle needs to be introduced to in the code. The extraction of the 3D coordinates (x, y, z) of the nanoparticles was performed from the 3D reconstruction obtained in Fig. 6.3 (b). 3D coordinates were extracted in pixel values, then converted to nm scale, with bin size 0.4, corresponding to the STEM image pixel size (0.4 nm). Fig. 6.4 shows the  $g(r)$  function calculated from the sample with 10 mg/ml concentration of nanoparticles.

The radial distribution function  $g(r)$  for nanoparticles in Fig. 6.4 represents the probability of finding a particle at a certain distance from a reference particle in a solution, where  $r$  is an interparticle distance. The result obtained corresponds to what is generally predicted from the specimen with a 10 mg/ml concentration: the first peak at a distance of 5.5 nm from the reference nanoparticle is observed, corresponding to the average interparticle distance. At higher distances, the function is approaching the value of 1, indicating that the nanoparticles are randomly distributed in a vitrified solution.

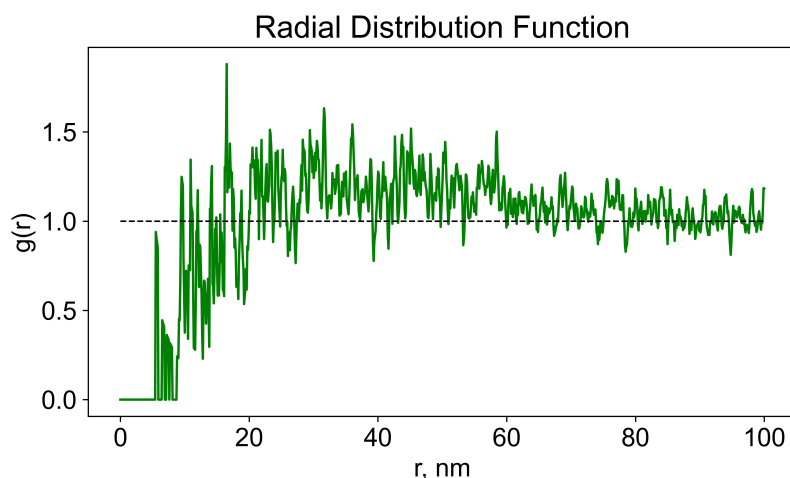


Figure 6.4: Radial distribution function  $g(r)$  of the nanoparticles in vitrified ice with 10mg/ml concentration obtained from the 3D reconstruction in Fig. 6.3 (b).

### 6.5.1 Comparison to tomography

In order to verify the performance of 3D imaging with the tilt-less 3D approach, the resulting reconstruction was compared to the tomographic 3D reconstruction that has served as a ground-truth. 3D imaging and comparison of the two radial distribution functions were done on a sample with a 10 mg/ml concentration of nanoparticles in a stable dispersion state.

Images of nanoparticles for tomographic reconstruction were acquired from the same region of the sample as in tilt-less 3D imaging. Firstly, tilt series were recorded on the Tecnai F20 microscope in TEM mode, then, the sample was transferred to the Titan Themis microscope for the tilt-less 3D imaging on the segmented detector. Tilt series were collected automatically with the microscope operating at 200kV. The vitrified sample was tilted from  $-60^\circ$  to  $+60^\circ$  and TEM images were recorded every  $2^\circ$  on a Falcon III camera (Thermo Fisher) with  $4096 \times 4096$  pixels with approximately the same value of the pixel size as in the tilt-less technique of 0.4nm. During the acquisition process, the data was drift corrected by Tomo 4.0 (Thermo Fisher) software. For tomographic reconstruction, images of the tilt series were firstly cropped around the regions of interest, consisted of  $2664 \times 2664$  pixels, secondly aligned, then processed using the SIRT reconstruction technique (with 24 iterations).

The tomogram obtained consisted of 910 slices in a stack sectioning the sample in the direction of its depth. Then it was uploaded to a custom Python script in order to extract the 3D coordinates of each nanoparticle in the 3D volume of the sample for the following calculation of the radial distribution function  $g(r)$ .

Fig. 6.5 shows  $g(r)$  functions calculated from the two types of 3D reconstructions plotted together: the red one obtained from four BF-STEM images acquired via single-shot tilt-less 3D imaging in STEM on a segmented detector and the grey one obtained from the tomographic

reconstruction of the tilt series.

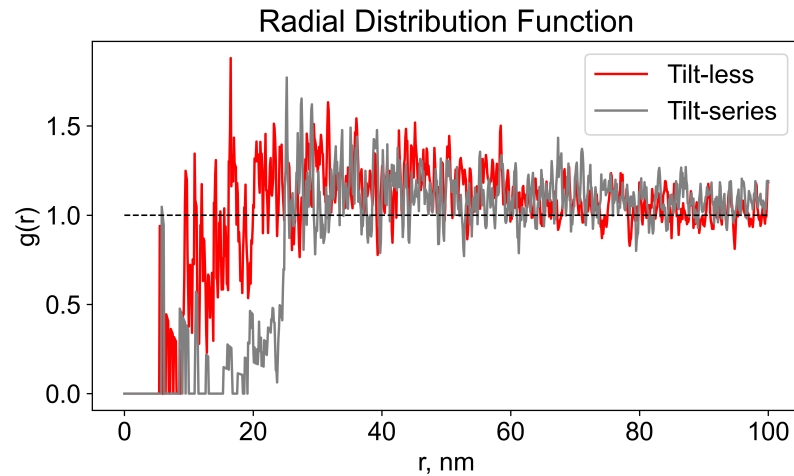


Figure 6.5: Radial distribution function  $g(r)$  of the nanoparticles in vitrified ice with 10mg/ml concentration obtained from the 3D reconstruction by 3D tilt-less imaging in STEM mode (with the stereo-angle of  $3^\circ$ ) and from the TEM tilt series.

As can be seen, the two  $g(r)$  functions exhibit a high degree of similarity. There is a good level of correlation at the larger values of interparticle distances. However, some divergences can be observed at smaller distances, for example, a small shift of the first peak. In the RDF function calculated from the tilt-less 3D reconstruction, the first peak is observed at 5.5 nm of interparticle distance, while for tomogram reconstruction is at 5.8 nm. This is something that may happen due to many factors. First of all, the field of view in the two microscopes was slightly different, and the number of nanoparticles used for 3D reconstruction. In particular, the images for tomographic reconstruction contained a higher number of pixels, and the final tomogram consisted of 1606 nanoparticles, whereas the 3D reconstruction obtained from four STEM images had 1304 nanoparticles. Secondly, the sample after acquisition of tilt series can be deformed due to the long exposure to the electron beam, and during the transfer to another microscope. Thirdly, there is no possibility to define precisely the tilt angle in the stereo-pairs acquired on a segmented detector, which can lead to uncertainties in the tilt-less 3D reconstruction.

To test the effect of the stereo-angle on the final 3D reconstruction and on  $g(r)$  function, the 3D reconstruction of nanoparticles was performed with different values of the stereo-angle which lies in the range from  $1.6^\circ$  to  $3.2^\circ$ . The smaller stereo-angle corresponds to the inner diameter of the detector collection angle at this value of the CL, and the largest stereo-angle corresponds to the maximum angle of the beam convergence projected on a segmented detector. The most proximity to the RDF of the tomogram obtained the tilt-less reconstructions with  $2.0^\circ$  and  $2.2^\circ$  of stereo-angle, with 6.0 and 5.9 nm interparticle distance respectively, where the first peak appears. However, their RDF demonstrated more disagreement with the RDF of tomogram at larger distances than 3D reconstruction with  $3.0^\circ$  of stereo-angle. The  $g(r)$  function of 3D



reconstruction with  $2.8^\circ$  of stereo-angle also provided similar results to the tomogram, with the first peak at 5.6 nm of interparticle distance and in good agreement at larger distances. So it was concluded that 3D reconstructions with  $2.8^\circ$  and  $3.0^\circ$  of stereo-angle are the closest to the tomogram.

Overall, the two  $g(r)$  functions obtained from tilt-less 3D reconstruction and conventional tomogram displayed a strong resemblance. This confirms that our tilt-less 3D reconstruction approach is valid and can be used as an alternative technique to conventional TEM tomography to obtain  $g(r)$  functions of nanoparticle systems.

## 6.6 Application to other samples

After confirmation of the results from the tilt-less 3D imaging approach, this technique was applied to study vitrified samples with a high concentration of nanoparticles. The method was applied as well to the challenging case of nanoparticles that forms agglomerates. STEM imaging conditions for the simultaneous acquisition of four images of the nanoparticles and the 3D reconstruction procedure remained the same as in the sections 6.3 and 6.4.

### 6.6.1 Sample with a high concentration of nanoparticles

A sample with a concentration of 40mg/ml of nanoparticles was prepared and imaged in cryo-condition in STEM mode on a segmented detector. Fig. 6.6 demonstrates an example of the BF-STEM image from segment A acquired on a segmented detector (a), corresponding 3D reconstruction from all four STEM images (b), RDF calculated from the 3D coordinates of nanoparticles in (b) can be observed in (c).

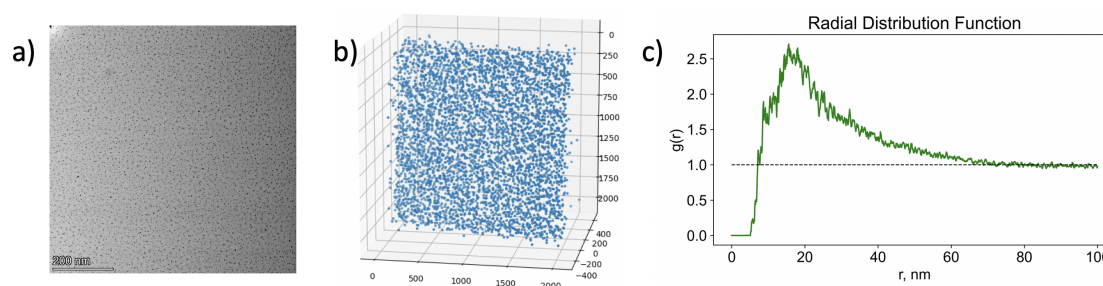


Figure 6.6: Radial distribution analysis of nanoparticles with a high concentration: (a) BF-STEM image of dispersed nanoparticles (segment A) in vitrified solution with 40mg/ml concentration, (b) 3D reconstruction using all four views by the 3D tilt-less imaging technique, (c) Radial distribution function  $g(r)$  of the nanoparticles.

The final 3D reconstruction in Fig. 6.6 consists of 4444 nanoparticles. It is worth mentioning, that the number of nanoparticles may strongly vary in the different regions of the same specimen, due to the thickness variations of the vitrified ice at different specimen locations.

The radial distribution function for nanoparticles with a high concentration in a solution shows a sharp peak at a small interparticle distance, in particular at 5.2 nm, indicating a high probability of finding a nanoparticle at that distance. This is because the high concentration of nanoparticles increases the probability of finding particles in close proximity to each other, resulting in more frequent interactions and a denser arrangement. Then  $g(r)$  function gradually decreases until it reaches a plateau at larger distances, indicating that the nanoparticles are randomly distributed in the solution.

### 6.6.2 Shortened nanoparticle agglomerates

The tilt-less 3D imaging and following radial distribution analysis were performed on a sample with a 10mg/ml concentration of nanoparticles forming agglomerates with reduced size (the length of each agglomerate contains 2-5 nanoparticles in a chain). Fig. 6.7 demonstrates an example of the BF-STEM image from segment A acquired on a segmented detector (a), corresponding 3D reconstruction from all four STEM images can be seen in (b) with 704 nanoparticles, RDA analysis results in (c).

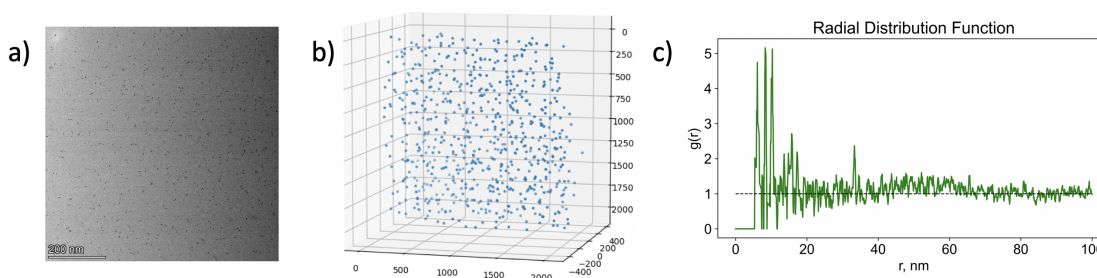


Figure 6.7: Radial distribution analysis of nanoparticles forming shortened agglomerates in a vitrified solution: (a) BF-STEM image of agglomerated nanoparticles (segment A) in vitrified solution with 10mg/ml concentration, (b) 3D reconstruction using all four views by the 3D tilt-less imaging technique, (c) Radial distribution function  $g(r)$  of the nanoparticles.

The specimens that are forming agglomerates were challenging for our detection algorithm, occasionally a small number of nanoparticles with high proximity to each other were not detected. This led to only 704 nanoparticles in the final 3D reconstruction.

The radial distribution function for nanoparticles that are forming short agglomerates shows the first peak at a 5.4 nm distance corresponding to the average distance between neighboring particles within the agglomerates. The distribution function also shows a decrease in intensity at larger distances, indicating the absence of any long-range ordering of the particles. Overall, despite the missing nanoparticles, the distribution function indicated short-range correlations due to the formation of small agglomerates.

### 6.6.3 Long nanoparticle agglomerates

Then the tilt-less 3D imaging and following radial distribution analysis were performed on a sample with a 10mg/ml concentration of nanoparticles forming long agglomerates (the length of this type of agglomerate can have more than 20 nanoparticles in a chain). Fig. 6.8 demonstrates an example of the BF-STEM image from segment A acquired on a segmented detector (a), corresponding 3D reconstruction from all four STEM images can be seen in (b) with 1408 detected nanoparticles, RDA analysis results are presented in (c).

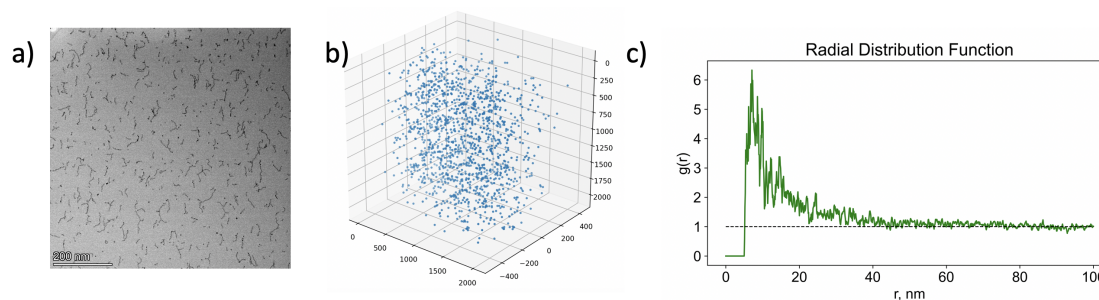


Figure 6.8: Radial distribution analysis of nanoparticles forming long agglomerates in a vitrified solution: (a) BF-STEM image of agglomerated nanoparticles (segment A) in vitrified solution with 10mg/ml concentration, (b) 3D reconstruction using all four views by the 3D tilt-less imaging technique, (c) Radial distribution function  $g(r)$  of the nanoparticles.

When nanoparticles form long agglomerates, the radial distribution function typically shows a broader and less defined peak, indicating that the particles are less dispersed in the solution and are more likely to be found in clusters or aggregates. This is because the particles have a higher probability of interacting with each other and forming larger structures, which affects their distribution within the solution. The first peak in the  $g(r)$  function was observed at 5.1 nm of interparticle distance which corresponds to the average distance between neighboring nanoparticles in a vitrified solution.

## 6.7 Cryo-STEM 3D imaging with pixelated detector

Due to the advantages of using pixelated detectors for tilt-less 3D imaging of dislocations mentioned in Chapter 4 of the thesis, this imaging technique was applied to study the 3D distribution of nanoparticles in a vitrified solution.

The acquisition of the 4D dataset requires a significantly longer time compared to the segmented detector imaging time. Considering this the conditions for cryo-STEM imaging of vitrified samples need to be carefully adjusted in order to prevent electron beam damage. The value of the current on the fluorescent screen was considerably reduced compared to the tilt-less imaging of nanoparticles on a segmented detector, and fixed at the level of 0.010 nA. Counting mode with 2x6Bit was chosen that allowed to reduce the frame time down to 4  $\mu$ s, and ultimately, to reduce the time required to acquire the 4D-STEM dataset. The pixel size in

real space was set at the value of 1 nm, which is 2.5 times larger than the pixel size for imaging with the segmented detector, the total scanned region consisted of 512x512 pixels in real space. The total size of the 4D-STEM dataset is (512, 512, 256, 256). These conditions protected the sample with vitrified ice from melting. The convergence semi-angle of the electron beam was set to 28 mrad with a corresponding 70 $\mu$ m probe-forming aperture.

Fig. 6.9 (a) shows the 4D-STEM imaging scheme of nanoparticles in a vitrified solution on a pixelated detector with (256, 256) pixels in a reciprocal space with the transmitted disc covering the pixelated detector. Calibrated diffraction pattern with four "virtual" detectors with 30, 40, and 50 pixels radii can be seen in (b). During the post-processing of the 4D-STEM dataset, "virtual" detectors can be placed at any place in the reciprocal space and may have varying radii. Virtual BF-STEM images 1, 2, 3, and 4 from corresponding "virtual" detectors (c) were extracted during the post-processing of the 4D-STEM dataset and utilized for the 3D reconstruction (as an example, STEM images of nanoparticles with 50 pixels of "virtual" detector radii are presented in Fig. 6.9). Due to the absence of the diffraction contrast, all four images of nanoparticles were used to perform the 3D reconstruction using the classical computer vision reconstruction technique utilized in section 6.4. Stereo-angle between each pair of the STEM images (1-3) and (2-4) is 3 degrees.

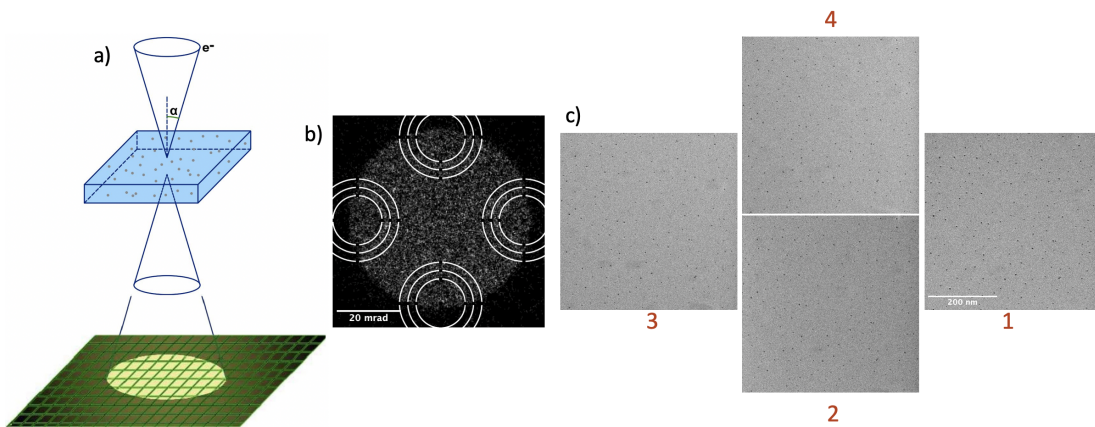


Figure 6.9: 4D-STEM cryo-imaging workflow with pixelated detector: a) Schematic illustration of the 4D-STEM imaging of nanoparticles in vitrified solution on the pixelated detector with (256, 256) pixels, b) Calibrated diffraction pattern in reciprocal space with four "virtual" detectors with 30, 40, and 50 pixels radii and the same coordinate of a center, c) Four virtual BF-STEM images obtained from the corresponding "virtual" detectors in b) with 50 pixels radii.

### 6.7.1 Detection technique

The conditions used for imaging nanoparticles on a pixelated detector were significantly different from the ones used for tilt-less imaging with the segmented detector. In addition to the lower electron dose, pixel size values were considerably larger when performing imaging

on a pixelated detector. As a result, the signal-to-noise ratio on the STEM images from the two detectors is very different. The signal-to-noise ratio can significantly affect the accuracy and reliability of feature detection using classical computer vision algorithms. When the noise in the image is high compared to the signal, it becomes more difficult for the algorithm to distinguish between true image features and noise artifacts.

Sobel operator for the edge detection and Hough transform for circle detection, used previously in section 6.4.2 for STEM images acquired on a segmented detector, demonstrated a low level of performance on the images from the 4D-STEM dataset. These algorithms are not robust to the noise in the images and had difficulties to detect nanoparticles. This resulted in missed and false detections on the STEM images obtained from a pixelated detector, so the detection algorithm needed to be replaced. After testing various classical computer vision techniques, it was found that thresholding in combination with contour detection (from the OpenCV library) displayed improved quality outcomes of nanoparticle detection on noisy images from 4D-STEM data.

Fig. 6.10 shows a 3D reconstruction pipeline of nanoparticles with 10 mg/ml concentration in a vitrified solution imaged on a pixelated detector, with an example of the virtual BF-STEM image extracted from the 4D-STEM dataset using "virtual" detector with 50 pixels in radius (a), image after performing thresholding operation is depicted in (b), and detected nanoparticles drawn on the original STEM image can be observed in (c). After applying these operations on all four virtual BF-STEM images, the final 3D reconstruction can be obtained, see Fig. 6.10 (d).

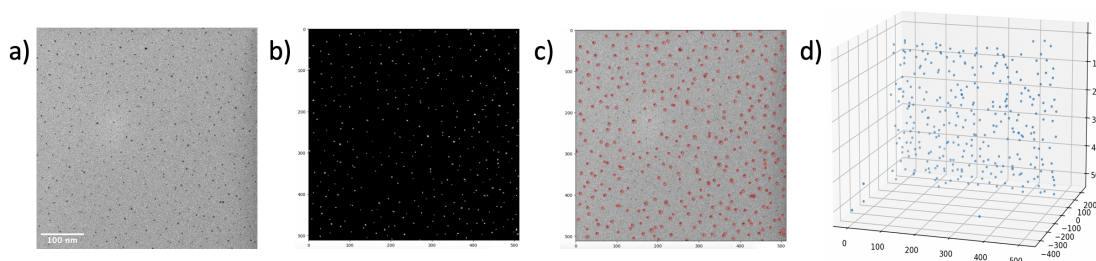


Figure 6.10: 3D reconstruction pipeline of nanoparticles in a vitrified solution imaged on a pixelated detector: (a) An example of virtual BF-STEM image obtained from the 4D-STEM dataset from a "virtual" detector with 50 pixels of radius, (b) Image (a) after applying thresholding operation, (c) Detected on thresholded image contours drawn on an original STEM image, (d) 3D reconstruction after performing steps (b)-(c) on all four virtual STEM images extracted from the 4D dataset. Stereo-angle in each stereo-pair is  $3^\circ$ .

Each technique used for nanoparticles detection is explained in detail below:

*Thresholding.* The original greyscale virtual BF-STEM images from the 4D dataset were thresholded to separate the object of interest (nanoparticles) from the background. This involved setting a threshold value, below which the pixels in the image are considered background. This operation is fast and relatively simple, however, is not particularly convenient, because it requires manually setting the threshold values for each image individually. If imaging or



post-processing conditions are slightly changed, for example, the radii of "virtual" detectors, a manual adjustment of the threshold value needs to be performed again due to a variation in contrast and image quality.

It is worth mentioning that virtual BF-STEM images obtained from the 4D dataset were not preprocessed, unlike the images acquired on a segmented detector. The high-frequency noise was not observed in this case, so the Gaussian blur filter did not improve the quality of the virtual STEM images with their particular noise related to the low electron doses and large pixel sizes.

*Contour detection.* After performing successful thresholding on greyscale STEM images of nanoparticles, a contour detection algorithm was applied to the binary images, where nanoparticles are separated from the background. Contour detection is a common image processing technique used to extract the boundaries of objects or shapes in an image. Typically, a specific contour refers to boundary pixels that have identical color and intensity. The black pixels, having a value of 0, are considered background pixels and ignored. Firstly, the *findContours()* function is used to detect the contours on the images. This function returns a list of contours, each of which is a list of points that define the boundary of an object. Then, the contours are visualized on the original image (red circles in 6.10 (c)) using the *drawContours()* function. The coordinates of the center of the red circles were extracted and used for the following stereo-matching and 3D reconstruction.

### 6.7.2 3D reconstruction and RDA

For the 3D reconstruction of the detected nanoparticles from four virtual BF-STEM images, an algorithm from section 6.4.3 was used.

As can be seen in Fig. 6.10, not all nanoparticles were successfully detected on the STEM images extracted from a 4D dataset using a "virtual" detector with 50 pixels of radius. Nanoparticles can be reconstructed in the 3D volume of the sample only if the algorithm finds correspondences in all four images. A detection missed in only one image will cause the absence of this nanoparticle in the final 3D reconstruction.

To increase the probability of nanoparticle detection in the images, when the threshold value is already optimized, the radii of the "virtual" detector can be varied in the post-processing of the 4D-STEM dataset. To find an optimal value of the radius for virtual imaging, "virtual" detectors with various radii were tested, in particular, with 30, 40, 50, 60, and 70 pixels. When the radius of the "virtual" detector is 50 pixels, the algorithm detected 366 nanoparticles, however, correspondences were found only for 309 nanoparticles. Decreasing the radii of "virtual" detectors led to an even smaller number of detected nanoparticles. For example, virtual images extracted with 40 pixels radii of "virtual" detectors had only 264 nanoparticles in the final 3D reconstruction. Increasing the radius of a "virtual" detector can lead to the integration of aberrations dominating at the large values of convergence semi-angle and

blurring of nanoparticles in the image, but a better signal-to-noise ratio. When the radii of "virtual" detectors were set to 70 pixels, visual improvement in STEM image quality and following detection were noticed, with a 363 nanoparticles in the final 3D reconstruction, see Fig. 6.11 (a) and (b). It was concluded that the optimal radii of "virtual" detectors are 70 pixels for the virtual imaging and 3D reconstruction when utilizing the convergence semi-angle of 28 mrad.

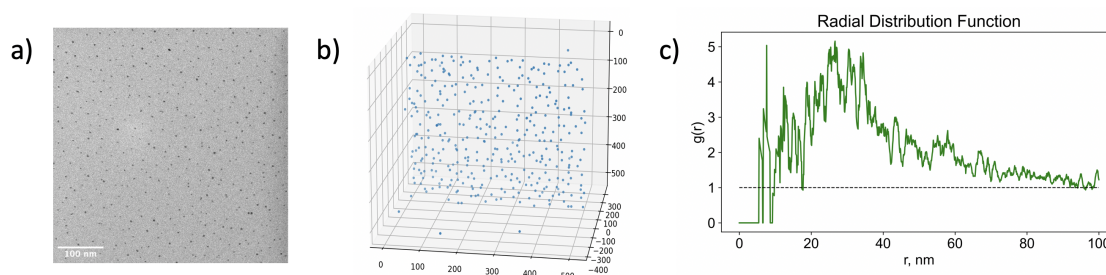


Figure 6.11: Radial distribution analysis of nanoparticles with 10 mg/ml of concentration: (a) an example of virtual BF-STEM image of nanoparticles extracted from 4D-STEM dataset with 70 pixels radius of "virtual" detector, (b) 3D reconstruction by 3D tilt-less imaging technique using four virtual BF-STEM images, (c) Radial distribution function  $g(r)$  of the nanoparticles calculated from the 3D reconstruction.

After extraction of the 3D coordinates of nanoparticles reconstructed in Fig. 6.11 (b) the computation of the  $g(r)$  was performed. RDF was computed using the bin size 1, due to the pixel size value of 1 nm. The first peak in the  $g(r)$  function was observed at 5.5 nm interparticle distance, see Fig. 6.11 (c). The distance where the first peak appears in the  $g(r)$  function is exactly at the same distance of the first peak in RDF obtained from the segmented detector for the specimen with a 10mg/ml concentration of nanoparticles in a solution. This confirms the validity of this approach for the determination of the 3D distribution of nanoparticles in a vitrified solution.

### 6.7.3 Large convergence semi-angle

Tilt-less 3D imaging of nanoparticles on a pixelated detector was performed with 60 mrad of convergence semi-angle, using the largest condenser aperture on a Titan Themis microscope with  $150\mu\text{m}$  in diameter. The 4D-STEM dataset was acquired at a smaller value of CL, particularly 58 mm, and with a slightly higher value of the electron dose, in comparison to the 4D-STEM imaging with 28 mrad of convergence semi-angle.

Fig. 6.12 shows the results of the 4D-STEM imaging with  $\alpha=60$  mrad, and the detection results with the 3D reconstruction of the nanoparticles. The virtual BF-STEM images were obtained from the "virtual" detectors with 80 pixels of radii. As can be seen on the virtual STEM image the nanoparticles are blurred and distorted due to the aberrations of the probe dominating at the large convergence semi-angles. There is also a high level of noise in the obtained images. Increasing the radii of the "virtual" detectors can lead to a better signal-to-noise ratio,

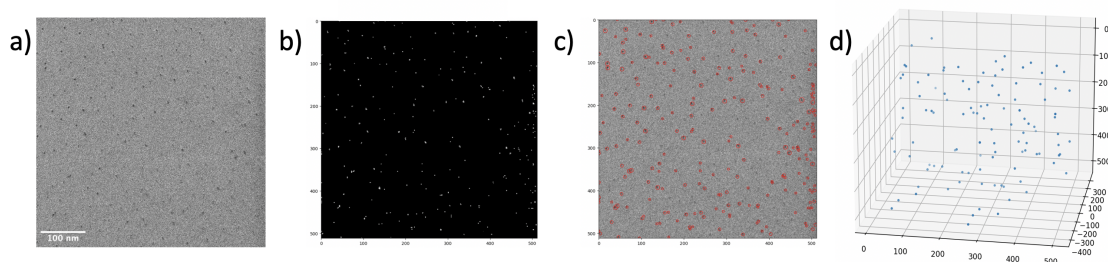


Figure 6.12: 3D reconstruction procedure of virtual BF-STEM images acquired with 60 mrad of convergence semi-angle: (a) an example of virtual BF-STEM image of nanoparticles extracted from 4D-STEM dataset with 80 pixels radius of "virtual" detector, (b) Image (a) after applying thresholding operation, (c) Detected on thresholded image contours drawn on an original STEM image, (d) 3D reconstruction after performing steps (b)-(c) on all four virtual STEM images extracted from the 4D dataset. Stereo-angle in each stereo-pair is  $6^\circ$ .

however, the blurring effect due to the aberrations will amplify. Nanoparticles' detection was unsuccessful with the employed classical computer vision algorithms. The high level of noise in the images led to false detections, and due to the presence of many blurred nanoparticles, they were not detected.

Ultimately, the imaging mode with a large convergence semi-angle is not recommended for the tilt-less 3D imaging of nanoparticles under cryo-condition.

#### 6.7.4 Application to other samples

In order to test our approach, the tilt-less 3D imaging with the pixelated detector and 3D reconstruction pipeline was used to study cryo-samples with various concentrations of nanoparticles. Then developed detection approach was used on virtual BF-STEM images obtained from the 4D-STEM datasets using "virtual" detectors with 70 pixels of radii. In this section, the results from the highest and lowest concentrations of nanoparticles in a vitrified solution will be presented, 40 mg/ml and 2.5 mg/ml respectively.

##### *Sample with a high concentration of nanoparticles.*

Fig. 6.13 depicts the RDA process of the cryo-specimen with a high concentration of nanoparticles in a solution, particularly, 40 mg/ml. An example of the virtual BF-STEM image extracted from the 4D dataset can be seen in (a), the final 3D reconstruction using all four images in (b), and the RDF calculated from the (b) can be observed in (c). The number of detected nanoparticles is 1066, however, the number of nanoparticles that found correspondences in all four views, so in the final 3D reconstruction is 960.

The obtained  $g(r)$  function for the cryo-sample with a high concentration of nanoparticles is similar to the RDF obtained from the segmented detector with the same concentration. The first peak here is observed at 4.5 nm of interparticle distance, causing nanoparticles to be



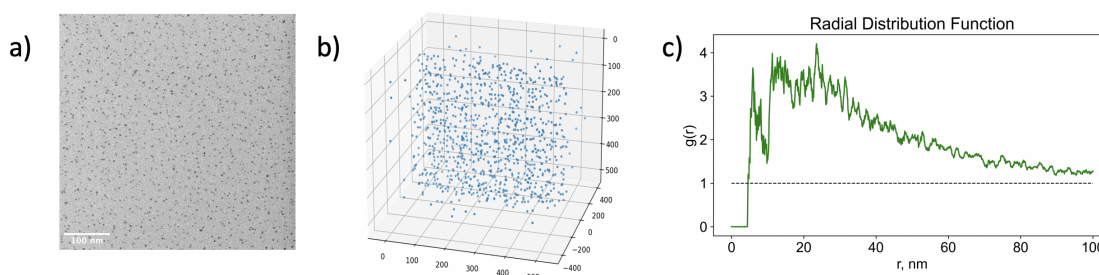


Figure 6.13: Radial distribution analysis of nanoparticles with 40 mg/ml of concentration: (a) an example of virtual BF-STEM image of nanoparticles extracted from 4D-STEM dataset with 70 pixels radius of "virtual" detector, (b) 3D reconstruction by 3D tilt-less imaging technique using four virtual BF-STEM images, (c) Radial distribution function  $g(r)$  of the nanoparticles calculated from the 3D reconstruction.

closer to each other.

#### *Diluted sample.*

The cryo-sample with a high level of dilution was prepared for the 3D tilt-less imaging on a pixelated detector. The concentration of nanoparticles in this sample was only 2.5 mg/ml. Fig. 6.14 represents the RDA of the sample with an example of the virtual BF-STEM image in (a), corresponding 3D reconstruction from four images can be seen in (b), with the results of nanoparticles' distribution analysis in (c). Due to the low concentration of the nanoparticles in the solution, the detection algorithm found 230 nanoparticles in the first image, and correspondences were found for the 185 nanoparticles for the final 3D reconstruction in a 3D volume of the vitrified solution.

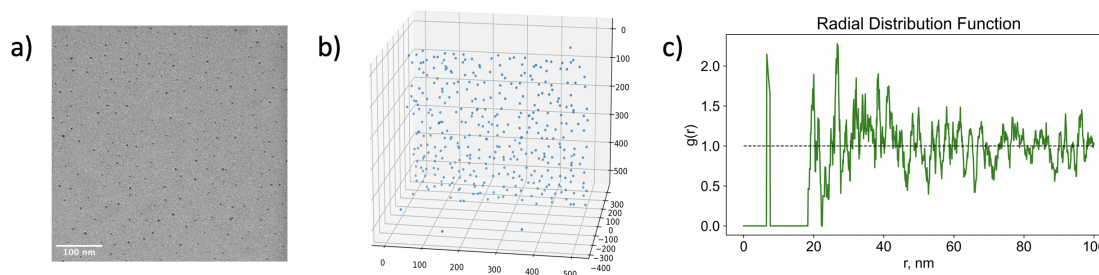


Figure 6.14: Radial distribution analysis of nanoparticles with 2.5 mg/ml of concentration: (a) an example of virtual BF-STEM image of nanoparticles extracted from 4D-STEM dataset with 70 pixels radius of "virtual" detector, (b) 3D reconstruction by 3D tilt-less imaging technique using four virtual BF-STEM images, (c) Radial distribution function  $g(r)$  of the nanoparticles calculated from the 3D reconstruction.

The radial distribution function exhibits the first peak at 6.6 nm interparticle distance. However, at distances around 20 nm, most of the nanoparticles are found. This corresponds to the average distance that can be visually observed in the virtual BF-STEM images for the highly

diluted specimen. It is important to mention that, the cryo-samples with low concentrations require acquiring more datasets for statistically meaningful results in the calculation of the  $g(r)$  functions.

## 6.8 Concluding remarks

In this Chapter of the thesis, tilt-less 3D imaging was applied for the first time to study the 3D distribution of nanoparticles in a vitrified solution. Optimal STEM imaging conditions were found for the tilt-less cryo-imaging on two different detectors: a segmented detector with an annular shape and a pixelated detector.

Simultaneous collection of the STEM images from four segments of the annular detector reduced the imaging time to 1 minute compared to the conventional tomography approach, which requires 1.5 hours to acquire one dataset. Together with the developed classical computer vision algorithm for the 3D reconstruction this novel approach allowed to obtain the 3D distribution of the nanoparticles within a 3D volume of a frozen solution from four views with noticeably reduced time and electron damage to the sample. Our approach has the potential to study the dynamical processes of nanoparticle systems over time, which is important for ensuring their effectiveness and safety in biological and environmental systems. Due to the fast acquisition statistically meaningful results can be obtained by performing tilt-less 3D imaging in multiple sample locations.

Acquisition of the 4D-STEM dataset using the pixelated detectors on a cryo-sample is a challenging procedure. Cryo-imaging on a pixelated detector requires a longer time (approximately 6 minutes for the acquisition of one 4D-STEM dataset), and in order to protect the sample from electron damage, lower electron doses need to be used and larger pixel sizes, this degrades the spatial resolution compared to the segmented detector and increases the noise level. Due to those differences another algorithm needed to be developed to perform nanoparticles' detection on 2D images obtained from the 4D dataset. However, the new algorithm requires manual adjustments of the threshold values for each STEM image.

We propose the utilization of deep learning neural networks for the 3D reconstruction of the nanoparticles. However, it requires performing the tedious training procedure with the STEM images of nanoparticles, this approach demonstrated its robustness to the noise level for the STEM images of dislocations. The use of deep learning CNNs will allow to avoid using manual adjustments of thresholds and eliminate the missing and false detections of the nanoparticles which appear when using classical computer vision techniques. This will potentially lead to a more precise 3D reconstruction and analysis of nanoparticles, especially when using pixelated detectors, where the stereo-angle between each pair of images can be precisely defined.



# 7 Conclusion

## 7.1 Achieved results

In the framework of this interdisciplinary project with the development of the novel detector's technology and computer vision algorithms it became possible to improve methods for the 3D imaging and reconstruction of one-dimensional curvilinear and point-like structures observed in STEM images. The developed tools have been optimized to complement the unique characteristics of electron microscopy images, enabling a fast, effective, and productive analytical process. The source codes and acquired datasets are open-source and publicly available to the scientific community.

The project encompassed various objectives, and I have listed the achievements for each part below.

### **Automatic stereo 3D reconstruction of dislocations using deep learning neural networks**

A fully automated stereo-based approach was developed to perform the 3D reconstruction of the curvilinear structures observed in a TEM. The technique was tested for the challenging case of dislocations. The output is presented in the crystallographic frame of reference of the specimen which gives the researchers the opportunity to extract useful information about the material properties. Only two images are utilized as an input, which compared to conventional tomography, reduces the imaging and post-processing times. The accuracy of the final 3D reconstruction is similar to the tomography techniques, coupled with an added advantage as the elimination of manual thresholding of final reconstruction results. The missing wedge effect has been replaced by a new challenge, where uncertainty in the depth position emerges. However, by leveraging the prior knowledge of the curvilinear shape of the structure, this uncertainty can be limited to a few nanometers when the stereo-angle is increased beyond of approximately 8 degrees. The principal component of the developed method is a deep learning neural network that jointly detects dislocations in a stereo-pair and matches them to recover their 3D structure while supporting end-to-end training with semi-supervised approaches. The developed approach has been integrated into a graphical software tool that

facilitates fast and easy reconstruction and visualization of dislocations from stereo-pairs of images.

A systematic investigation of the diffraction and STEM imaging conditions was performed using the segmentation neural network outputs and topological data analysis. This allowed the optimization of the imaging conditions to work together with the neural networks and deliver the most precise results. Important parameters for the STEM imaging were systematically quantified, for example, pixel size and dwell time, allowing the acquisition of the stereo-pair with the smallest errors in the post-processing by neural networks. It was demonstrated that the developed 3D reconstruction pipeline based on a neural network approach is robust to the noise level on the STEM images and allows to reduce the acquisition time without losing the quality of the dataset and outputs of the neural networks.

The accuracy of the 3D reconstruction was improved by augmentation of the size of the training dataset with synthetically generated images. Due to the limited amount of experimental electron microscopy images and the necessity of using human annotations for the creation of 2D ground-truth, a new pipeline was developed for the automatic generation of realistically-looking STEM images of dislocations using the GAN-SPADE network.

### **Tilt-less 3D imaging and reconstruction using the segmented and pixelated detectors**

A recently developed tilt-less 3D imaging technique was further optimized to simultaneously generate a stereo-pair of STEM dislocation images with a larger stereo-angle utilizing a fast segmented detector on a Cs-corrected microscope. This technique eliminates the necessity of mechanical tilt of the specimen, and hence the alignment of the STEM images, and reduces the time of electron exposure, which is crucial for radiation-sensitive materials. In combination with the automatic 3D reconstruction approach, it was possible to obtain the 3D distribution of dislocations rapidly. However, due to the shape of the detector's segments, it is impossible to determine precisely the stereo-angle which can cause the degradation of the 3D reconstruction's quality.

Utilization of the novel pixelated detector on a Cs-corrected microscope, due to the possibility of a more precise location of the "virtual" detectors in the post-processing procedure, allowed for reduction of the image degradation due to the aberrations dominating at large values of the convergence semi-angles. It also gives an opportunity to precisely determine the stereo-angle, with the record value of 9.32 degrees. Custom Python scripts were developed to perform the post-processing of the 4D-STEM dataset and extract the virtual BF-STEM images. This technique allows the generation of multiple images from different viewing angles after the acquisition of the 4D-STEM dataset which potentially can improve the precision of the 3D reconstruction. Also, a method for the generation of an additional training dataset was proposed, which facilitates the labeling task by humans by creating only one segmentation mask and multiple images for training and allows for a decrease of the domain gap between various STEM detectors, hence improving the performance of the neural networks on the virtual STEM images from the 4D-STEM dataset. Furthermore, the high quality and DQE of

the modern pixelated detectors allowed for the first time to achieve the largest value of the stereo-angle between two virtual STEM images without the necessity of tilting the specimen.

### **3D distribution of nanoparticles imaged in cryoSTEM condition**

For the first time, the tilt-less 3D imaging technique in STEM was applied to study the 3D distribution of nanoparticles in a vitrified solution. The imaging conditions were optimized for imaging with segmented and pixelated detectors to prevent electron damage to a vitrified specimen. This allowed the simultaneous acquisition of the STEM images with different viewing angles at a single sample tilt. The 3D reconstruction algorithm based on classical computer vision techniques was developed in order to obtain the 3D coordinates of the nanoparticles in the volume of the vitrified solution. The reconstruction algorithm is based on the concept of the stereo-matching with modifications, accounting for the particularities of the segmented detector's geometry, and utilization of the four STEM images simultaneously acquired as input. The information extracted from the final 3D distribution of nanoparticles is used to calculate the radial distribution function, which is an important characteristic for the analysis of these systems. It was demonstrated that this novel approach is delivering similar results compared to the conventional tomography reconstruction, while considerably reducing the imaging time (from 1.5 hours to 1 minute on a fast segmented detector).

## **7.2 Outlook**

### **Multi-view 3D reconstruction**

The utilization of modern pixelated detectors with a large number of pixels allows the extraction of multiple virtual BF-STEM images with different viewing angles on a specimen. However, in the current project, the 3D reconstruction of curvilinear one-dimensional structures is performed by utilization of only two images, i.e. one stereo-pair, due to the architecture of the neural networks that are designed to perform stereo detection and matching by taking two images as an input. Further improvement can be achieved by implementation of the multi-view neural networks. Utilization of these types of neural networks with multiple images extracted from the 4D-STEM dataset can increase the precision of the final 3D reconstruction and decrease the number of ambiguities in it.

### **Physics-informed algorithms for 3D reconstruction**

Most neural network algorithms utilized for scientific data analysis rely exclusively on a data-driven approach, disregarding the actual physical phenomenon. This approach can have significant drawbacks, as the neural network accurately models the physical process within the experimental data but fails to generalize beyond the training data. Physics-informed neural networks have been developed to integrate the knowledge of the underlying physical processes into machine learning algorithms [91]. By utilizing state-of-the-art NeRF neural networks, it becomes feasible to integrate the contrast formation mechanisms of the STEM

images into the creation of a 3D reconstruction that holds physical significance. In addition, NeRF networks provide the flexibility to incorporate multiple input images, which is especially advantageous when imaging with pixelated detectors. In the framework of the SCEM project, the first attempt in this direction has been made for the STEM images of dislocations (acquired for tomography reconstruction in Chapter 2), using the absorption contrast theory, and the NeuS network architecture [92]. The stack of dislocation images consisting of 39 BF-STEM images was given as input to the NeuS network to optimize the model. After the optimization procedure, the network was able to perform the rendering of a 3D scene, so that the rendered views match the given inputs. This procedure allowed us to obtain the 3D distribution of dislocations in the sample volume. The preliminary results obtained by this approach can be seen in Fig. 7.1, representing the different views on the 3D volume generated with the outputs of the NeuS network.

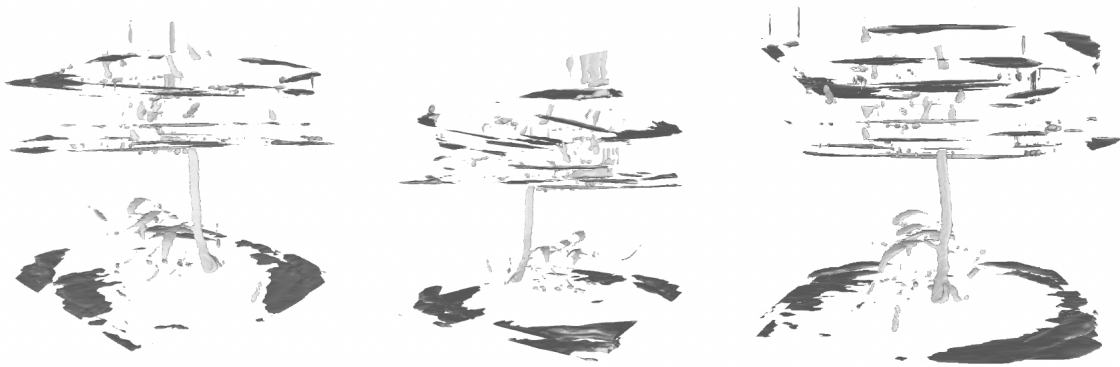


Figure 7.1: Multiple views of the 3D volume generated by the NeuS network, utilizing (multiple) STEM images of dislocations as an input. Light grey lines correspond to the dislocation structures, and dark grey regions to the grain boundaries reconstructed from the STEM images.

As can be observed in Fig. 7.1 a major part of the dislocation networks is missing in the 3D volume. To address this issue, optimizations need to be made in the algorithm, in particular, an effort to model the diffraction contrast of dislocations. This will allow generating the unseen by the network views on the sample with higher precision. Moreover, an approach based on the NeRF networks can automatize the 3D reconstruction of more complex 2D and 3D objects, in particular, the biological specimens utilizing the images acquired by cryo-electron microscopy, and by incorporating the phase contrast formation mechanisms in the algorithm. It can also be combined with EDX or Electron Energy Loss Spectroscopy (EELS) tomography to perform the 3D reconstruction addressing the information from multiple channels.

### Quantification in 3D

The 3D reconstruction can be further quantified using the TDA tool. In Chapter 4 quantification of the 2D outputs of the UNet segmentation network was performed for the images acquired with different imaging conditions by comparing them to the manually annotated 2D ground-truths. In order to perform the quantification of the developed stereo 3D CNN neural

network and its outputs, the 3D ground-truth is required. However, the real distribution of dislocations in the volume of the sample is unknown, so the 3D ground-truth is not available. Nevertheless, it can be obtained by the creation of the synthetic specimen, using dislocation contrast simulation software to generate the synthetic stereo-pair of images.

### **3D distribution of nanoparticles**

The tilt-less 3D imaging can be used to observe the dynamic of the nanoparticles in a 3D volume within the solution when utilizing fast segmented detectors. For this task, 3D imaging can be performed with modern liquid holders, and utilizing a novel Panther STEM detector with 16 segments installed on a Titan Themis microscope at CIME, EPFL. This approach in combination with the developed algorithms for 3D reconstruction will allow performing the analysis of the solution with the nanoparticles in a liquid state revealing the changes in their 3D distribution over time intervals.

As demonstrated in Chapter 6, the detection algorithm based on the classical computer vision approach is not robust to the noise level when utilized on the STEM images of the nanoparticles acquired on the different segments of a segmented detector. Hence, the missing and fault detections appear in the noisy stereo-pair, which are not reconstructed as a result. Algorithms based on neural networks have proven to be more robust to the noise level on STEM images. In order to utilize the neural networks for the detection and 3D reconstruction of nanoparticles they need to be trained with at least 100 STEM images of nanoparticles. However, potentially, it can improve the quality of the 3D reconstruction and avoid manual intervention, like an adjustment of the thresholds, and detection parameters in the classical computer vision approach.





# Bibliography

- [1] S. Amelinckx, “The Characterization of Defects in Crystals”, *Journal of Crystal Growth*, pp. 6–10, 1974.
- [2] P. B. Hirsch, R. W. Horne, and M. J. Whelan, “Direct Observations of the Arrangement and Motion of Dislocations in Aluminium”, *Philosophical Magazine*, vol. 86, no. 29-31, pp. 4553–4572, 2006.
- [3] P. B. Hirsch, A. Howie, R. Nicholson, D. W. Pashley, and M. J. Whelan, *Microscopy of thin crystals*, 1977.
- [4] Z. Feng, R. Fu, C. Lin, *et al.*, “Tem-based dislocation tomography: challenges and opportunities”, *Current Opinion in Solid State and Materials Science*, vol. 24, no. 3, p. 100 833, 2020, ISSN: 1359-0286.
- [5] H. Jelena, G. Abdul, W. Katharina, *et al.*, “Exceptional strengthening of biodegradable mg-zn-ca alloys through high pressure torsion and subsequent heat treatment”, *Materials*, vol. 12, no. 15, 2019, ISSN: 1996-1944.
- [6] X. Huang, N. Hansen, and N. Tsuji, “Hardening by annealing and softening by deformation in nanostructured metals”, *Science*, vol. 312, no. 5771, pp. 249–251, 2006.
- [7] E. Ma, T. Shen, and X. Wu, “Less is more”, *Nature Mater*, vol. 5, pp. 515–516, 2006.
- [8] J. Sharp, “Electron Tomography of Defects”, Ph.D. dissertation, Wolfson College Cambridge, 2010.
- [9] E. Oveisi, “Three-Dimensional STEM Imaging of Dislocations”, Ph.D. thesis, EPFL, Lausanne, Switzerland, 2015.
- [10] A. Alpers, R. J. Gardner, S. König, *et al.*, “Geometric reconstruction methods for electron tomography”, *Ultramicroscopy*, vol. 128, pp. 42–54, 2013, ISSN: 0304-3991.
- [11] R. B. Sills and D. L. Medlin, “Semi-automated, object-based tomography of dislocation structures”, *Microsc Microanal.*, vol. 8, pp. 1–13, 2022.
- [12] K. Batenburg, S. Bals, J. Sijbers, *et al.*, “3d imaging of nanomaterials by discrete tomography”, *Ultramicroscopy*, vol. 109, no. 6, pp. 730–740, 2009, ISSN: 0304-3991.
- [13] B. Goris, T. Roelandts, K. Batenburg, H. Heidari Mezerji, and S. Bals, “Advanced reconstruction algorithms for electron tomography: from comparison to combination”, *Ultramicroscopy*, vol. 127, pp. 40–47, 2013, ISSN: 0304-3991.

- [14] B. Goris, W. V. den Broek, K. Batenburg, H. H. Mezerji, and S. Bals, “Electron tomography based on a total variation minimization reconstruction technique”, *Ultramicroscopy*, vol. 113, pp. 120–130, 2012.
- [15] Z. Saghi, D. J. Holland, R. Leary, *et al.*, “Three-dimensional morphology of iron oxide nanoparticles with reactive concave surfaces. a compressed sensing-electron tomography (cs-et) approach”, *Nano Letters*, vol. 11, no. 11, pp. 4666–4673, 2011.
- [16] E. Candes and T. Tao, “Near-optimal signal recovery from random projections: universal encoding strategies”, *IEEE Trans. Inf. Theory*, vol. 52, pp. 5406–5425, 2006.
- [17] L. Turpin, S. Roux, O. Caty, S. Denneulin, and D. Sébastien, “A phase-field approach to limited-angle tomographic reconstruction”, <https://hal.archives-ouvertes.fr/hal-02350800>, 2019.
- [18] P. Piau, A. King, L. Henry, *et al.*, “A thresholding based iterative reconstruction method for limited-angle tomography data”, *Tomography of Materials and Structures*, vol. 2, p. 100 008, 2023, ISSN: 2949-673X.
- [19] J. Schwartz, H. Zheng, M. Hanwell, Y. Jiang, and R. Hovden, “Dynamic compressed sensing for real-time tomographic reconstruction”, *Ultramicroscopy*, vol. 219, p. 113 122, 2020, ISSN: 0304-3991.
- [20] D. B. Williams and C. B. Carter, *Transmission electron microscopy*. Springer, 1996.
- [21] A. Jacome, K. Pöthkow, O. Paetsch, and H.-C. Hege, “Three-Dimensional Reconstruction and Quantification of Dislocation Substructures from Transmission Electron Microscopy Stereo Pairs”, *Ultramicroscopy*, vol. 195, pp. 157–170, 2018.
- [22] E. Oveisi, A. Letouzey, S. D. Zanet, *et al.*, “Stereo-Vision Three-Dimensional Reconstruction of Curvilinear Structures Imaged with a TEM”, *Ultramicroscopy*, vol. 184, no. A, pp. 116–124, 2018.
- [23] F. D. León-Cázares, C. Kienl, and C. M. F. Rae, “Three-dimensional reconstruction of planar deformation features from single electron micrographs.”, *Metall Mater Trans.*, vol. 51, pp. 1163–1172, 2020.
- [24] J. M. Ede, “Deep learning in electron microscopy”, *Mach. Learn.: Sci. Technol.*, vol. 2, no. 1, 2021.
- [25] W. Xu and J. LeBeau, “A deep convolutional neural network to analyze position averaged convergent beam electron diffraction patterns”, *Ultramicroscopy*, vol. 188, pp. 59–69, 2018, ISSN: 0304-3991.
- [26] G. Roberts, S. Y. Haile, and R. S. et al, “Deep learning for semantic segmentation of defects in advanced stem images of steels”, *Sci Rep*, vol. 9, 2019.
- [27] M. Z. et al., “Deep learning for atomically resolved imaging”, *Microscopy and Microanalysis*, vol. 24, pp. 60–61, 2018.
- [28] H. Kniesel, T. Ropinski, T. Bergner, *et al.*, *Clean implicit 3d structure from noisy 2d stem images*, 2022. arXiv: 2203.15434 [eess . IV].

- [29] Q. T. Minh, H. D. G. Colburn, L. Kanggeun, *et al.*, “Removing imaging artifacts in electron microscopy using an asymmetrically cyclic adversarial network without paired training data”, in *2019 IEEE/CVF International Conference on Computer Vision Workshop (ICCVW)*, 2019, pp. 3804–3813.
- [30] I. MacLaren, T. A. Macgregor, C. S. Allen, and A. I. Kirkland, “Detectors—The ongoing revolution in scanning transmission electron microscopy and why this important to material characterization”, *APL Mater*, vol. 8, no. 11, 2020.
- [31] O. Colin, “Four-dimensional scanning transmission electron microscopy (4d-stem): from scanning nanodiffraction to ptychography and beyond”, *Microscopy and Microanalysis*, vol. 25, no. 3, pp. 563–582, 2019.
- [32] E. Oveisi, A. Letouzey, D. Alexander, *et al.*, “Tilt-Less 3D Electron Imaging and Reconstruction of Complex Curvilinear Structures”, *SREP*, vol. 7, no. 10630, 2017.
- [33] Y. W. Kim, R. Wagner, and Y. Masaharu, “Gamma titanium aluminides”, Dec. 1995. [Online]. Available: <https://www.osti.gov/biblio/225071>.
- [34] D. M. Dimiduk, D. Miracle, and C. H. Ward, “Development of intermetallic materials for aerospace systems”, *Materials Science and Technology*, vol. 8, no. 4, pp. 367–375, 1992.
- [35] B. Michael, K. Thomas, L. Janny, *et al.*, “An advanced tial alloy for high-performance racing applications”, *Materials*, vol. 13, no. 21, p. 4720, 2020.
- [36] P. R. Subramanian, M. G. Mendiratta, and D. M. Dimiduk, “The development of nb-based advanced intermetallic alloys for structural applications”, *Jom*, vol. 48, no. 1, pp. 33–38, 1996.
- [37] R. Pflumm, A. Donchev, and S. M. et al., “High-temperature oxidation behavior of multi-phase Mo-containing  $\gamma$ -TiAl-based alloys”, *Intermetallics*, vol. 53, pp. 45–55, 2014, ISSN: 0966-9795.
- [38] F. Appel, U. Brossmann, U. Christoph, *et al.*, “Recent progress in the development of gamma titanium aluminide alloys”, *Advanced Engineering Materials*, vol. 2, no. 11, pp. 699–720, 2000.
- [39] C. Helmut and M. Svea, “Design, processing, microstructure, properties, and applications of advanced intermetallic tial alloys”, *Advanced Engineering Materials*, vol. 15, no. 4, pp. 191–215, 2013.
- [40] L. Giannuzzi and F. Stevie, “A review of focused ion beam milling techniques for tem specimen preparation”, *Micron*, vol. 30, no. 3, pp. 197–204, 1999, ISSN: 0968-4328.
- [41] P. Albarede and H. Lezec, “Transmission electron microscopy of focused ion beam induced damage at 50 keV in Si”, *H.A. Calderon Benavides M.J. Yacamán (Eds.), Electron Microscopy 1998, ICEM14, Symposium HH, Institute of Physics, Bristol*, p. 431, 1998.
- [42] S. Lee, J. Jeong, Y. Kim, S. M. Han, D. Kiener, and S. H. Oh, “Fib-induced dislocations in Al submicron pillars: annihilation by thermal annealing and effects on deformation behavior”, *Acta Materialia*, vol. 110, pp. 283–294, 2016, ISSN: 1359-6454.

- [43] U. Necip, "Preparation of high quality al tem specimens via a double-jet electropolishing technique", *Materials Characterization*, vol. 59, pp. 547–553, May 2008.
- [44] A. Pakzad, M. Stephen, V. Cathy, C. Jayhoon, and L. Guoda, "Application of low energy broad ion beam milling to improve the quality of fib prepared tem samples", *Microscopy and Microanalysis*, vol. 19, pp. 1326–1327, Aug. 2013.
- [45] J. Lapin, "TiAl-based Alloys: Present Status and Future Perspectives", *METAL 2009*, vol. 5, pp. 19–21, 2009.
- [46] H. Okamoto, "Phase diagrams for binary alloys", *ASM International, Materials Park, OH*, 2009.
- [47] F. Appel and R. Wagner, "Microstructure and deformation of two-phase  $\gamma$ -titanium aluminides", *Materials Science and Engineering R: Reports*, vol. 22, no. 5, pp. 187–268, 1998.
- [48] A. Guitton, H. Kriaa, E. Bouzy, J. Guyon, and N. Maloufi, "A dislocation-scale characterization of the evolution of deformation microstructures around nanoindentation imprints in a tial alloy", *Materials (Basel)*, vol. 11, no. 2, 2018.
- [49] P. Stadelmann, "Ems - a software package for electron diffraction analysis and hrem image simulation in materials science", *Ultramicroscopy*, vol. 21, no. 2, pp. 131–145, 1987, ISSN: 0304-3991.
- [50] R. Vincent and P. Midgley, "Double conical beam-rocking system for measurement of integrated electron diffraction intensities", *Ultramicroscopy*, vol. 53, no. 3, pp. 271–282, 1994, ISSN: 0304-3991.
- [51] K. Chan and Y. Kim, "Rate and environmental effects on fracture of a two-phase tial-alloy", *Metall Mater Trans A*, vol. 24, pp. 113–125, 1993, ISSN: 0304-3991.
- [52] E. Oveisi, M. C. Spadaro, E. Rotunno, V. Grillo, and C. Hebert, "Insights into Image Contrast from Dislocations in ADF-STEM", *Ultramicroscopy*, vol. 200, pp. 139–148, 2019.
- [53] P. Phillips, M. Brandes, M. Mills, and M. De Graef, "Diffraction contrast stem of dislocations: imaging and simulations", *Ultramicroscopy*, vol. 111, no. 9, pp. 1483–1487, 2011, ISSN: 0304-3991.
- [54] Y. Zhu, C. Ophus, M. B. Toloczko, and D. J. Edwards, "Towards bend-contour-free dislocation imaging via diffraction contrast stem", *Ultramicroscopy*, vol. 193, pp. 12–23, 2018, ISSN: 0304-3991.
- [55] R. Schäublin and P. Stadelmann, "A method for simulating electron microscope dislocation images", *Materials Science and Engineering: A*, vol. 164, no. 1, pp. 373–378, 1993, ISSN: 0921-5093.
- [56] S. Robert, "Stereoscopic photography in transmitted light microscopy", *Microscopy Today*, vol. 25, no. 4, pp. 46–49, 2017.
- [57] O. Ronneberger, P. Fischer, and T. Brox, "U-net: convolutional networks for biomedical image segmentation", 2015.

- [58] D. G. Lowe, "Distinctive Image Features from Scale-Invariant Keypoints", *IJCV*, vol. 20, no. 2, pp. 91–110, 2004.
- [59] R. Bolles and R. Horaud, "3DPO: A Three-Dimensional Part Orientation System", *IJRR*, vol. 5, no. 3, pp. 3–26, 1986.
- [60] J. Bromley, I. Guyon, Y. LeCun, E. Säcker, and R. Shah, "Signature verification using a "Siamese" time delay neural network", pp. 737–744, 1993.
- [61] A. Kendall, H. Martirosyan, S. Dasgupta, and P. Henry, "End-To-End Learning of Geometry and Context for Deep Stereo Regression", in *ICCV*, 2017.
- [62] Z. Liang, Y. Feng, Y. Guo, *et al.*, "Learning for Disparity Estimation through Feature Constancy", in *CVPR*, 2018.
- [63] J. Pang, W. Sun, J. S. Ren, C. Yang, and Q. Yan, "Cascade Residual Learning: A Two-stage Convolutional Network for Stereo Matching", in *ICCVW*, 2017.
- [64] D. P. Kingma and J. Ba, "Adam: A method for stochastic optimization", in *3rd International Conference on Learning Representations, ICLR 2015, San Diego, CA, USA, May 7-9, 2015, Conference Track Proceedings*, Y. Bengio and Y. LeCun, Eds., 2015.
- [65] T. Park, M.-Y. Liu, T.-C. Wang, and J.-Y. Zhu, "Semantic image synthesis with spatially-adaptive normalization", in *Proceedings of the IEEE Conference on Computer Vision and Pattern Recognition*, 2019.
- [66] N. H. Dekkers and H. de Lang, "Differential phase contrast in stem", *Optik (Jena)*, vol. 41, no. 4, pp. 452–456, 1974.
- [67] H. Rose, "Nonstandard imaging methods in electron microscopy", *Ultramicroscopy*, vol. 2, pp. 251–267, 1976, ISSN: 0304-3991.
- [68] J. N. Chapman, "The investigation of magnetic domain structures in thin foils by electron microscopy", *Journal of Physics D: Applied Physics*, vol. 17, no. 4, pp. 623–647, 1984.
- [69] K. Ooe, T. Seki, Y. Ikuhara, and N. Shibata, "Ultra-high contrast stem imaging for segmented/pixelated detectors by maximizing the signal-to-noise ratio", *Ultramicroscopy*, vol. 220, p. 113 133, 2021, ISSN: 0304-3991.
- [70] G. McMullan, D. Cattermole, S. Chen, *et al.*, "Electron imaging with medipix2 hybrid pixel detector", *Ultramicroscopy*, vol. 107, no. 4, pp. 401–413, 2007, ISSN: 0304-3991.
- [71] M. Krajnak, D. McGrouther, D. Maneuski, V. O. Shea, and S. McVitie, "Pixelated detectors and improved efficiency for magnetic imaging in stem differential phase contrast", *Ultramicroscopy*, vol. 165, pp. 42–50, 2016, ISSN: 0304-3991.
- [72] P. Fua, "Model-based optimization: accurate and consistent site modeling", in *18th Congress of International Society for Photogrammetry and Remote Sensing*, 1996.
- [73] K. Thomas, R.-K. Benjamin, P. Fernando, *et al.*, *Jupyter Notebooks-a publishing format for reproducible computational workflows*. 2016, vol. 2016.
- [74] D. N. Johnstone, P. Crout, M. Nord, *et al.*, *Pyxem/pyxem: pyxem 0.12.1*, version v0.12.1, Aug. 2020.

- [75] G. Carlsson, "Topology and data", *Bull. Amer. Math. Soc. (N.S.)*, vol. 46, no. 2, pp. 255–308, 2009.
- [76] G. Adélie and T. Guillaume, "A topological "reading" lesson: classification of mnist using tda", *arXiv*, 2019.
- [77] H. Edelsbrunner and J. Harer, "Persistent homology — a survey".
- [78] A. Madjid, K. Mischaikow, and T. Allen, "Cubical homology and the topological classification of 2d and 3d imagery", vol. 2, Nov. 2001, 173–176 vol.2, ISBN: 0-7803-6725-1.
- [79] L. Kanari, P. Dłotko, and M. S. et al., "A Topological Representation of Branching Neuronal Morphologies", *Neuroinform*, vol. 16, pp. 3–13, 2018.
- [80] R. Vanessa, W. P. John, and A. P. Sheppard, "Theory and algorithms for constructing discrete morse complexes from grayscale digital images", *IEEE Transactions on Pattern Analysis and Machine Intelligence*, vol. 33, no. 8, pp. 1646–1658, 2011.
- [81] D. M. Boyer, S. Mukherjee, and K. Turner, "Persistent homology transform for modeling shapes and surfaces", *Information and Inference: A Journal of the IMA*, vol. 3, pp. 310–344, 2014.
- [82] P. Goodman, "Observation of background contrast in convergent beam patterns.", *Acta Cryst.*, vol. 28, no. 1, pp. 92–93, 1972.
- [83] F. Fujimoto and G. Lehmpfuhl, "Contrast of kossel patterns in electron diffraction", *Zeitschrift für Naturforschung A*, vol. 29, no. 12, 1929–1930b, 1974.
- [84] D. Marie-Christine and A. Didier, "Gold nanoparticles: assembly, supramolecular chemistry, quantum-size-related properties, and applications toward biology, catalysis, and nanotechnology", *Chemical Reviews*, vol. 104, no. 1, pp. 293–346, 2004.
- [85] A. Verma and F. Stellacci, "Effect of surface properties on nanoparticle-cell interactions", *Small.*, vol. 6, no. 1, pp. 12–21, 2010.
- [86] Y. Yi-Cheun, C. Brian, and V. M. Rotello, "Gold nanoparticles: preparation, properties, and applications in bionanotechnology", *Nanoscale*, vol. 4, pp. 1871–1880, 6 2012.
- [87] D. Cressey and E. Callaway, "Cryo-electron microscopy wins chemistry Nobel", *Nature*, vol. 550, no. 167, 2017.
- [88] O. Quy, M. Ting, I. A. Neda, *et al.*, "Cryogenic electron tomography to determine thermodynamic quantities for nanoparticle dispersions", *Mater. Horiz.*, vol. 9, pp. 303–311, 1 2022.
- [89] I. Lazić, M. Wirix, and M. L. L. et al., "Single-particle cryo-EM structures from iDPC-STEM at near-atomic resolution", *Nat Methods*, vol. 19, pp. 1126–1136, 2022.
- [90] B. A. Kopera and M. Retsch, "Computing the 3d radial distribution function from particle positions: an advanced analytic approach", *Analytical chemistry*, vol. 90, pp. 13 909–13 914, 23 2018.

- 
- [91] M. Raissi, P. Perdikaris, and G. E. Karniadakis, “Physics-informed neural networks: A deep learning framework for solving forward and inverse problems involving nonlinear partial differential equations”, *Journal of Computational Physics*, 2019.
  - [92] P. Wang, L. Liu, Y. Liu, C. Theobalt, T. Komura, and W. Wang, *Neus: learning neural implicit surfaces by volume rendering for multi-view reconstruction*, 2023. arXiv: 2106.10689 [cs.CV].





# Curriculum Vitae

## PERSONAL INFORMATION

### Gulnaz Ganeeva

📍 Rue du Simplon 3, Renens 1020, Switzerland

☎ +41 78 802 5400

✉ ganeeva.gul@gmail.com

🌐 [www.linkedin.com/in/gulnaz-g-13842bb4](https://www.linkedin.com/in/gulnaz-g-13842bb4)

Date of birth 30/12/1990

Nationality Russian

## WORK EXPERIENCE

August 2023 – October 2023 **Postdoctoral Researcher**  
Laboratory of Electron Spectrometry and Microscopy (LSME)  
École polytechnique fédérale de Lausanne (EPFL)

June 2018 – July 2023 **Doctoral Assistant**  
Laboratory of Electron Spectrometry and Microscopy (LSME)  
École polytechnique fédérale de Lausanne (EPFL)

July 2016 – May 2018 **Equipment Specialist**  
Pharmaceutical and microbiology equipment sales department  
Kreator Lab, Moscow, Russian Federation

August 2014 – September 2015 **Junior Research Scientist**  
Laboratory of Structural Research  
Institute of Solid State Physics, Russian Academy of Sciences, Chernogolovka

September 2010 – July 2014 **Engineer**  
Laboratory of Structural Research  
Institute of Solid State Physics, Russian Academy of Sciences, Chernogolovka

## EDUCATION

June 2018 – July 2023 **Ph.D. studies in Physics**  
Laboratory of Electron Spectrometry and Microscopy (LSME)  
École Polytechnique Fédérale de Lausanne

- 3D imaging and reconstruction techniques in transmission electron microscopy

September 2009 – July 2014 **Specialist in Physics**  
Lomonosov Moscow State University

- Subject of final qualifying paper: "Structure reconstructions in nano-powders of simple and complex rare-earth oxides: singular cases".

## PERSONAL SKILLS

Languages English (upper-intermediate)  
French (intermediate)  
Russian (native)  
Tatar (native)  
Turkish (intermediate)

## ADDITIONAL INFORMATION

---

### Publications

G. Ganeeva, O. Altingovde, QO. Khac, F. Stellacci, P. Fua, et al., "Automatic 3D Reconstruction by Deep Learning Neural Networks Using Images Acquired via 4D-STEM Stereo Imaging", *Microsc. Microanal.*, 28(S1): 218-20, 2022.

O. Altingovde, A. Mishchuk, G. Ganeeva, E. Oveisi, C. Hebert, P. Fua, "3D Reconstruction of Curvilinear Structures with Stereo Matching Deep Convolutional Neural Networks", *Ultramicroscopy*, Vol. 233, 2022.

I. Shmytko, D. Frolov, A. Aronin, G. Ganeeva, V. Kedrov, "Formation of New Structural States in Compressed BaTiO<sub>3</sub> Nanopowders", *Physics of the Solid State*, Vol. 59, No. 6, pp. 1196-1205, 2017.

I. Shmytko, G. Ganeeva "X-Ray Analysis of the Actual Structure of Yttrium Orthoborate YBO<sub>3</sub>", *Physics of the Solid State*, Vol. 58, No. 12, pp. 2529-2535, 2016.

I. Shmytko, G. Ganeeva, A. Aronin, "Influence of Grain Boundaries on the Formation of New Structural States in Simple Rare-Earth Oxides", *Physics of the Solid State*, Vol. 57, No.1, pp. 136-141, 2015.

### Conferences

IMC20, September 10 – 15, 2023, Busan, South Korea, *Oral presentation*

16MCM, September 4 – 9, 2022, Brno, Czech Republic, *Oral presentation*

M&M2022, July 31 – August 4, 2022, Portland, Oregon, USA, *Poster presentation*

PICO2022, May 8 – 12, 2022, Kasteel Vaalsbroek, Netherlands, *Poster presentation*

PICO2021, virtual conference, May 2 - 6, 2021, *Poster presentation*

MC2021, virtual conference, August 22 - 26, 2021, *Poster presentation*

"Interdisciplinary Symposium on 3D Microscopy", October 1 - 4, 2019, Engelberg, Switzerland, *Oral presentation*

### Awards

EPFL-CIME Image Contest. *Winner of September/October 2021 contest period*

### Certificates

Business Concept Training (Innosuisse, Switzerland). *Winner of one year at La Forge accelerator*